Experimental equilibrium structures of solids and gases

Anthony M. Reilly

Doctor of Philosophy
University of Edinburgh
2009

Declaration

This thesis has not been previously submitted, in whole or in part, for any degree at this or any other university. The work is original and my own, carried out under the supervision of Prof. David W. H. Rankin; where this is not so, credit has been duly given.

(*Anthony M. Reilly*)

Acknowledgements

I would like to thank my supervisors, David Rankin and Carole Morrison, for giving me the opportunity to work with them and for all the guidance and support they have provided over my three enjoyable years in Edinburgh. My thanks also to the everyone who has graced the Rankin, Morrison and Masters research groups during that time, for their help, support and cake! I especially thank Derek Wann for proof-reading many split-infinitive laden documents and answering many silly questions.

Much of the work presented in this thesis could not have been performed without the help of collaborators and colleagues in Edinburgh and elsewhere. In particular, the PIMD simulations of ammonia and nitromethane would not have been possible without the generous help of Scott Habershon and David Manolopoulos, both of the University of Oxford.

Thanks also to everyone else from the School of Chemistry (especially those who I have managed to beat at pool), the orienteering club and elsewhere who have made my time in Edinburgh so productive and such good fun. Ruchika, Andrew and others from back home have always been a good source of advice and a laugh. The lovely Kirsten has made the last year particularly enjoyable.

Finally, I would like to thank my parents and the rest of my family. They have always been very supportive of my studies, home and abroad, for which I am very grateful.

Abstract

In the past sixty years, X-ray, neutron and electron diffraction have emerged as the structural techniques of choice in the solid state. However, despite many advances in theory and instrumentation, these diffraction methods are still reliant on a number of assumptions. Chief amongst these is that the atoms in the crystal vibrate in a harmonic fashion.

This thesis is concerned with understanding the effects of anharmonic motion on crystal structure determination and developing new ways of moving beyond the harmonic approximation used in crystallography.

A method has been developed, using molecular dynamics simulations, to correct experimental structures to equilibrium structures. This has been applied to the crystal structures of phase-I deutero-ammonia, deutero-nitromethane and benzophenone. Path-integral molecular dynamics simulations have been used to obtain meaningful comparison with experimental data collected at low temperatures. The simulations also offer information on the probability density functions that describe thermal motion in solids. Using data from simulations of nitromethane and other compounds it has been demonstrated that the molecular dynamics-derived data can be used to assess and develop new functions for modelling thermal motion in crystal structure refinements.

Finally, similar molecular dynamics techniques have been applied to determine the equilibrium structures of some polyhedral oligomeric silsesquioxanes in the gas phase. Some members of this class of compounds feature such strong anharmonic motion that refinement of the structures using gas electron diffraction is impossible without taking into account the effects of the anharmonicity.

Abbreviations and acronyms

ADP	anisotropic displacement parameter
BOMD	Born-Oppenheimer molecular dynamics
CI	configuration interaction
CNDO	complete neglect of differential overlap
CPMD	Car-Parrinello molecular dynamics
DFT	density functional theory
DMUOX	2:1 adduct of dimethyl-urea and oxalic acid
EHT	extended-Hückel theory
EP	empirical potential
EPSRC	engineering and physical sciences research council
Expt.	experimental
FF	force field
GC	Gram-Charlier
GGA	generalised-gradient approximation
GPW	Gaussian plane-wave
GTO	Gaussian-type orbital
HF	Hartree-Fock
HMT	hexamethylenetetramine
INDO	intermediate neglect of differential overlap
LD	lattice dynamics
LDA	local-density approximation
MD	molecular dynamics
Me	methyl
MNDO	modified neglect of diatomic overlap

MP	Monkhorst-Pack
NH	Nosé-Hoover
OPP	one-particle potential
PCA	principal component analysis
PDF	probability density function
PI(MD)	path-integral (molecular dynamics)
PP	pseudopotential
PW	plane wave
QM	quantum mechanical
RDC	radial distribution curve
r	interatomic distance
r_a	average interatomic distance (definition depends on method)
r_e	equilibrium distance
r_p	most probable distance
SCF	self-consistent field
SE	semi-empirical
SN	skew-normal
STO	Slater-type orbital
TLS	translation, libration and screw tensors
UPA	1:1 adduct of urea and phosphoric acid
vdW	van der Waals
ZPE	zero-point energy

Contents

Chapter 1

Thermal motion in crystalline solids

1.1 Diffraction Methods

The fundamental goal of chemistry is to understand and manipulate chemical systems. Its scope is therefore very broad, encompassing many different areas and topics, from the behaviour of materials to the targeting of active sites in proteins. Structural chemistry is a field of study which transcends all of the applications of chemistry. Techniques such as spectroscopy, elemental analysis, diffraction and computer simulation yield the critical information that allows us to understand chemical systems, spurring us on to manipulate them in ever more innovative and useful ways. Application of chemical knowledge is naturally the primary focus of chemical research but it will always be important to ensure that the methods that yield such knowledge are developed, tested and validated regularly.

The main focus of this thesis is the field of diffraction, in particular, solid-state diffraction. Diffraction methods can probe matter in the solid, liquid and gaseous phases to reveal raw structural parameters such as bond lengths, angles and atomic positions. Depending on the type of diffraction used, information on bonding, vibrations, phase transitions and even reactions can also be obtained. Solid-state diffraction, especially using X-rays, is one of the most widely used structural techniques with currently over 450,000 organic or metallo-organic structures in the Cambridge structural database (CSD). That the CSD reference paper by Allen,[1] dating from only seven years ago (2002), is entitled "The Cambridge Structural Database: a quarter of a million crystal structures and rising" illustrates the phenomenal growth in the application of this versatile characterisation technique.

The phenomenon of diffraction has a long and venerable history dating back to Young,[2] whose double-slit experiment demonstrated that light can be diffracted and therefore had wave-like properties. Diffraction of X-rays by a crystal was first shown by von Laue in 1913,[3] while diffraction by a gas (with X-rays) was first performed by Debye in 1929.[4] From then on there have been many developments of diffraction techniques and theory, extending diffraction to electrons and neutrons and studying ever more complex systems.

Structural chemists do not consider individual systems in isolation. Some of the most important insights are to be found in comparing different materials, polymorphs, and even the same molecule at two different temperatures or pressures. Doing this requires comparing structural information but quantitative comparison can be hindered by a number of things. Chief amongst these is the fact that most structural observations are averaged over the thermal motion that occurs in the system of interest. This is a result of the short time-scale of vibrations and motions compared to the time an experiment takes. The nature of thermal motion will, naturally, be different from system to system, preventing direct comparison. To overcome this problem it is preferable to correct structural parameters to values that represent the system at rest with no thermal motion. These *equilibrium* values can then be directly compared. Equilibrium values are routinely obtained by computer simulations of chemical systems. Comparison of computational results with experimental ones is desirable not just to confirm an experimental result or augment it in some way but also to validate the computational theory for use in systems on length and time scales were experimentation is not feasible.

Thermal motion has been a consideration in solid-state diffraction from practically the beginning.[5] The majority of diffraction experiments model thermal motion in a harmonic fashion (as outlined in Section 1.3.1). Despite the work of Cruickshank[6] and many others in highlighting the deficiencies of this model and proposing more sophisticated methods of dealing with it, it is still rare to see structural analysis performed using anything other than a harmonic treatment. The two main reasons for this were the lack of data of sufficient quality for an anharmonic model of thermal motion and also a lack of information about the true nature of the problem specifically because models of anharmonicity involve so many extra parameters. Technical developments mean that the former is no longer a serious issue, while addressing (or at least starting to address) the latter is the focus of the work presented in this thesis. Theoretical simulations of thermal motion, using the molecular dynamics (MD) technique, will be used to bridge the gap between time-averaged and equilibrium crystal structures. The information obtained using the MD simulations will be used to understand and hopefully improve the process of modelling anharmonic thermal motion.

The remainder of this chapter outlines the basic equations and mathematics of crystallography, showing why thermal motion is important. The various approaches for modelling anharmonic thermal motion that have been developed already will also be discussed.

1.2 Diffraction by a lattice

The majority of diffraction experiments in the solid state are carried out on perfect or near-perfect crystalline solids. In such a solid the atoms are packed and positioned in a regular order that repeats in all space upon a lattice. The smallest repeating unit is the unit cell of the crystal, which can be mathematically represented using three basis vectors, $\mathbf{a}_1$, $\mathbf{a}_2$ and $\mathbf{a}_3$. Positions in the unit cell may be referenced using these vectors and fractional coordinates, (x, y, z):

$$\mathbf{r} = (x\mathbf{a}_1 + y\mathbf{a}_2 + z\mathbf{a}_3). \tag{1.1}$$

In total there are fourteen unique types of lattices, which are referred to as Bravias lattices.[7] The regular positioning of atoms in the lattices results in numerous planes of atoms being formed. Each plane can be labelled with a Miller Index, $\mathbf{H} = (h,k,l)$, which is the inverse of the fractional coordinate at which the plane intersects the crystallographic axes. The long-range order that results from these planes may be succinctly represented using the reciprocal lattice of the Bravias lattice. This lattice is comprised of all of the wave-vectors that represent the planes of the Bravais lattice, where each plane can be represented as a plane-wave. The reciprocal lattice basis vectors can be obtained from the real space ones:

$$\mathbf{b}_1 = \frac{\mathbf{a}_2 \times \mathbf{a}_3}{\mathbf{a}_1 \cdot (\mathbf{a}_2 \times \mathbf{a}_3)}; \mathbf{b}_2 = \frac{\mathbf{a}_3 \times \mathbf{a}_1}{\mathbf{a}_2 \cdot (\mathbf{a}_3 \times \mathbf{a}_1)}; \mathbf{b}_3 = \frac{\mathbf{a}_1 \times \mathbf{a}_2}{\mathbf{a}_3 \cdot (\mathbf{a}_1 \times \mathbf{a}_2)}. \tag{1.2}$$

A position, $\mathbf{r}^*$, in the reciprocal lattice can be represented in a similar fashion to that in the real lattice. In particular,

$$\mathbf{r}^*_{\mathbf{H}} = h\mathbf{b}_1 + k\mathbf{b}_2 + l\mathbf{b}_3 = \mathbf{H}\ \mathbf{b}^T. \tag{1.3}$$

where $\mathbf{b}^T$ is the transpose of $\mathbf{b}$.

It is the planes of atoms in the crystal that diffract the incident beam of light or wave-particles. The necessary condition for constructive interference of the diffracted beam is given by Bragg's law,[7]

$$n\lambda = 2d_{hkl}\sin\theta, \tag{1.4}$$

where d_{hkl} is the spacing between two hkl planes and θ is the scattering angle. Bragg's law leads to the relationship between scattering angle and distance in reciprocal space:

$$2\sin\theta/\lambda = \frac{1}{d_{hkl}}, \tag{1.5}$$

$$2\sin\theta/\lambda = |\mathbf{r}^*_{\mathbf{H}}|. \tag{1.6}$$

For diffraction from a single crystal the result is a pattern of diffraction spots. If a powder sample is used then the random orientation of the microcrystals leads to a diffraction pattern comprised of concentric rings. As each spot gives us information on a plane in the lattice the diffraction pattern is directly related to the reciprocal lattice of the crystals. The intensity of a given hkl diffraction spot can be determined from the structure factor, $F(hkl)$ which is the Fourier transform of the real-space scattering density of the N atoms in the unit cell to reciprocal space:

$$F(\mathbf{H}) = \sum_{n=1}^{N} f(\mathbf{H})\exp(i2\pi\mathbf{H}\cdot\mathbf{x}_n), \tag{1.7}$$

where $\mathbf{x}$ is the fractional position of an atom in the unit cell and $f(\mathbf{H})$ is the form factor or scattering density for the n^{th} atom. Equation 1.7 is given in terms of the dimensionless vector $\mathbf{H}$. Alternatively, the substitution $\mathbf{Q} = 2\pi\mathbf{H}\mathbf{b}^T$ is made to give:

$$F(\mathbf{Q}) = \sum_{n=1}^{N} f(\mathbf{Q}) \exp(i\mathbf{Q} \cdot \mathbf{r}_n), \tag{1.8}$$

where the use of $\mathbf{Q}$ means that $\mathbf{x}_n$ is replaced by the Cartesian position of the atom, $\mathbf{r}_n$. The diffraction experiment determines the intensity of scattering in reciprocal space, which is the square modulus of the structure factor:

$$I^{obs}(\mathbf{Q}) = |F(\mathbf{Q})|^2. \tag{1.9}$$

Each value of F has a phase associated with it that relates the positions of the atoms to each other. This information is lost in the diffraction experiment as the intensity determines only the square of the amplitude, $|F(\mathbf{H})|$. This *phase problem* has been a major consideration of crystallography for many years,[8] and as a result a number of different methods have been developed to “solve” crystals structures and determine suitable initial guesses for the phases for use in refinement.

1.2.1 Form factors

The interaction of the crystal with the diffraction beam is determined by the type of particles incident on the sample. This is incorporated into Equation 1.7 by the form factor, $f(\mathbf{H})$. X-rays interact with the electron density surrounding an atom and it can be shown that the X-ray form factor is the Fourier transform of the electron density to reciprocal space. As a first approximation this may be assumed to be spherically symmetric and many structure refinements use scattering factors of this type. As the electron density of the atom is of the order of the wavelengths used in diffraction experiments, the scattering factors vary with the angle of the incident X-ray beam. A nine parameter analytical expression was developed by Cromer and Mann[9] to represent the scattering factor as a function of $\sin\theta/\lambda$, which is equivalent to $|\mathbf{Hb}|/2$:

$$f_{\text{x-ray}}(\sin\theta/\lambda) = \sum_{i=1}^{4} a_i \exp(-b_i \sin\theta/\lambda) + c, \tag{1.10}$$

with the value of $f(0)$ equal to the number of electrons for that atom. The exponential form means that this function tails off at higher values of $\sin\theta/\lambda$. In a molecule the valence electron density will be significantly deformed from that of an isolated atom and may no longer be centred on the position of the nucleus. Correctly modelling the density requires specific fitting for each system of interest and is not routinely performed due to the large number of parameters required. As a result the majority of X-ray diffraction structures determine the centre of the electron density and not the true atomic position.

In neutron diffraction scattering occurs directly from the nucleus. As the nucleus is much smaller than the wavelength of the neutrons the scattering is effectively from a single point and displays no angular dependence. Thus $f(\mathbf{H})$ in Equation 1.7 is a constant for a given atom and is usually referred to as the coherent scattering length, b, which is measured in fm (10^{-15} m). The total scattering in neutron diffraction is typically much smaller than from X-ray diffraction, due to the small size of the nucleus, but the scattering lengths are not directly proportional to atomic number as $f(0)$ is in X-ray diffraction.[10] The result is that lighter atoms can be much easier to distinguish in neutron diffraction. In particular, deuterium is used often in neutron diffraction as its scattering length is very similar to that of the carbon atom (approximately 6.6 fm). Some nuclei, including H with $b_{\mathrm{H}} = -3.7$ fm, have a negative scattering length, indicating that neutrons scattered by these nuclei have a phase of 180° relative to neutrons scattered by other nuclei.

The form factor for electrons is dependent both on the nuclear charge, Z, and the electron density and thus is dependent on the X-ray form factor:[8,11]

$$f_{\text{elec}}(\sin\theta/\lambda) = \frac{Z - f_{\text{x-ray}}(\sin\theta/\lambda)}{2\pi\sin^2\theta/\lambda^2}. \tag{1.11}$$

Typically electron diffraction intensities are higher than those for X-ray or neutron diffraction. As a result electron diffraction may be performed for very small sample sizes, making it a very useful characterisation technique in the solid state. Electrons are also used for diffraction in the gas phase.

1.3 Thermal motion in the solid state

The crystal described by Equation 1.7 is at rest, with no movement of the atoms. In a real system there will be a significant amount of thermal motion. In molecular crystals this motion may range from intramolecular vibrations (bond stretches, angle bends *etc.*) to intermolecular lattice vibrations. Some of these intermolecular vibrations may involve translational motion, where atoms move along straight lines, or librational motion along curved trajectories.

This thermal motion can be incorporated into the structure factor by considering the structure factor of a system where the n^{th} atom has a Cartesian displacement, $\mathbf{u}_n$, from its mean position, $\mathbf{x}_{n0}$:[12]

$$F(\mathbf{H}) = \sum_{n=1}^{N} f(\mathbf{H}) \exp(i2\pi\mathbf{H} \cdot (\mathbf{x}_{n0} + \mathbf{r}^*_{\mathbf{H}} \cdot \mathbf{u}_n)) \tag{1.12}$$

$$F(\mathbf{Q}) = \sum_{n=1}^{N} f(\mathbf{Q}) \exp(i\mathbf{Q} \cdot \mathbf{r}_{n0}) \times \exp(i\mathbf{Q} \cdot \mathbf{u}_n). \tag{1.13}$$

The experimentally measured intensity is the square modulus of the time and space average over all of the possible displacements of the atoms:

$$I^{obs}(\mathbf{Q}) = |\langle F(\mathbf{Q}) \rangle|^2$$

$$\langle F(\mathbf{Q}) \rangle = \sum_{n=1}^{N} f(\mathbf{Q}) \exp(i\mathbf{Q} \cdot \mathbf{r}_{n0}) \times \langle \exp(i\mathbf{Q} \cdot \mathbf{u}_n) \rangle. \tag{1.14}$$

The mean or average value of a function, $f(x)$, is given by

$$\langle f(x) \rangle = \int_{-\infty}^{\infty} f(x) P(x) \, \mathrm{d}x, \tag{1.15}$$

where $P(x)$ is the probability density function (PDF) for the variable x. Combining Equation 1.15 with the term in angle brackets from Equation 1.14 yields:

$$\langle \exp(i\mathbf{Q} \cdot \mathbf{u}_n) \rangle = \int_{-\infty}^{\infty} \exp(i\mathbf{Q} \cdot \mathbf{u}_n) P(\mathbf{u}) \, \mathrm{d}\mathbf{u}. \tag{1.16}$$

This equation represents the characteristic function of the probability distribution. The characteristic function, $\hat{P}(\mathbf{Q})$, is closely related to the Fourier transform of $P(\mathbf{u})$ and the two terms are often used interchangeably in crystallographic literature. The structure factor then takes the form

$$\langle F(\mathbf{Q})\rangle = \sum_{n=1}^{N} f(\mathbf{Q})\hat{P}(\mathbf{Q})\exp(i\mathbf{Q}\cdot\mathbf{r}_{n0}). \tag{1.17}$$

$\hat{P}(\mathbf{Q})$ is known as the Debye-Waller factor after Debye and Waller, who first identified its role in the structure factor.[5] It is also known as the atomic temperature factor or the atomic displacement factor.[13] $\hat{P}(\mathbf{Q})$ reduces the scattering intensity, accounting for the fact that the atom will not spend all of its time on the lattice site that fulfils the condition for Bragg scattering. At large values of $\mathbf{Q}$ the scattering should be completely damped out. In the classical limit of Boltzmann statistics the PDF can be related to the underlying effective free-energy surface, $V_{\text{eff}}(\mathbf{u})$, by the Boltzmann equation:[12,14]

$$P(\mathbf{u}) \propto \exp(-V_{\text{eff}}(\mathbf{u})/k_{\text{b}}T). \tag{1.18}$$

$V_{\text{eff}}(\mathbf{u})$ represents the motion of an atom in the mean field of the other atoms present in the system.

The functional form of $P(\mathbf{u})$ can have a significant effect on the structure parameters that crystallography determines and a number of different types of PDF have been used previously to approximate the true probability function. There is generally a trade off between the sophistication of the model and the number of parameters that are required to fit it.

1.3.1 Gaussian approximation

A useful starting approximation for thermal motion is to assume that the atoms behave like harmonic oscillators. If the atoms move independently of each other then the oscillations will be identical in all directions and we may consider them as one-dimensional oscillators. The potential energy, $V(u)$, for a harmonic oscillator is given by ku^2 and it can be shown using Equation 1.18 that this leads to a Gaussian distribution in u:[12]

$$P(u) = \frac{1}{2\pi\sqrt{U_{\mathrm{eq}}}} \exp\left(-\frac{u^2}{2U_{\mathrm{eq}}}\right), \tag{1.19}$$

where U_{eq} is the variance, $\langle u^2 \rangle$, of the distribution. The Fourier transform of this is given by:

$$\hat{P}(|\mathbf{r}^*_{\mathbf{H}}|) = \exp(-2\pi^2 U_{\mathrm{eq}} |\mathbf{r}^*_{\mathbf{H}}|^2) = \exp(-8\pi^2 U_{\mathrm{eq}} \sin^2\theta/\lambda^2). \tag{1.20}$$

The isotropic model is very useful for systems with poor or incomplete data as it only requires a single parameter per atom and is often used in powder diffraction studies and protein crystallography. The effect of isotropic motion on a neutron scattering length is shown in Figure 1.1.

Figure 1.1: Neutron scattering factor with a isotropic Debye-Waller factor (dashed line) and without (solid line).

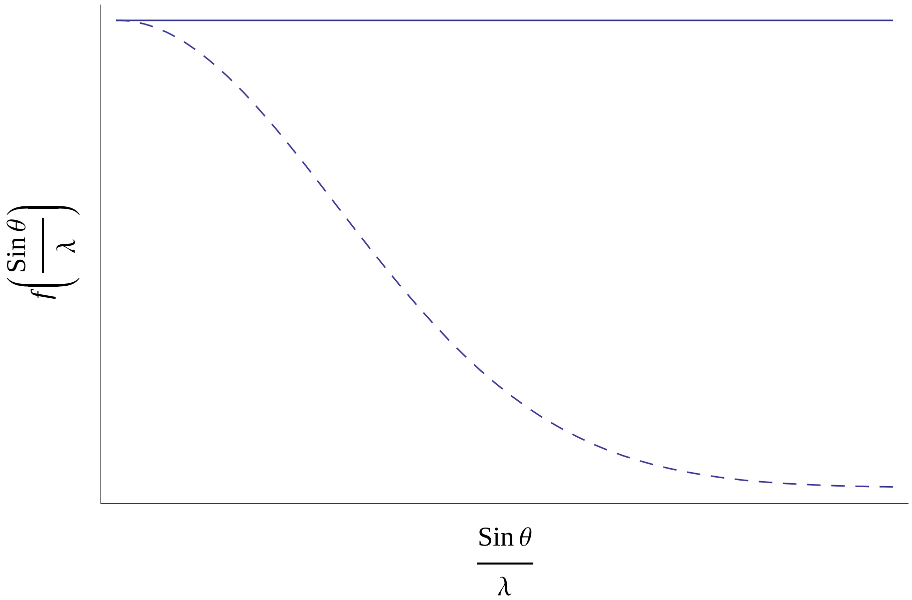

Another common approximation is to take $P(\mathbf{u})$ as being a trivariate Gaussian PDF. This allows for harmonic motion along three separate axes. A trivariate Guassian PDF is given by:[15,16]

$$P(\mathbf{u}) = \frac{det(\mathbf{U}^{-1/2})}{8\pi^3} \exp(-\frac{1}{2}\mathbf{u}^T\mathbf{U}^{-1}\mathbf{u}), \tag{1.21}$$

where $\mathbf{U}$ is the symmetric, 3×3 variance-covariance matrix of the distribution, whose elements U_{ij} equal $\langle u_i u_j \rangle$. Taking the Fourier transform leads to

$$\hat{P}(\mathbf{Q}) = \exp(-\frac{1}{2}\mathbf{Q}^T\mathbf{U}\mathbf{Q}). \tag{1.22}$$

The six unique elements of $\mathbf{U}$ usually have units of Å^2 and are referred to as the anisotropic displacement parameters[13](ADPs), although other names and forms for them are given in some older papers. The trivariate or anisotropic approximation can lead to significantly better R factors and is widely used in small-molecule X-ray and neutron diffraction.

The Gaussian probability distributions are easily visualised using surfaces of constant probability. The size of the surface is scaled so that the atoms have a certain percentage chance of being within them. For a monovariate Gaussian the probability surface is spherical in shape, while in the trivariate case probability ellipsoids are depicted.[17] Figure 1.2 shows a typical probability ellipsoid plot for nitromethane.

Figure 1.2: Theoretical thermal ellipsoids of deuterated nitromethane at 228 K, plotted at the 50% probability level. See Chapter 4 for more information.

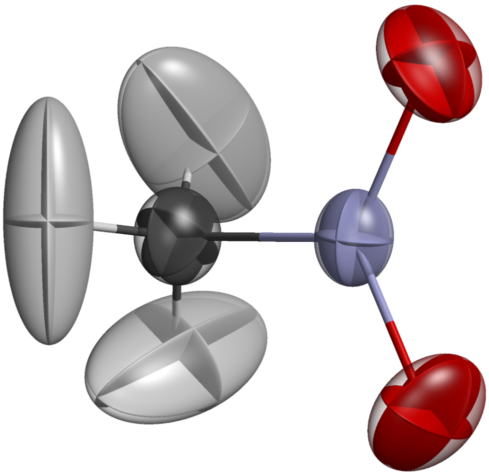

1.3.2 Equilibrium and time-averaged positions

Central to structural studies of crystals is the determination of the atomic positions in the lattice. It is important to note though that a number of different types of position may be defined and determined. The formulation of the structure factor leads to a 3-dimensional (3-D) PDF being determined for each atom. The 3-D PDF represents the motions of the atom in the mean field of all of the other atoms in the system. It is the full $(3N-3)$-dimensional crystallographic PDF integrated over the other atoms in the unit cell. By definition the position, $\mathbf{r}_{n0}$ or $\mathbf{x}_{n0}$, appearing in the structure factor (Equation 1.17) is the mean or time-averaged atomic position given by the 3-D PDF, which will be denoted $\mathbf{r}_{\mathrm{a}}$. For a 1-dimensional (1-D) object the mean is the position about which the object would balance. From the Boltzmann relationship (Equation 1.18) the atomic PDF corresponds to an effective free-energy surface. The minimum of this surface corresponds to the maximum or mode of the PDF. This position is referred to as the mode position by Johnson.[16] To avoid confusion with a mean position, in this work it will be referred to as the probable position, $\mathbf{r}_{\mathrm{p}}$.

In a harmonic system the probable and time-average positions will coincide as the distribution is symmetric about the mean/probable position. If the free-energy surface is anharmonic then they will differ. In integrating the full 3-D PDF we lose information about the correlated motions of atoms. As such the geometry obtained from the combination of probable positions may not coincide with the minimum of the $(3N-3)$-D potential-energy surface the equilibrium position, $\mathbf{r}_{\mathrm{e}}$. Only in the harmonic case will all three positions be guaranteed to be the same. For an anharmonic system the equilibrium position can only be obtained from experiment with an assumption on the relationship between the full $(3N-3)$-D potential-energy surface and the 3-D effective free-energy surface.

The equilibrium and time-averaged geometries can differ significantly and determining the time-average geometry can result in physically meaningless structural parameters. The problem was highlighted by Cruickshank,[6] who considered the librational motion of an atom relative to another where the time

-averaged position differed substantially from the equilibrium or most probable position. As Figure 1.3 illustrates the harmonic ellipsoid is placed at the time-averaged position leading to poor agreement with the anharmonic PDF and thus a poor agreement factor. In general librational motion between atoms leads to shortening of bonded distances. Asymmetric free-energy surfaces will also lead to apparent lengthening or shortening of bonds. Comparison of bond lengths and other parameters from different structures is fraught with difficulties unless the effects of thermal motion are taken into account.

Figure 1.3: Representation of the curved PDF of an atom (grey) showing the equilibrium position and the averaged position (with the corresponding harmonic ellipsoid).

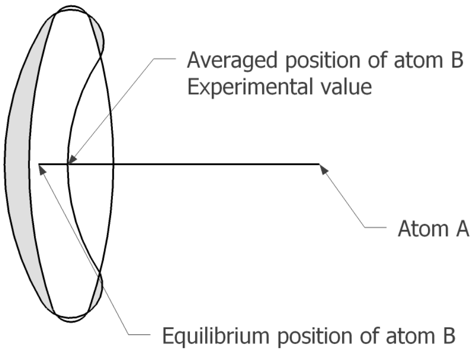

1.3.3 Beyond the Gaussian Approximation

A considerable amount of research has been performed with the aim of improving the description of thermal motion in crystallography. Some of these methods aim to analyse the harmonic model and correct for librational motion, while other utilise more complex expressions for the PDF. In general these approaches are based on physical, statistical or kinematic interpretations of the anharmonicity. The full mathematical treatment of these methods is detailed and only a brief overview is provided here. A more comprehensive overview is available within the International Tables for Crystallography.[15] Expressions using tensors are shortened using Einstein sum notation (where all indices repeated twice are implicitly summed over) with the indices running from 1 to 3 unless otherwise stated.[18]

Kinematic models

The kinematic methods model the thermal motion as having a specific physical form. The curvilinear or librational motion of Figure 1.3 has been of considerable interest to many authors. If the motion of the atoms in a molecule are correlated, *i.e.* the molecule behaves as a rigid body, then differences between the ADPs of atoms in different parts of the molecule can be interpreted as being the result of the librational motion of the molecule. The **TLS** method refines 20 parameters that describe the librational (**L**), translational (**T**) and screw (**S**) motions of the molecule from the ADPs.[19] Screw motions are a correlation of translational and librational motion. Only the librational motion leads to thermal shortening effects (in the "harmonic" limit) and the **L** tensor can be used to correct the interatomic distances. In systems that deviate from the rigid-body approximation such models can lead to spurious results. A similar method, **TLX**, was developed by Cruickshank and Pawley.[20] These *a posteriori* methods provide only intramolecular distance corrections. Corrections for intermolecular distances cannot be obtained from a single-temperature measurement as the correlations between the motions of different molecules are unknown. Some of this information can be recovered using multi-temperature datasets.[21] A stand-alone program THMA[22] is available for performing **TLS** analysis and it is also incorporated in the CRYSTALS program.[23]

An alternative to *a posteriori* corrections is to include the librational effects in the structure-factor equation. Willis and Pawley developed such an approach by modelling the librational motion as occurring around a fixed axis of libration with structure factors expressed for isotropic[24] and anisotropic[25] motion of rigid bodies. Incorporating the curvilinear motion into the structure factor has the advantage of leading to better agreement factors, the R factor, weighted R factor *etc.*

Physical models

The physical models aim to fit the potential, $V(\mathbf{u})$, that describes the thermal motion of the atom as given in Equation 1.18. The true form of the potential should reflect the correlation between atomic motions. However, most formulations treat the potential as being for a single particle and so these methods are often referred to as the one-particle potential (OPP) or isolated-atom potential (IAP) approach. The original formalisation for the OPP method was given by Willis[26] for cubic space groups and extended to generic symmetry by Tanaka and Marumo.[27] Combining Equation 1.18 with Equations 1.14 and 1.15 in an orthogonal coordinate system leads to the OPP expression for $\hat{P}(\mathbf{Q})$:

$$\hat{P}(\mathbf{Q}) = \left[\int_{-\infty}^{\infty} \exp(i\mathbf{Q}\mathbf{u}) \exp(-V_{\text{eff}}(\mathbf{u})/k_{\text{b}}T)\,\mathrm{d}\mathbf{u}\right] / Z_{\text{OPP}}, \tag{1.23}$$

where Z_{OPP} is the partition function

$$Z_{\text{OPP}} = \int_{-\infty}^{\infty} \exp(-V_{\text{eff}}(\mathbf{u})/k_{\text{b}}T)\,\mathrm{d}\mathbf{u}. \tag{1.24}$$

The anharmonic effects are incorporated using a power series expansion about the harmonic potential with higher order force constants, γ and δ:

$$\begin{aligned} V_{\text{OPP}}(\mathbf{u}) &= V_{\text{harm}}(\mathbf{u}) + \gamma_{ijk}u^i u^j u^k + \delta_{ijkl}u^i u^j u^k u^l \\ &= V_{\text{harm}}(\mathbf{u}) + \Delta V. \end{aligned} \tag{1.25}$$

Equation 1.23 cannot be analytically determined with the anharmonic potential given by Equation 1.25, so an approximation is required for practical use of the OPP method:

$$\exp\left(-\Delta V(\mathbf{u})/k_{\text{b}}T\right) \simeq 1 - \Delta V(\mathbf{u})/k_{\text{b}}T. \tag{1.26}$$

This approximation holds only while the anharmonic contribution is small, limiting the application of the OPP method.[14] The resulting anharmonic structure factor is a power series expansion of the harmonic part.[27] In addition, while the fitted potential may reflect the experimental behaviour, the force constants may not have any real physical significance. The effective potential can also be obtained using other methods using Equation 1.18 and numerical evaluation if required. Fourier-invariant expressions for the OPP method are also available[15] but direct, analytical refinement of the potential will always be hindered by the approximation of Equation 1.26.

Statistical models

The final group of methods focus on improving the functional form of $P(\mathbf{u})$. Some of these methods parametrise the probability density function for motion on the surface of sphere or circle and expanding $P(\mathbf{u})$ in terms of spherical harmonics has also been used.[15] The most widely used statistical methods are the Gram-Charlier (GC) and Edgeworth series.[14,16] Both of these methods expand the anharmonic PDF in terms of the harmonic one multiplied by various different orders of Hermite polynomials. For crystallographic use these are defined as:[15,28]

$$H(\mathbf{u})_{\alpha\beta\gamma\ldots} = (-1)^p \exp\left(\frac{1}{2}U^{-1}_{jk}u^j u^k\right)\left[\frac{\partial^p}{\partial u_\alpha \partial u_\beta \partial u_\gamma \ldots}\exp\left(-\frac{1}{2}U^{-1}_{jk}u^j u^k\right)\right]. \tag{1.27}$$

The super- and subscript indexes refer to the contra and co-variance of the polynomials and coefficients.[8,14] For the one-dimensional standardised normal distribution the first five Hermite polynomials are:

$$\begin{aligned} H_0(x) &= 1 \\ H_1(x) &= x \\ H_2(x) &= x^2 - 1 \\ H_3(x) &= x^3 - 3x \\ H_4(x) &= x^4 - 6x^2 + 3, \end{aligned}$$

which are plotted in Figure 1.4. The odd polynomials are odd functions and will skew the anharmonic distribution while even order terms will change its “peakedness”. In 2 dimensions the odd-order functions can bend the probability

Figure 1.4: The first five 1-dimensional Hermite polynomials of the standardised normal distribution. ($H_0(x)$ is along the x-axis.)

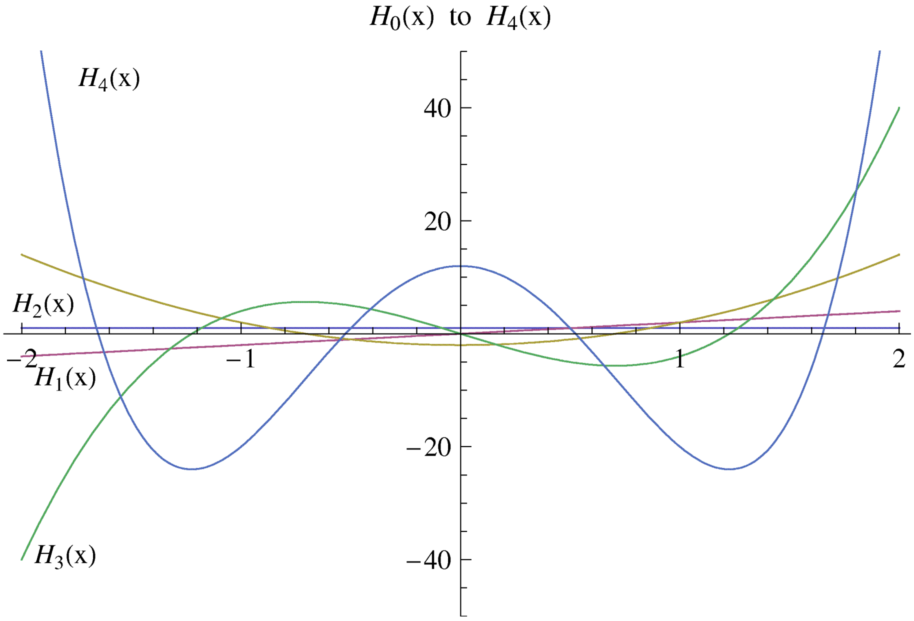

distribution to give an approximation of curvilinear motion. The Gram-Charlier series PDF is given by:[15,29]

$$P_{\mathrm{GC}}(\mathbf{u}) = P(\mathbf{u})_{\mathrm{harm}} \left[1 + \frac{1}{3!} c^{jkl} H_{jkl}(\mathbf{u}) + \frac{1}{4!} c^{jklm} H_{jklm}(\mathbf{u}) + ...\right]. \tag{1.28}$$

where $P(\mathbf{u})_{\mathrm{harm}}$ is the normal trivariate Gaussian distribution and the expansion coefficients, $c^{jk\cdots}$, are the quasi moments of the PDF given by the appropriate generating function:[30]

$$M(\mathbf{Q}) = \exp\left(\frac{1}{2}\langle(\mathbf{Q}\cdot\mathbf{u})^2\rangle\right)\left[\sum_{N=0}^{\infty} c_{jkl...}\frac{i^N}{N!} Q_j Q_k Q_l ...\right]; \tag{1.29}$$

$$c_{jkl...} = \frac{d^N M(\mathbf{0})}{d\mathbf{Q}}. \tag{1.30}$$

The Fourier transform of Equation 1.28 is the quantity directly determined by the refinement:

$$\hat{P}_{\mathrm{GC}}(\mathbf{Q}) = \hat{P}_{\mathrm{harm}}(\mathbf{Q}) \left[1 - i c^{jkl} Q_j Q_k Q_l + c^{jklm} Q_j Q_k Q_l Q_m + ...\right]. \tag{1.31}$$

The first- and second-order Hermite polynomials are not included in Equation 1.28 as the first- and second-order quasi-moments can become correlated with the harmonic mean and variances.[14,16,31] The method has been used a number of times and is incorporated in the PROMETHEUS refinement program[32] and the more recent XD2006 code.[33] The functional form of the GC series is very flexible but at a cost of a substantial number of parameters, with up 60 parameters required per atom to perform a sixth-order refinement. The flexibility of the GC series has seen it used to model disorder and split-atom systems.[34]

In the Edgeworth series, different expansion coefficients are used. Instead of quasi-moments the cumulants, κ, of the PDF are used:

$$K(\mathbf{Q}) = \exp\left(\sum_{N=0}^{\infty} \kappa_{jkl...} \frac{i^N}{N!} Q_j Q_k Q_l ...\right). \tag{1.32}$$

A given order cumulant is determined by lower order cumulants and moments and *vice versa*. As a result truncation of the Edgeworth series to a given order leaves the highest order cumulants poorly defined. The Fourier transform of $P(\mathbf{u})$ between real and reciprocal space is not analytically possible. For crystallographic use, the Edgeworth series is defined in reciprocal space:

$$\hat{P}_{\mathrm{EW}}(\mathbf{Q}) = \hat{P}_{\mathrm{harm}}(\mathbf{Q}) \exp\left(-i\kappa^{jkl} Q_j Q_k Q_l + \kappa^{jklm} Q_j Q_k Q_l Q_m\right). \tag{1.33}$$

The suggested form for the real space PDF is given by:[14,16,35]

$$P_{\mathrm{EW}}(\mathbf{u}) = P(\mathbf{u})_{\mathrm{harm}} \left[1 + \frac{1}{3!}\kappa^{jkl} H_{jkl}(\mathbf{u}) + \frac{1}{4!}\kappa^{jklm} H_{jklm}(\mathbf{u}) + \kappa^{jkl}\kappa^{mno} H_{jklmno}(\mathbf{u})\right]. \tag{1.34}$$

The exponential form of $\hat{P}_{\mathrm{EW}}(\mathbf{Q})$ in Equation 1.33 makes it possible for the Edgeworth series to diverge, as in the case of the OPP method. The Gram-Charlier and Edgeworth expansions are identical in the limit of an infinite expansion.

1.3.4 Modern usage of anharmonic Debye-Waller factors

The use of anharmonic refinements has been restricted. In the 1970's and 80's a number of groups and researchers both developed and applied the methodologies outlined in the preceding section. However, application of the method has been held back for a number of reasons. First, many of the methods can require a large number of extra parameters and thus a substantial number of reflections, as a 10:1 reflection to parameter ratio is preferred in crystallographic studies.[36] While sufficient quality data can be collected with X-rays, refinement of the aspherical form factors is necessary to model thermal motion correctly. This introduces yet more parameters and there is potential for correlation of the results. This will still yield the correct atomic positions but the charge density and vibrational PDF may not be physically meaningful. The **TLS** method does not require more reflections but it is limited to correcting *distances* for a specific type of curvilinear motion and relies on accurate ADPs.

Each of the methods is also held back by mathematical considerations. The OPP method relies on a significant approximation that limits is use, while the Edgeworth series may diverge in reciprocal space (due to its exponential form) and has no closed form in real space. Some of these deficiencies could be overcome using numerical methods, which were not considered feasible when these methods were first developed. Any statistical method that involves polynomials with odd powers, including the GC series, may also lead to a PDF with negative regions. Kuhs argued that such regions are acceptable if they are far from the nucleus and within experimental error.[14] The most flexible method is the Gram-Charlier series being preferred by a number of authors,[14,29,37] and it is the method recommended by the IUCr's ADP nomenclature committee.[13] The Edgeworth and Gram-Charlier series are available in the XD2006,[33] PROMETHEUS[32] and Jana2006[38] codes but not in the two most widely used codes, SHELX[39] and CRYSTALS.[23]

Visualisation of the PDF resulting from anharmonic refinements can also be an issue. The definition of constant probability surfaces is more cumbersome in the anharmonic case and visualising the analytical surface is not readily possible. The surfaces could be visualised using numerically calculated surfaces and interpolation. The differences between an anharmonic and harmonic PDF may not be discernible visually despite a dramatic effect on the positional parameters.

Interpreting the refined parameters also poses difficulties. In a normal refinement the mean and variance of the distribution are the fitting parameters of the trivariate Gaussian, and their uncertainties are determined directly by the least-squares method. In an anharmonic refinement the true mean and variance are given by the moments of the anharmonic PDF or Debye-Waller factor, and may not be directly refined, complicating the analysis or derivation of their uncertainty.

1.4 Moving forward – a molecular dynamics approach

Improving the crystallographic description of thermal motion faces a number of challenges. Determining equilibrium structures requires more information than experimental methods alone can give. Developing and benchmarking current and new forms for $P(\mathbf{u})$ or $\hat{P}(\mathbf{H})$ requires detailed studies of very accurate neutron diffraction data. While experiment may yield enough data to refine a fourth-order Gram-Charlier series, to understand fully what parameters and forms are required, refinement of much higher order series may be necessary.

The natural step forward is to use theoretical means to further our understanding of the experimental process. The focus of this present work is to provide such an understanding using molecular dynamics (MD) simulations. The theoretical basis of MD will be provided in the following chapter but the method in essence allows one to simulation the dynamics of a system at the unit or supercell scale, providing trajectories of atomic motions that can be used to determine diffraction patterns and the atomic PDF's numerically, free of any approximations concerning thermal motion. The results of such simulations can be used to assess and develop anharmonic Debye-Waller factors. Such assessments benefit from the fact that we know the numerical forms for the analytical functions we seek. Also the MD simulations will yield time-averaged coordinates of the atoms. The differences between the theoretical time-averaged and equilibrium structures are corrections that can be applied to the experimental structure to determine experimental equilibrium structures for the first time.

MD simulations have been applied to study crystallographic systems previously mostly for the prediction of ADPs,[40] but also for probing the effects on anharmonic motion.[41,42] No concerted, detailed study has been carried out using MD simulations and with recent developments in experimental and theoretical methods such a study is timely.

Bibliography

[1] F. H. Allen, *Acta Cryst. B*, 2002, **58**, 380.

[2] T. Young, *Philos. Trans. R. Soc. London., Ser. A*, 1802, **92**, 12.

[3] M. von Laue, *Phys. Zeit.*, 1913, **14**, 1075.

[4] P. Debye, L. Bewilogua and F. Ehrhardt, *Phys. Zeit.*, 1929, **30**, 84.

[5] (*a*) P. Debye, *Ann. d. Phys.*, 1913, **348**, 49; (*b*) I. Waller, *Z. Phys. A*, 1923, **17**, 398.

[6] D. W. J. Cruickshank, *Acta Cryst.*, 1956, **9**, 757.

[7] C. Hammond, *The Basics of Crystallography and Diffraction*, Oxford University Press, 2nd edn., 2001.

[8] C. Giacovazzo, H. L. Monaco, G. Artioli, D. Viterbo, G. Ferraris, G. Gilli, G. Zanotti and M. Catti, *Fundamentals of Crystallography*, Oxford University Press, 2nd edn., 2002.

[9] D. T. Cromer and J. B. Mann, *Acta Cryst. A*, 1968, **24**, 321.

[10] G. L. Squires, *Introduction to the theory of thermal neutron scattering*, Dover Publications, 1978.

[11] I. Hargittai, in *Stereochemical applications of gas-phase electron diffraction: Part A The electron diffraction technique*, ed. I. Hargittai and M. Hargittai, VCH Publishers, 1988, ch. A survey: the gas-phase electron diffraction technique of molecular structure determination, p. 1.

[12] E. E. Castellano and P. Main, *Acta Cryst. A*, 1985, **41**, 156.

[13] K. N. Trueblood, H. B. Bürgi, H. Burzlaff, J. D. Dunitz, C. M. Gramaccioli, H. H. Schulz, U. Shmueli and S. C. Abrahams, *Acta Cryst. A*, 1996, **52**, 770.

[14] W. F. Kuhs, *Acta Cryst. A*, 1992, **48**, 80.

[15] *International Tables for Crystallography*, ed. A. J. C. Wilson, Kluwer Academic Publishers, 1995, vol. C, p. 505.

[16] C. K. Johnson, *Acta Cryst. A*, 1969, **25**, 187.

[17] M. J. Kronenburg, *Acta. Cryst. A*, 2004, **60**, 250.

[18] A. Einstein, *Annal. Phys.*, 1916, **354**, 769.

[19] V. Schomaker and K. N. Trueblood, *Acta Cryst. B*, 1968, **24**, 63–76.

[20] G. S. Pawley, *Acta Cryst. A*, 1970, **26**, 289.

[21] H. B. Bürgi, *Annu. Rev. Phys. Chem.*, 2000, **51**, 275.

[22] K. N. Trueblood and E. Huber-Buser, *THMA11. Program for Thermal Motion Analysis. UCLA, USA.*, 1987.

[23] P. W. Betteridge, J. R. Carruthers, R. I. Cooper, K. Prout and D. J. Watkin, *J. Appl. Cryst.*, 2003, **36**, 1487.

[24] B. T. M. Willis and G. S. Pawley, *Acta Cryst. A*, 1970, **26**, 254.

[25] G. S. Pawley and B. T. M. Willis, *Acta Cryst. A*, 1970, **26**, 260.

[26] B. T. M. Willis, *Acta Cryst. A*, 1969, **25**, 277.

[27] K. Tanaka and F. Marumo, *Acta Cryst. A*, 1983, **39**, 631.

[28] *Higher Transcendental Functions*, ed. A. Erdélyi, McGraw-Hill Book Company, 1953, vol. 2.

[29] U. H. Zucker and H. H. Schulz, *Acta Cryst. A*, 1982, **38**, 563.

[30] P. I. Kuznetsov, R. L. Stratonovich and V. I. Tikhonov, *Theory of Probability and its Applications*, 1960, **5**, 80.

[31] C. Scheringer, *Acta Cryst. A*, 1986, **42**, 356.

[32] U. H. Zucker, E. Perenthaler, W. F. Kuhs, R. Bachmann and H. Schulz, *J. Appl. Cryst.*, 1983, **13**, 358.

[33] A. Volkov, P. Macchi, L. J. Farrugia, C. Gatti, P. Mallinson, T. Richter and T. Koritsanszky, *XD2006*, 2006.

[34] W. F. Kuhs, *Acta Cryst. A*, 1983, **39**, 148.

[35] F. Y. Edgeworth, *Proc. Cambridge Phil. Soc.*, 1905, **20**, 36.

[36] G. Ferguson, *Acta Cryst. C*, 2008, **64**, e2.

[37] U. H. Zucker and H. H. Schulz, *Acta Cryst. A*, 1982, **38**, 568.

[38] V. Petricek, M. Dusek and L. Palantinus, *Jana2006. The crystallographic computing system. Institute of Physics, Praha, Czech Republic.*, 2006.

[39] G. M. Sheldrick, *Acta Cryst. A*, 1990, **46**, 467.

[40] N. M. Glykos, *Acta Cryst. D*, 2007, **63**, 705.

[41] J. v. Eerden, S. Harkema and D. Feil, *Acta Cryst. B*, 1990, **46**, 222.

[42] A. Alberti, E. Fois and A. Gamba, *Am. Mineral.*, 2003, **88**, 1.

Chapter 2

Computational techniques for the study of solids

2.1 Introduction

There is a plethora of computational methods that can be applied to study chemical systems. The following section outlines a number of these methods with a particular focus on performing solid-state simulations that make up the bulk of the work presented in later chapters. Section 2.3 details the molecular dynamics technique that can apply these various computational methods to probe the dynamic behaviour of chemical systems.

2.2 Introduction to computational chemistry

The principal aim of most computational chemical theories is to calculate the total energy, E, of a molecule, lattice or other form of chemical system. From the energy the atomic forces can be determined:

$$f_n = -\frac{\partial E}{\partial x_n}. \tag{2.1}$$

The sophistication with which the energy is evaluated ranges from full quantum mechanical treatments to simple pair-potential models. The more sophisticated methods yield molecular orbitals and the electron density. Knowledge of the forces, energies and electronic properties of a system can be used to determine a wealth of information including equilibrium geometries, vibrational and electronic spectra and the energetics and dynamics of reactions.

2.2.1 *Ab initio* methods

Ab initio methods aim to determine E from first principles through the solution of the time-independent Schrödinger equation:[1]

$$\hat{\mathcal{H}}\Phi = E\Phi \tag{2.2}$$

where $\hat{\mathcal{H}}$ is the Hamiltonian operator and Φ is the wavefunction that describes the system of interest. This is an eigenvalue equation. The Hamiltonian operator is the sum of the potential and kinetic energy operators, $\hat{U}$ and $\hat{K}$. The full form of the Schrödinger equation includes the full dynamic interactions between the nuclei and electrons. The majority of static quantum chemical calculations, and all those presented in this thesis, use the Born-Oppenheimer approximation[2] whereby the nuclear and electron degrees of freedom are separated and we deal with the electrons in a field of fixed nuclei. The approximation is valid because the differences in the masses of the nuclei and electrons mean that the electron dynamics occur on a much faster time-scale. The electronic Schrödinger equation, for a n-electron system, in atomic units,[2,3] is given by

$$\left[-\sum_{i=1}^{n}\tfrac{1}{2}\nabla_i^2-\sum_{i=1}^{n}\sum_{A=1}^{M}\frac{Z_A}{r_{iA}}+\sum_{i=1}^{n}\sum_{i>j}^{n}\frac{1}{r_{ij}}\right]\Phi_{\mathrm{elec}}=E_{\mathrm{elec}}\Phi_{\mathrm{elec}} \tag{2.3}$$

where the subscripts i and A refer to electrons and nuclei respectively, Z_A is the nuclear charge and r_{ij} is the separation of the i^{th} and j^{th} particle in the system. The first term in Equation 2.3 is the kinetic energy operator, the second details the electrostatic interaction between the nuclei and the electrons, while the third is the electrostatic interaction between electrons. The Schrödinger equation can only be solved analytically for one electron systems due to the form of the electron-electron electrostatic interaction. It may be solved numerically for many electron systems using a variety of theories that approximate the Columbic interaction. It is also impossible to determine a closed form for the electronic wavefunction Φ_{elec} so an approximate form must therefore be used, usually based on a product of molecular orbitals (MOs). In general, any MO, ϕ_i, may be approximated using a linear combination of simple or basis functions:

$$\phi_i=\sum_{j=1}^{\infty}c_j\chi_j \tag{2.4}$$

where c_i is the expansion coefficient for the j^{th} basis function. In general the expansion in Equation 2.4 is limited to a few well-chosen functions. Various types of basis functions, referred to as basis sets, have been proposed. An important requirement for the total wavefunction is that it obeys the Pauli Exclusion principle, which requires that Φ is antisymmetric to the exchange of two electrons. This can be achieved by using a Slater determinate comprised of the MOs.[2] A manifestation of this principle is the requirement that only two electrons of opposite spin occupy an orbital. Some common basis sets will be detailed in Section 2.2.3.

Hartree-Fock (HF) theory approximates the Columbic interaction using mean-field theory. The electrostatic interaction between two electrons, V_{ee}, is described as the interaction of an electron with the continuous charge distribution, ρ, of the other electrons in the system:

$$\hat{V}_{\mathrm{ee,\ HF}} = \sum_{i=2}^{n} \int \frac{\rho(\mathbf{r}_i)}{r_{1i}}\, d\mathbf{r}_i. \tag{2.5}$$

Equation 2.5 treats each atom independently and ignores the potential for correlation between electrons. Using a basis set that enforces the antisymmetry principle results in a term for electron "exchange" appearing in the HF Hamiltonian. The Hamiltonian arising from the HF approximation is best derived using an example such as the He atom, as detailed in full by Levine[3] or Szabo and Otslund.[2] The resulting Hamiltonian is formulated as a summation of one-electron Hamiltonians (called the Fock operator, $\hat{F}$ in HF theory):

$$\hat{H}_{\mathrm{HF}} = \sum_{i=1}^{n} \hat{F}(1) = \sum_{i=1}^{n} \left[\hat{h}_{\mathrm{core}} + \sum_{i=1}^{n/2} (2\hat{J}_i(1) - \hat{K}_i(1)) \right], \tag{2.6}$$

where the numbers in brackets [*e.g.* (1)] indicates the electron of the MO, the summations run to $n/2$ to account for the fact that two electrons occupy each orbital and $\hat{h}_{\mathrm{core}}$ is the sum of the kinetic and electron-nuclear operators given by:

$$\hat{h}_{\mathrm{core}} = \tfrac{1}{2}\nabla_i^2 - \sum_{A=1}^{M} \frac{Z_A}{r_{iA}}. \tag{2.7}$$

This one-electron Hamiltonian operates on an orbital to yield its energy:

$$\hat{F}(1)\phi_i(1) = \varepsilon_i \phi_i(1). \tag{2.8}$$

$\hat{J}$ in Equation 2.6 is the Columb operator, which stems from the approximation of Equation 2.5. It is defined as

$$\hat{J}_j(1)f(1) = f(1)\int |\phi_i(2)|^2 \frac{1}{r_{12}}\,dv_2 \tag{2.9}$$

with $f(1)$ being an arbitrary function and the integral being taken over all space of electron 2, v_2. $\hat{K}$ is the exchange operator that arises from the antisymmetry principle:

$$\hat{K}_j(1)f(1) = \phi_j(1)\int \frac{\phi_i^*(2)f(2)}{r_{12}}\,dv_2. \tag{2.10}$$

Inserting Equation 2.4 with b basis functions into Equation 2.8 we obtain

$$\hat{F}(1)\sum_{s=1}^{b} c_{si}\chi_s = \varepsilon_i \sum_{s=1}^{b} c_{si}\chi_s. \tag{2.11}$$

If we multiply by χ_r^* and integrate over all space we obtain the Roothaan equations:

$$\sum_{s=1}^{b}(c_{si}F_{rs} - \varepsilon_i S_{rs}) = 0, \quad r = 1, 2, 3, ..., b \tag{2.12}$$

where

$$F_{rs} \equiv \int \chi_r^* \hat{F}\chi_s\,dv, \qquad S_{rs} \equiv \int \chi_r^*\chi_s\,dv. \tag{2.13}$$

S_{rs} indicates the overlap between the r^{th} and s^{th} basis functions. Equation 2.12 gives a set of b simultaneous equations with b unknowns (the MO coefficients c_i) which is best solved using matrix methods.[3] The Fock matrix elements can be computationally intensive to determine as inserting Equation 2.4 into the equations for $\hat{K}$ and $\hat{J}$ leads to integrals, centred on one to four different basis functions, that are time-consuming to evaluate. The result of solving the Roothaan equations is b MO's with energies ε_i. If more than one basis function is used to represented each AO then many of these orbitals will be unoccupied. The total HF energy of the system, E_{HF}, is evaluated by summation of the occupied orbital energies taking into account double summations of the repulsion integrals. As the $\hat{F}$ operator is dependent on the orbitals, the Hartree-Fock formulation of the Schrödinger equation cannot be solved directly. Instead it is solved in an iterative fashion, refining an initial guess wavefunction in a self-consistent manner, which is often referred to as the self-consistent field (SCF) method.

The neglect of full electron correlation is the main deficiency of HF theory and there are numerous methods for incorporating electron correlation into the SCF process. Those that use the HF solution as an initial solution are referred to as the post Hartree-Fock methods. One example is configuration interaction (CI), which expands the true wavefunction as being a summation of HF solutions of the system in the ground state (Ψ_0) and various excited electronic configurations ($\Psi_n\ ;\ n \geq 1$)

$$\Phi_{\mathrm{CI}} = c_0\Psi_0 + c_1\Psi_1 + c_2\Psi_2 + \cdots\ . \tag{2.14}$$

The summation may be truncated at various levels of excited configuration to lead to various forms of CI. Full CI, taken over all possible configurations is an exact method within the limitations of the basis set used to represent each configuration. As such it is an important benchmarking tool. However, its practical use is limited to only very small systems. Truncated CI calculations suffered from a number of problems, most notably that some of them are not size consistent. This property means that the total energy is proportional to the size of the molecule and is important for comparing the energies of different molecules.[3] Other methods for including correlation include perturbation theory, usually in the form of Møller-Plesset Theory[4] (MP2 and higher) and coupled-cluster methods.[2,3]

2.2.2 The Hellmann-Feynman theorem

Quantum chemistry methods give the total energy of the system directly. However, it is also important to know how the energy changes with respect to specific parameters. For a parameter, λ, in a Hamiltonian, $\hat{\mathcal{H}}$, that operates on a system described by the wavefunction Φ, the generalised Hellmann-Feynman theorem[3] states that

$$\frac{\partial E}{\partial \lambda} = \int \Phi^* \frac{\partial \hat{\mathcal{H}}}{\partial \lambda} \Phi \, \mathrm{d}\tau. \tag{2.15}$$

This theorem can then be applied to molecular systems to give the Hellmann-Feynman electrostatic theorem, that shows the force acting upon a nucleus to be the sum of the Coulombic forces exerted by the other nuclei and the electron cloud determined by solving the time-independent Schrödinger equation (Equation 2.2). This important theorem permits the direct calculation of forces in QM calculations, which is essential for the molecular-dynamics method. Forces may also be evaluated using finite displacements but this is unsuitable for molecular-dynamics simulations (Section 2.3), which can be computationally intensive without the need for multiple evaluations of the energy at each step.

2.2.3 Basis sets

The choice of basis set is very important for a calculation and has as much bearing on the accuracy of the result as the level of theory chosen. As stated above in Section 2.2.1, the wavefunction of the system is expanded as the summation of a finite number of appropriate functions. For molecular systems this often takes the form of a linear combination of atomic-like orbitals (LCAO). Slater-type orbitals (STO's) are a simple and intuitive basis set based on the analytical wavefunctions for the one-electron system:[5]

$$\phi_{\mathrm{STO}} = N r^{n-1} \exp(-\zeta r) Y_l^m(\theta, \psi), \tag{2.16}$$

where Y_l^m is a spherical harmonic of degree l and order m. While the STO basis set is intuitive, the integrals that result from its use can be time-consuming to evaluate numerically due to the large number of multi-site integrals that result. The most commonly used type of basis set in isolated-molecule calculations are comprised of Gaussian-type orbitals (GTOs).[3,6] An orbital centred on nucleus b, with coordinates x_b, y_b and z_b, can be represented by a series of Cartesian Gaussians of the form:

$$g_{ijk} = N x_b^i y_b^j z_b^k \exp(-\alpha r_b^2), \tag{2.17}$$

where N is normalisation constant, α is the positive orbital exponent, and the positive integers, i, j and k, denote the type of orbital. The sum $i + j + k = 0$

gives an s orbital, $i + j + k = 1$ yields a p orbital and so on. A single Gaussian function does not approximate the form of an atomic orbital (AO) very well so more that one Gaussian is required to model orbitals. However, it can be shown that all multi-centre integrals involving Gaussians reduce to two-centre integrals, which are far less computationally demanding; multiple Gaussians can be used to model an AO accurately with a significant speed-up compared to STO calculations. Much of the work on GTOs was done by Pople and co-workers, who introduced many of the standard basis sets, *e.g.* 6–31G*,[7] used in quantum chemistry. Extra functions are typically added to the GTOs to account for the polarisable and diffuse nature of valence orbitals in larger atoms. Optimised basis sets are available for most potential applications in quantum chemistry. For post-HF methods the correlation-consistent basis sets of Dunning and co-workers are quite popular.[8]

For calculations on periodic systems, such as crystals, a periodic basis is often preferable. Instead of using atom-centred orbitals a plane-wave basis can also be used:

$$\phi_{\mathrm{PW}} = c \times \exp(-i\mathbf{G} \cdot \mathbf{r}), \tag{2.18}$$

with $\mathbf{G}$ being the plane-wave vector. The quality of a plane-wave basis set is determined by the cut-off energy, E_{cut}, which describes the highest energy wave-vector that is included in the basis-set summation in Equation 2.4. A higher energy means a shorter wavelength allowing the plane-wave basis set to model the more detailed features of the wavefunction.

2.2.4 Solid-state calculations

The electronic structure of a periodic solid is much more complicated than that of an isolated molecule. This is because the electronic wavefunctions extend over the effectively infinite range of the crystal lattice. The combination of atomic orbitals from different cells, some of which are in phase and others which are out of phase, leads to wavefunctions with periods longer than a unit cell.

To deal with these wavefunctions we can again turn to the reciprocal space of the infinite lattice (Section 1.2). Here, spatially infinite wavefunctions are reduced to particular points in k-space, where the value of the wave-vector, $\mathbf{k}$, denotes the period of the wavefunction. For a given value of $\mathbf{k}$ there are potentially a large number of wavefunctions resulting from LCAO within cells. A wavefunction where AO's from different cells are combined in phase is located at the centre of the Brillouin zone, the Γ-point (0, 0, 0). For a cubic system with lattice length, a, a wavefunction involving alternating in-phase and out-of-phase AOs in all three directions has the wavevector $\frac{2\pi}{a} \times (\frac{1}{2}, \frac{1}{2}, \frac{1}{2})$. To calculate the electronic structure of a solid we make use of Bloch's theorem,[9] which allows us to represent our electronic wavefunction as the product of a lattice periodic function, $f(\mathbf{r})$, and a wave-like part that accounts for the position we are sampling in the Brillouin zone:

$$\Psi(\mathbf{r}) = \sum_{k} \exp(i\mathbf{k} \cdot \mathbf{r}) f(\mathbf{r}) \tag{2.19}$$

From this equation we can see that all of the wavefunctions of the system can be described by confining $\mathbf{k}$ to the range 0 to 1 ($\times\frac{2\pi}{a}$). The problem of determining an infinite number of wavefunctions is reduced to that of determining a finite number of wavefunctions at an infinite number of k-points. However, in practice we can sample the Brillouin zone using a finite mesh of k-points and interpolate the result to obtain an accurate solution. A number of schemes are available for choosing the important k-points including the widely used Monkhorst-Pack (MP) grid method.[10]

2.2.5 Pseudopotentials

In any electronic structure calculation the bottleneck is the number of wavefunctions required and so a major consideration in solid-state calculations, or those isolated-molecule calculations involving large atoms, is to reduce this number. This is done by treating only the valence electrons, which are the most important for describing chemical properties. By treating only the valence electrons we remove the real ionic potential and replace it with a weaker pseudopotential (PP) that makes the valence electrons behave as if the core electrons were present.

The real ionic potential makes the valence wavefunctions oscillate near the nucleus (to preserve orthogonality with the core wavefunctions). The near-nucleus oscillations mean that many more plane waves or more complex GTO's are required to depict it accurately. With the PP we smooth the inner-most part of the wavefunction (removing nodes *etc.*) to reduce the required number of plane waves or Gaussian primitives used.[9] This is subject to the assumption that the properties of the real and pseudo wavefunctions are the same in the core region we are smoothing and that the real potentials and pseudopotentials are the same outside this core region. PP's were originally developed for use with plane-wave basis-set calculations of solids and are now nearly universally used in solid-sate calculations due to the significant computational speed-up they garner.

One of the constraints applied in the original formulation of PPs was that the charge of the real potential was conserved by the pseudopotential. PPs generated in this fashion are termed norm-conserving and include the Martins-Troullier[11] PP's commonly used in the CPMD program.[12] This constraint limits the amount of smoothing that can be applied to the PP. Vanderbilt[13] relaxed this constraint to make ultrasoft pseudopotentials. With these much smoother potentials a significantly smaller basis set (*i.e.* smaller value of E_{cut}) can be used, greatly speeding up the computation. However, the charge omitted from the potential must be re-introduced later. This requires significant theoretical and coding effort and as a result many computational chemistry codes have limited ultrasoft-pseudopotential support.

2.2.6 Density-functional theory

Density-functional theory (DFT) is one of the most successful and widely used methods in theoretical chemistry.[14] The key concept exploited by DFT is that the ground-state energy and electronic properties of the system are functions of the ground-state electron density, $\rho_0(\mathbf{r})$. A functional is an expression that relates a function [*e.g.* $\rho_0(\mathbf{r})$] to a number and is usually denoted using square brackets (*e.g.* $F[\rho]$). It can also be shown that the energy of the system changes in a variational manner with the electron density. This means that the most likely form for ρ is that which gives the lowest ground-state energy, E_0. These concepts are known as the Hohenburg-Kohn theorems.[15]

Kohn and Sham built upon these ideas to give the method applied today in DFT.[16] They considered a non-interacting system of n electrons with the one-electron Hamiltonian (in atomic units),

$$\hat{h}_{\mathrm{s}} = \left[-\tfrac{1}{2}\nabla_i^2 - \sum_{A=1}^{M} \frac{Z_A}{r_{1A}} + \int \frac{\rho(\mathbf{r}')}{r_{1'}}\, d\mathbf{r}' \right], \tag{2.20}$$

where the first term represents the kinetic-energy operator, the second term is the interaction between the electrons and the A nuclei and the third term is the interelectronic repulsion operator of the non-interacting system (whose charge is smeared out into a continuous distribution). The assumption in Kohn-Sham DFT (KS-DFT) is that there is some potential, $v_{\mathrm{xc}}(\mathbf{r})$, that can be added to this Hamiltonian that results in the non-interacting system's electron density equalling that of the real system. This term accounts for the exchange and correlation that occurs in the real, interacting system and has the form:

$$v_{\mathrm{xc}}(\mathbf{r}) = \frac{\partial E_{\mathrm{xc}}[\rho(\mathbf{r})]}{\partial \rho(\mathbf{r}),} \tag{2.21}$$

where E_{xc} is the exchange-correlation (XC) energy given by:

$$E_{\mathrm{xc}}[\rho] = \int \rho(\mathbf{r})\epsilon_{\mathrm{xc}}(\rho)\, \mathrm{d}\mathbf{r}, \tag{2.22}$$

with $\epsilon_{\mathrm{xc}}(\rho)$ being the XC energy per electron in the system of interest. The exact form of the XC potential is unknown. It if were known then DFT would give exact results. The term $v_{\mathrm{xc}}(\mathbf{r})$ can be used to describe a set of Kohn-Sham (KS) orbitals,

$$\left[\hat{h}_{\mathrm{s}} + v_{\mathrm{xc}}\right] \psi_i^{\mathrm{KS}} = \varepsilon_i^{\mathrm{KS}} \psi_i^{\mathrm{KS}}, \tag{2.23}$$

from which the ground-state energy and electron density may be calculated. For isolated molecules the same types of STO's and GTO's used in HF and post-HF methods can be used to represent the KS orbitals. Plane-wave basis sets are often used in standard DFT simulations of solids as many parts of the calculation can be performed efficiently using them in conjunction with fast-Fourier transform (FFT) techniques.

Determining a suitable form for $v_{\mathrm{xc}}(\mathbf{r})$ has been a focus of research for numerous chemists and physicists since the Hohenburg-Kohn theorems where first postulated and a number of expressions for it have been derived. The local-density approximation (LDA) assumes that E_{xc} for a particular ρ can be determined from the E_{xc} for a homogeneous electron gas, jellium, which has the same ρ. For jellium, ϵ_{xc} as a function of ρ has been accurately determined using Monte-Carlo simulations.[17] In Equation 2.22 E_{xc} is a function of how ρ changes over space. LDA assumes that ρ varies slowly over space so that the local electron density is homogeneous as is the case for jellium. LDA is quite useful for metals as the electron density is smeared out and reasonably uniform. For molecular systems, however, ρ will change over small distances due to the more discrete nature of molecules and so LDA is a poor approximation. This can be overcome with the generalised-gradient approximation (GGA), which includes the gradient of ρ to account for it rapidly changing over space. Naturally, this leads to much more complex equations for the exchange-correlation functional and in some cases GGA functionals are parametrised.[3] The GGA also has some limitations. In particular van der Waals dispersion forces are poorly described by all mainstream LDA and GGA functionals. Dispersion forces depend on long-range interactions between electrons, requiring an understanding of how ρ changes over large distances in our system. GGA, while including information about the gradient, is still essentially a semi-local method and neglects long-range effects on E_{xc}.

It is possible to separate the exchange and correlation parts of the functional such that $E_{\mathrm{xc}} = E_{\mathrm{x}} + E_{\mathrm{c}}$. This allows mixing of different functionals and also the use of exact Hartree-Fock exchange energies. Functionals that incorporate some form of exact exchange are called “hybrid functionals”. B3LYP is a widely used hybrid functional parametrised for organic systems.[18]

The XC functional can involve more complex expressions than HF theory. The

DFT Hamiltonian is dependent only on the three positional coordinates of the electron density as opposed to the $3N$ coordinates that are required for dealing with orbitals, greatly simplifying calculations. The use of hybrid functionals can significantly slow a calculation as it requires the explicit evaluation of the exchange integral for each *basis function.* In solid-state simulations this can be a severe restriction due to the number of AO's and resultant MO's and as a result hybrid-DFT and HF simulations of solids are far less common than normal DFT simulations of solids. In particular, a plane-wave basis is unsuitable for hybrid-functional calculations as the number of plane waves in the basis can be upwards of 10,000, compared to the Gaussian-type basis sets that would typically comprise $1/20^{\text{th}}$ of this.

2.2.7 Empirical "force-field" calculations

Despite the many advances in computational software and hardware, methods based on quantum theory remain time-consuming. An alternative approach is to use simple analytical or tabulated potentials to describe interactions between atoms. In molecular systems a number of different potentials are used to model the various types of interactions that make up the real system:

$$V_{\text{total}} = V_{\text{bonds}} + V_{\text{bends}} + V_{\text{torsions}} + V_{\text{eletrostatic}} + V_{\text{vdW}} + \cdots . \tag{2.24}$$

Each interaction is modelled using a specific potential defined by a number of parameters. The complete set of potentials and parameters is often referred to as a "force field" (FF). Most force fields utilise pair potentials, where the potential energy depends only on the distances between atom pairs. A number of generic parameter sets are available, including the MM and AMBER series.[19,20]

To model a bond between two atoms a simple harmonic potential, $V(r) = kr^2$, may be used. Anharmonicity can be incorporated using a Morse potential or a higher order polynomial expression (often quadratic). Bending motions can be reproduced using similar potentials dependent on bond angles. Torsions, inversions and other forms of motion can also be explicitly defined. Electrostatic interactions are modelled by associating a point charge with each atom in the system. The interaction energy can be evaluated using the usual Columbic expression:

$$V(r)_{\mathrm{Col}} = \frac{q_1 q_2}{r}, \tag{2.25}$$

where r is the distance between atoms 1 and 2 that have charges q_1 and q_2 respectively. The expression in Equation 2.25 is evaluated in a double summation over all atoms and often converges slowly. It is usually replaced by some variation on the Ewald sum method, which breaks the long-range real space summation into more efficient real and reciprocal space components.[21] The long-range interactions are typically modelled using a potential that is repulsive at small r and attractive at intermediate distances. A number of different potential forms are used, including the Lennard-Jones potential and the Buckingham potential:[21,22]

$$\begin{aligned} V(r)_{\mathrm{LJ}} &= 4\varepsilon\left[\left(\frac{\sigma}{r}\right)^{12} - \left(\frac{\sigma}{r}\right)^{6}\right] && (2.26)\\ V(r)_{\mathrm{buck}} &= A\exp(-Br) - \left(\frac{C}{r^6}\right). && (2.27)\end{aligned}$$

The fitting parameters in the potential can be determined in a variety of ways. For simple systems the parameters may be adjusted to reproduce experimental observations including structural and spectroscopic data. It is now common to use *ab initio* or DFT calculations, particularly when generating a force field specific to a molecule or a small set of molecules. Most fitting procedures use some form of self-consistent least-squares analysis to reproduce various physical properties of the desired system. Despite the many sophisticated methods for determining force fields, there is no guarantee that the property of interest will be correctly modelled by the force field.

Force fields are far less computationally demanding than QM methods and can be used to study a range of systems and time-scales inaccessible to DFT and *ab initio* methods alone. As an example, a simulation of the unit cell of phase-I ND_3 with DFT might take 4 days using 8 processors in parallel. The corresponding force field simulation would take less than half an hour on a single processor. However, force field simulations are naturally less robust than QM methods.

Traditional force fields are limited to systems where no chemical reactions occur, *i.e.* no bond breaking or forming. Reactive force fields, such as ReaxFF,[23] can be used to overcome this limitation but more parametrisation is required for meaningful results. Polarisable force fields are also available to model electrostatic interactions more realistically.

2.2.8 Semi-empirical methods

Semi-smpirical (SE) methods represent a balance between QM and empirical-potential approaches. SE methods usually treat only the valence electrons of the system using a Hamiltonian, which neglects certain interactions and/or parametrises others. The earliest SE methods such as Hückel theory and the Pariser-Parr-Pople method, treated the π electrons of aromatic hydrocarbons and yielded reasonable qualitative results.[3] A variety of methods have been developed that extend the basic principles of these methods to non-planar hydrocarbons and more recently the majority of the periodic table.

Extended Hückel theory (EHT) was developed by Hoffmann in 1963.[24] This method treats only the valence electrons of H and C atoms. STOs are used to represent the H atom $1s$ orbitals and the $2s$ and $2p$ orbitals of the C atom. The ETH MO's are determined using the Roothaan equations (Equation 2.12) but with the Fock operator replaced by an effective Hamiltonian,

$$\sum_{s=1}^{b}(c_{si}H_{rs}^{\text{eff}} - \varepsilon_i S_{rs}) = 0, \quad r = 1, 2, 3, ..., b. \tag{2.28}$$

H_{rs}^{eff} is not explicitly defined. For $r = s$ it is taken as the valence-state ionisation potential (VSIP) of the r^{th} AO.[3] The off-diagonal elements are given by:

$$H_{rs}^{\text{eff}} = \frac{1}{2}K(H_{rr}^{\text{eff}} + H_{ss}^{\text{eff}})S_{rs}, \tag{2.29}$$

where K is a general scaling constant.

More sophisticated methods were developed by Pople and co-workers using an explicit Hamiltonian, which features the electron-electron repulsion operator $\frac{1}{r_{12}}$.

Inclusion of this operator leads to all of the computationally intensive one- and two-electron integrals (ranging from one- to four-centre integrals) that result in HF theory so some of these integrals are “neglected”, often using the zero differential overlap approximation:

$$f_r^*(1) f_s(1)\,\mathrm{d}v_1 = 0, \quad r \neq s. \tag{2.30}$$

The core Hamiltonian is approximated using some form of spectroscopic data (often VSIP as in ETH). The aim of these methods was to reproduce small-basis HF calculations at a fraction of the computational cost. The complete neglect of differential overlap (CNDO) method[25] neglects all overlap between different orbitals (thus removing the majority of repulsion integrals), while the intermediate neglect of differential overlap (INDO) method[26] includes overlap between basis functions on the same atom but only in one-centre integrals. Pople *et al.* also suggested the neglect of diatomic differential overlap (NDDO) method[25] where all overlap is included for orbitals on the same atom in two-centre repulsion integrals. As these methods were aimed at reproducing low-level HF calculations they provide reasonable results for molecular geometries but not for binding energies and other quantities where HF theory is likely to fail.

More recent work on semi-empirical methods has focused on parametrising them to provide binding energies and thermochemical properties to within the “chemical accuracy” that research into higher levels of theory is still trying to achieve (~ 1 kcal mol^{-1}).[3] These SE methods were based on the INDO and NDDO methods but with many of the repulsion integrals derived in some manner from atomic spectra or, especially for more recent methods, used as fitting parameters to experimental and *ab initio* results. The modified neglect of diatomic overlap (MNDO) method[27] was the first widely-used SE method parameterised to provide accurate thermochemical properties with average errors for a set of C, H, O and N containing compounds of 6.3 kcal mol^{-1} in heats of formation, 0.014 Å in bond lengths and 2.8° in bond angles. Most SE methods use only s- and p-type basis functions. The MNDO/d method[28] adds d oribtials to second row and larger atoms improving the accuracy of results.

The most recent SE method is PM6 (parameterised method 6).[29] This method was based on the earlier PM3 method,[30] which itself was derived from MNDO. In PM6 many of the electron repulsion integrals are treated as fitting parameters to mimic experimental structures (both gas phase and solid state) and heats of formation. Specific corrections were made for inaccurate geometries or interactions and unlike previous PM methods *d* orbitals were used for all non-first row atoms.

SE methods have found considerable use in studying large systems although primarily using static calculations or geometry optimisations. A number of SE methods have been recently implemented in the CP2K program[31] for use in isolated-molecule MD simulations.

2.3 Molecular dynamics simulations

The molecular dynamics (MD) method is a powerful and rich method for exploring the dynamics and statistical thermodynamics of chemical systems. There are many variants and applications of MD but the underlying principle is to use some level of chemical theory to determine the forces acting upon atoms in a representation of the molecular system, *e.g.* the unit cell of a crystal, and to use these forces to evolve the system such that it behaves just as the real system should.

The two most important aspects of MD simulations are the manner in which the dynamics is performed and the type of theory used. The evolution of a system of particles with positions, $\mathbf{r}$, and momenta, $\mathbf{p}$, can be described using the Lagrangian equation[21]

$$\frac{\mathrm{d}}{\mathrm{d}t}\frac{\partial \mathcal{L}}{\partial \dot{\mathbf{r}}_k} - \frac{\partial \mathcal{L}}{\partial \mathbf{r}_k} = 0 \tag{2.31}$$

where the Lagrangian function is given by the potential and kinetic energies

$$\mathcal{L} = K - V. \tag{2.32}$$

From this equation we can derive a series of $3N$ second-order differential equations, $m\ddot{\mathbf{r}} = \mathbf{f}$, that relate positions to forces. Alternatively the Hamiltonian, $\mathcal{H}$, can be used to derive $6N$ first-order differential equations.[21] These differential equations are solved using finite difference methods in which we solve and integrate the equations of motions at suitably small intervals. There are numerous integration schemes but many molecular dynamics simulation codes still use the simple Verlet algorithm[32] or modifications of it.[21] The Verlet leapfrog algorithm can be written as:

$$\begin{aligned} \mathbf{r}(t+\delta t) &= \mathbf{r}(t) + \delta t \mathbf{v}(t+\tfrac{1}{2}\delta t) && (2.33) \\ \mathbf{v}(t+\tfrac{1}{2}\delta t) &= \mathbf{v}(t-\tfrac{1}{2}\delta t) + \delta t \mathbf{a}(t). && (2.34) \end{aligned}$$

Its name originates from the manner in which the evaluation of the velocities and positions “leap-frog” each other. The system is initialised at a time $t - \frac{1}{2}t$ using velocities derived from the initial kinetic energy of the system and the Maxwell Boltzmann distribution.[33] The velocities at at a time t are determined using

$$\mathbf{v}(t) = \tfrac{1}{2}\left(\mathbf{v}(t+\tfrac{1}{2}\delta t) + \mathbf{v}(t-\tfrac{1}{2}\delta t)\right). \tag{2.35}$$

The timestep, δt, is chosen so that the iterative solution of Equations 2.33 and 2.34 leads to a smooth and stable trajectory. This can be achieved by sampling the system at an interval 10 to 15 times smaller than the highest frequency vibration. The most time-consuming process in an MD simulation is the evaluation of the forces to determine $\mathbf{a}(t)$. High-frequency vibrations can be a hindrance when studying some systems, *e.g.* organic systems with νC–H *circa* 3000 cm^{-1}, as the phenomenon of interest may occur at much longer time-scales, requiring many force evaluations. It is possible to constrain flexible degrees of freedom to increase the timestep,[21,34,35] but this can only be performed when high-frequency motions are known not to influence the property or behaviour of interest.

2.3.1 Ensembles and thermostats

A statistical mechanical ensemble is a collection of systems of identical composition. These systems will each have a specified volume, temperature and energy that defines the type of ensemble. An ensemble in which the volume and energy of each system is identical is the micro-canonical ensemble, often referred to as the NVE ensemble, as the number of particles, volume and energy are constant. Each type of ensemble has a specific expression for its partition function, which can then be used to determine quantities such as the entropy and pressure.[21,36] The NPT ensemble with constant pressure and temperature is a good approximation to experimental conditions for diffraction studies as experimental set-ups are such that temperature and pressure should be constant.

If no external force interacts with a system in an MD simulation, then the total energy of each configuration should be conserved (*i.e.* the same). With a constant number of particles and constant volume, the MD simulation generates an NVE ensemble of systems. To generate an NVT ensemble, with constant temperature, the simulation must be coupled to a mathematical "heat bath", which acts as a thermostat. There are numerous schemes for achieving this including, amongst others, the Nosé-Hoover thermostat,[37] the "canonical sampling through velocity re-scaling" thermostat[38] and the Anderson thermostat.[39] All of these methods aim to adjust the kinetic energy, and hence temperature, of the system in a natural fashion. Constant pressure and temperature simulations in the NPT ensemble are performed using a barostat to control the pressure as well as a thermostat for the temperature. The practical details of thermostatting and NVT and NVE simulations will be discussed more in Chapter 3.

It is important when performing an MD simulation in a particular ensemble that the simulation explores the phase space of the system sufficiently. The phase space is the $6N$-dimensional space comprising all the positions and momenta in the system. A simulation that explores every possible phase-space configuration is said to be ergodic. In practice, exploring the complete phase space is impossible for all but the simplest of systems and in many cases is not necessary as the complete phase space may include thermodynamically or kinetically inaccessible states (*i.e.* other phases). It is still important that the simulation explores the relevant areas of the potential-energy surface properly. If this is the case then the MD time averages will be equivalent to the ensemble space averages. In simulations with thermostats, the application of the thermostat acts as a randomising force that can encourage ergodic behaviour. Stronger thermostatting will ensure ergodicity, yielding meaningful time averages. However, the true dynamical behaviour of the atoms will be lost as their velocities are altered regularly by the thermostat.

2.3.2 Car-Parrinello molecular dynamics

Standard *ab initio*/DFT-MD calculations proceed by evolving the atomic positions and recalculating the electronic ground-state wavefunctions. This is termed Born-Oppenheimer molecular dynamics (BOMD), as it separates the motions of the nuclei from the electronic wavefunctions. However, another approach to *ab initio*/DFT MD was developed by Car and Parrinello,[40] who proposed treating the electronic wavefunction as a fictitious particle and evolving it based on the forces acting upon it. They constructed an equation of motion for the electron wavefunctions:

$$\mu\ddot{\varphi}_i(\mathbf{r},t) = \frac{\delta E}{\delta\varphi_i(\mathbf{r},t)} + \sum_k \Lambda_k \varphi_k(\mathbf{r},t), \tag{2.36}$$

where μ is an inertia (*i.e.* like mass for a real particle), the first term represents the forces acting on the wavefunction, φ_i, and the second term represents constraints (Λ_k) on the wavefunction to ensure orthogonality with the k other wavefunctions. This elegant method allows the atomic positions and wavefunctions to be evolved in step and is now referred to as Car-Parrinello molecular dynamics (CPMD). CPMD simulation steps are usually much faster than BOMD steps as the electronic wavefunction is evolved rather than calculated from scratch as in BOMD. However, dynamic processes for electrons occur much faster than for nuclei (this is the basis of the Born-Oppenheimer approximation) and so a much smaller timestep (< 0.1 fs) is required for a CPMD simulation to converge properly. Predictor-corrector methods[21] are often used for extrapolation of the wavefunction in BOMD with the result being that CPMD and BOMD simulations can take roughly the same amount of time.

2.3.3 Path-integral molecular dynamics

The dynamics of the nuclei in normal MD simulations are evolved using purely Newtonian mechanics. Thus the treatment of the nuclei is purely classical; there is no zero-point energy (ZPE) contribution and QM tunnelling of particles is not possible. For some simulations, especially those in the high-T limit, neglect of ZPE and tunnelling effects is not a significant issue. However, for low temperature simulations or those of lighter particles the neglect of quantum dynamics can be a serious issue. Numerous lattice-dynamics studies of thermal motion in the solid state have shown that in some cases the zero-point contribution to an atom's anisotropic displacement parameters can be as large as 30–50% of the room temperature values.[41]

Path-integral molecular dynamics (PIMD) is a method widely used to simulate ensembles quantum mechanically. This method is based on the work of Feynman, who devised the path-integral formulation of quantum statistical mechanics.[42] In PI theory classical trajectories of particles are replaced by many quantum paths that the particle may take. Integration over these paths yields the correct quantum behaviour.

PIMD simulations stem from considering the canonical QM partition function, Z_{NVT}. For a one-dimensional system with Hamiltonian, $H = \frac{p^2}{2m} + v(x)$, Z is given by (in Dirac notation[2]):

$$Z_{NVT}(\beta) = \int \mathrm{d}x \left\langle x \,\middle|\, \mathrm{e}^{-\beta H} \,\middle|\, x \right\rangle, \tag{2.37}$$

$$Z_{NVT}(\beta) = \int \mathrm{d}x \left\langle x \,\middle|\, \mathrm{e}^{-\beta (K+V)} \,\middle|\, x \right\rangle,$$

where β is given by $1/k_\mathrm{b}T$ and K and V refer to the kinetic and potential energy parts of H. Application of Trotter's theorem:

$$e^{\lambda(A+B)} = \lim_{P\to\infty} \left[\mathrm{e}^{\frac{\lambda}{2P}B} \mathrm{e}^{\frac{\lambda}{P}A} \mathrm{e}^{\frac{\lambda}{2P}B} \right]^P , \tag{2.38}$$

leads, eventually, to the following expression for the partition function:[21,43]

$$\begin{aligned} Z_{NVT}(\beta) = \lim_{P\to\infty} & \left(\frac{mP}{2\pi\beta\hbar^2} \right)^{P/2} \int \mathrm{d}x_1 \cdots \mathrm{d}x_P \\ \times \exp & \left(- \sum_{i=1}^{P} \left[\frac{mP}{2\beta\hbar^2} (x_{i+1} - x_i)^2 + \frac{\beta}{P} v(x_i) \right] \right) , \quad x_{P+1} = x_1 \end{aligned} \tag{2.39}$$

where P is the Trotter dimension. Close examination of Equation 2.39 will show that Z for a particular value of P corresponds to the partition function of a purely classical system of P particles where nearest neighbour particles are joined by harmonic oscillators in a cyclical fashion. The P particles are often referred to as beads as the chain of particles resembles a necklace. This formulation of a quantum system in terms of a classical one is know as the *classical isomorphism.*[44,45] For a N-body system we obtain P replicas of the system which interact through the harmonic oscillations. As $P \to \infty$ the classical approximation of the quantum system becomes more accurate. There are a number of important aspects to performing PIMD simulations, in particular ensuring ergodicity, which require specific re-formulations of Equation 2.39 and strong thermostatting.[43] PIMD simulations are in principle exact if a sufficiently large value of P is used. However, it is important to stress that the path-integral formalism of Equation 2.39 yields only static, *i.e.* time-averaged, quantities. Recovering dynamic information such as correlation functions requires methods such as centroid MD[46] and ring-polymer MD.[47]

Bibliography

[1] E. Schrödinger, *Phys. Rev.*, 1926, **28**, 1049.

[2] A. Szabo and N. S. Ostlund, *Modern Quantum Chemistry: Introduction to Advanced Electron Structure Theory*, Dover Publications, 1996.

[3] I. N. Levine, *Quantum Chemistry*, Prentice Hall, 5th edn., 2000.

[4] C. Møller and M. S. Plesset, *Phys. Rev.*, 1934, **46**, 618.

[5] J. C. Slater, *Phys. Rev.*, 1930, **36**, 57.

[6] S. F. Boys, *Proc. R. Soc. Lond. A.*, 1950, **200**, 542.

[7] (*a*) W. J. Hehre, R. Ditchfield and J. A. Pople, *J. Chem. Phys.*, 1972, **56**, 2257; (*b*) P. C. Hariharan and J. A. Pople, *Theor. Chim. Acta*, 1973, **28**, 213; (*c*) M. S. Gordon, *Chem. Phys. Lett.*, 1980, **76**, 163.

[8] (*a*) T. H. Dunning, *J. Chem. Phys.*, 1989, **90**, 1007; (*b*) R. A. Kendall, T. H. Dunning and R. J. Harrison, *J. Chem. Phys.*, 1992, **90**, 6796; (*c*) D. E. Woon and T. H. Dunning, *J. Chem. Phys.*, 1993, **98**, 1358; (*d*) A. Wilson, T. van Mourik and T. H. Dunning, *J. Mol. Struct. (THEOCHEM)*, 1997, **388**, 339.

[9] M. C. Payne, M. P. Teter, D. C. Allan, T. A. Arias and J. D. Joannopoulos, *Rev. Mod. Phys.*, 1992, **64**, 1045.

[10] H. J. Monkhorst and J. D. Pack, *Phys. Rev. B*, 1976, **13**, 5188.

[11] N. Troullier and J. L. Martins, *Phys. Rev. B*, 1991, **43**, 1993.

[12] *CPMD, Version 3.13.2, IBM Corp. 1990-2008, MPI für Festkörperforschung, Stuttgart, 1997-2001.*, 2008.

[13] D. Vanderbilt, *Phys. Rev. B*, 1990, **41**, 7892.

[14] R. M. Martin, *Electronic Structure: Basic Theory and Practical Methods*, Cambridge University Press, 2004.

[15] P. Hohenberg and W. Kohn, *Phys. Rev.*, 1964, **136**, B864.

[16] W. Kohn and L. J. Sham, *Phys. Rev.*, 1965, **140**, A1133.

[17] D. M. Ceperley and B. J. Alder, *Phys. Rev. Lett.*, 1980, **45**, 566.

[18] (*a*) A. D. Becke, *J. Chem. Phys.*, 1993, **98**, 5648; (*b*) C. Lee, W. Yang and R. G. Parr, *Phys. Rev. B*, 1992, **37**, 785; (*c*) B. Miehlich, A. Savin, H. Stoll and H. Preuss, *Chem. Phys. Lett.*, 1989, **157**, 200.

[19] N. L. Allinger and K. Chen, *J. Comput. Chem.*, 1996, **17**, 642.

[20] W. D. Cornell, P. Cieplak, C. I. Bayly, I. R. Gould, K. M. J. Merz, D. M. Ferguson, D. C. Spellmeyer, T. Fox, J. W. Caldwell and P. A. Kollman, *J. Am. Chem. Soc.*, 1995, **117**, 5179.

[21] M. P. Allen and D. J. Tildesley, *Computer Simulation of Liquids*, Oxford University Press, 1989.

[22] R. A. Buckingham, *Proc. R. Soc. Lond. A.*, 1938, **168**, 264.

[23] A. C. van Duin, S. Dasgupta and W. A. Lorant, F. Goddard III, *J. Phys. Chem. A*, 2001, **105**, 9396.

[24] R. Hoffmann, *J. Chem. Phys.*, 1963, **39**, 1397.

[25] J. A. Pople, D. P. Santry and G. A. Segal, *J. Chem. Phys.*, 1965, **43**, S129.

[26] J. A. Pople, D. L. Beveridge and P. A. Dobosh, *J. Chem. Phys.*, 1967, **47**, 2026.

[27] M. J. S. Dewar and W. Thiel, *J. Am. Chem. Soc.*, 1977, **99**, 4899.

[28] W. Thiel and A. A. Voityuk, *J. Phys. Chem.*, 1996, **100**, 616.

[29] J. J. P. Stewart, *J. Mol. Model.*, 2007, **13**, 1173.

[30] (*a*) J. J. P. Stewart, *J. Comput.Chem.*, 1989, **10**, 209; (*b*) J. J. P. Stewart, *J. Comput. Chem.*, 1989, **10**, 221.

[31] J. VandeVondele, M. Krack, F. Mohamed, M. Parrinello, T. Chassaing and J. Hutter, *Comp. Phys. Comm.*, 2005, **167**, 103.

[32] L. Verlet, *Phys. Rev.*, 1967, **159**, 98.

[33] W. G. Hoover, *Computational Statistical Mechanics*, Elsiver, 1991.

[34] H. C. Anderson, *J. Comp. Phys.*, 1983, **52**, 24.

[35] M. M. Siddick, G. J. Ackland and C. A. Morrison, *J. Chem. Phys.*, 2006, **125**, 64707.

[36] A. Nitzan, *Chemical Dynamics in Condensed Phases*, Oxford University Press, 2006.

[37] (*a*) S. Nosé, *J. Chem. Phys.*, 1984, **81**, 511; (*b*) W. G. Hoover, *Phys. Rev. A*, 1985, **31**, 1695.

[38] G. Bussi, D. Donadio and M. Parrinello, *J. Chem. Phys.*, 2007, **126**, 014101.

[39] H. C. Anderson, *J. Chem. Phys.*, 1980, **72**, 2384.

[40] R. Car and M. Parrinello, *Phys. Rev. Lett.*, 1985, **55**, 2471.

[41] T. Pilati, F. Demartin and C. M. Gramaccioli, *Phys. Chem. Minerals*, 1998, **26**, 149.

[42] R. P. Feynman and A. R. Hibbs, *Quantum mechanics and Path Integrals*, McGraw-Hill Book Company, 1965.

[43] M. E. Tuckerman, *Path Integration via Molecular Dynamics*, John von Neumann Institute for Computing, Jülich, 2002, vol. 10.

[44] D. Chandler and P. G. Wolynes, *J. Chem. Phys.*, 1981, **74**, 4078.

[45] M. Parrinello and A. Rahman, *J. Chem. Phys.*, 1984, **80**, 860.

[46] G. A. Cao, J. Voth, *J. Chem. Phys.*, 1993, **99**, 10070.

[47] I. R. Craig and D. E. Manolopoulos, *J. Chem. Phys.*, 2004, **121**, 3368.

Chapter 3

Molecular dynamics simulations of phase-I ammonia

3.1 Introduction

The molecular-dynamics simulation technique has been in use for over 40 years and has been applied to many challenging problems in all phases and types of matter. Its use in studying thermal motion from a crystallographic viewpoint has been limited to a few studies.[1–3] The present work represents the first systematic study using MD simulations. In performing such a study it is important to choose molecules that are both well suited to the methods being employed and have a variety of experimental data available for comparison with the simulated data.

The crystal structure of phase-I ammonia, NH_3, has been the focus of experimental and theoretical investigation for over 50 years. Experimentally the deuterated crystal structure has been determined by powder neutron diffraction by Reed and Harris,[4] and more recently by Hewat and Reikel.[5] X-ray diffraction has also been employed,[6] as well as diffuse neutron scattering.[7] Numerous experimental and theoretical studies have explored the phonon spectrum of phase-I ammonia using infra-red spectroscopy,[8,9] Raman spectroscopy,[8] inelastic neutron scattering,[10] DFT calculations[11] and empirical models.[12] The result is an array of information for comparison with the results of the MD simulations.

Figure 3.1: Unit-cell of phase-I ammonia (NH_3).

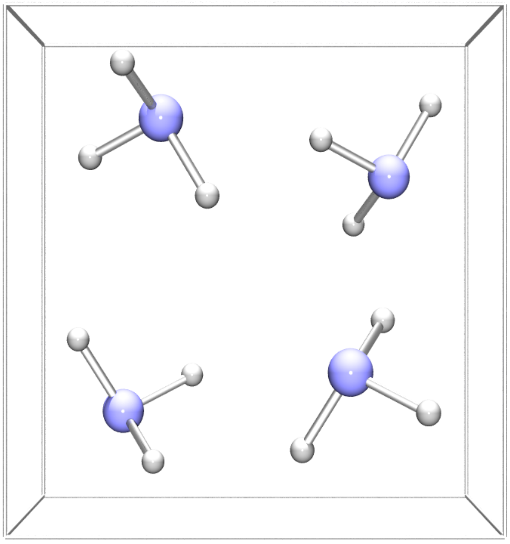

Phase-I ammonia is a cubic crystal structure in the $P2_13$ space group. There are four molecules in the unit cell as shown in Figure 3.1. With 12 symmetry operations acting on the unit cell, the asymmetric unit simplifies to just one hydrogen and one third of a nitrogen. The powder neutron study by Hewat and Reikel determined the crystal structure at 2, 77 and 180 K and applied **TLS** corrections (see Section 1.3.3) to the experimental N–D bond lengths to estimate experimental equilibrium (*i.e.* vibration free) distances. This should make ammonia an ideal test case for the molecule dynamics method of determining experimental equilibrium distances.

A combination of DFT and empirical-potential (EP) simulations have been used to apply the MD method for equilibrium structures. DFT should offer more quantitative information, while the EP simulations provide qualitative validation for the DFT-derived results.

3.2 Simulation methods

3.2.1 DFT-MD simulations

DFT-MD simulations were performed using a variety of ensembles and supercell sizes. A 1×1×1 unit cell of phase-I ND_3 was simulated using the CASTEP plane-wave (PW) DFT code.[13] ND_3 was simulated to allow direct comparison with the neutron diffraction results. The PW91 GGA-type exchange-correlation functional[14] was used for all these calculations, together with a PW cut-off energy of 400 eV. The core-valence interactions were represented by the standard ultrasoft psuedopotentials provided with the CASTEP code. The wavefunction's reciprocal space was sampled using a 2×2×2 Monkhorst-pack (MP) grid. The cut-off energy and MP grid were determined by converging the change in the total energy and atomic forces with respect to these parameters to sufficiently small values (less than 1 meV atom^{-1} and 1 meV Å^{-1}, respectively). The equilibrium geometry of the crystal structure was determined by optimisation of both the ionic positions and the lattice parameter until changes in the total energy, forces and stress tensor fell below acceptable limits (less than 5×10^{-7} eV, 1 meV Å^{-1}

and 0.02 GPa, respectively).

MD simulations of the 1×1×1 cells were carried out in both the NVE and NVT ensembles starting from the equilibrium geometry with the unit cell size fixed at the equilibrium value irrespective of the simulation temperature. The initial temperature of the simulation depended on which ensemble was used. These MD simulations were carried out using the BOMD method with wavefunction extrapolation (see Section 2.3.2). A simulation timestep of 0.8 fs was used. This timestep sampled the highest frequency stretch, νN–D, more than 15 times ensuring a stable trajectory.

Simulations were also carried out using a 2×2×2 supercell with the CPMD program.[15] For these simulations the PBE functional[16] was used together with a PW cut-off of 800 eV. The larger cut-off was required as the standard norm-conserving psuedopotentials provided with the CPMD code were used. The CPMD code did not support the use of multiple *k*-points at the time these simulations were performed. However, as the use of the supercell allows the electronic wavefunction to sample more *k*-points than just the Γ-point. The geometry was re-optimised but the unit-cell size was fixed, as the CPMD program does not have robust cell optimisation methods. MD simulations were carried out at a number of temperatures in the NVT ensemble. The Car-Parinello method[17] (Section 2.3.2) was used to perform the dynamics, necessitating a much smaller timestep of 0.09 fs.

Calculations were performed using the computational resources of the EPRSC National Service for Computational Chemistry (http://www.nsccs.ac.uk) and the Edinburgh Parallel Computing Centre (http://www.epcc.ed.ac.uk).

3.2.2 EP-MD simulations

To complement the DFT-MD simulations classical and path-integral (PI) empirical-potential MD simulations of ND_3 were carried out using a force field previously detailed in the literature by Hinchliffe *et al.*[12] Hinchliffe's Model C (abbreviated to HC) comprises an electrostatic component, with a charge

(0.462 e) on each H/D atom and a charge (-1.386 e) on a site suspended below the N atom (towards the plane of the hydrogens). The non-electrostatic intermolecular interactions are split into dispersive components (only between N atoms), repulsive interactions between all atoms and a mildly attractive interaction between N and H atoms. This force field was developed for rigid-body simulations so the harmonic bond stretches and angle bends suggested by Diraison *et al.*[18] were used to model intra-molecular degrees of freedom.

The HC model was implemented in an "in-house" PIMD code developed by Mr. T. Markland and Dr. S. Habershon, both of the University of Oxford. To ensure ergodicity during the classical and PI simulations an Anderson thermostat[19] was applied. It was evident from initial simulations that the experimental cell parameter for ammonia was unsuitable for simulations with these models. The finite-T cell vectors for 77 K and 180 K were determined by performing an NVT simulation using a 4×4×4 supercell with random attempts at Monte-Carlo NPT[20] changes in cell size. All calculations were performed on the Hare cluster of the EaStCHEM Research Computing Facility (http://www.eastchem.ac.uk/rcf). This facility is partially supported by the eDIKT initiative (http://www.edikt.org.uk).

3.2.3 Trajectory analysis

The trajectories that resulted from the MD simulations were analysed in a variety of ways. For analysis of crystallographic parameters the space-group symmetry may be exploited to increase the number of data points. In ammonia all of the H/D atoms and all of the N atoms are equivalent to each other. Application of the inverse symmetry operations maps each atom in the supercell into the asymmetric unit. When in the asymmetric unit the coordinates adopted by the symmetry related atoms can be used to calculate the mean and variance of each asymmetric atomic position. For the asymmetric nitrogen, the three positional coordinates are equivalent and were averaged accordingly. The mean Cartesian position of an atom, $\bar{\mathbf{u}}$, can be calculated from the mean components of the position vector:

$$\bar{\mathbf{u}} = (\bar{u_1}, \bar{u_2}, \bar{u_3}), \tag{3.1}$$

$$\bar{u_i} = \frac{1}{N}\sum_{n=1}^{N} u_{i,n}, \tag{3.2}$$

where N is the total number of steps the average is calculated over and $u_{i,n}$ is the value of u_i at step number n. It is routine to discard the first few picoseconds of a trajectory to allow for the MD simulation equilibrating. Time-averages over the equilibrated trajectory will be denoted using angle brackets, *e.g.* $\langle u_i \rangle$. The variances, σ^2_{ii}, and covariances, σ^2_{ij}, of an atomic position are given by:

$$\sigma^2_{ij} = \langle (u_i - \bar{u_i})(u_j - \bar{u_j}) \rangle = \langle \Delta u_i \Delta u_j \rangle. \tag{3.3}$$

The numerical evaluation of the mean and variances yields the true anharmonic mean and variance as we are effectively using a numerical probability density function (PDF) for discrete evaluation of Equation 1.15. The Gaussian approximation used in crystallography (Section 1.3.1) determines harmonic mean and variance values. If the true probability distribution is not harmonic then it is possible for the harmonic and MD/anharmonic values to differ. There has been no systematic study of how much the potential difference might be but Scheringer has shown various differences of 0.0004 – 0.0052 Å for bonded distances of thiopyridone when calculated with harmonic and anharmonic means.[21] However, it is likely that the numerical variances will provide a reasonable approximation to the experimental anisotropic displacement parameters (ADPs):

$$\sigma^2_{ij} \approx U_{ij}. \tag{3.4}$$

There is no direct uncertainty associated with a static, theoretically calculated geometry, although there will be some errors due to convergence of the various calculation parameters such as the cut-off energy *etc.* However, there is a sampling uncertainty associated with averages calculated from an MD simulation. The uncertainty or standard error in the mean value of random variable, x, is given by the Central Limit Theorem:[20]

$$\sigma_{\bar{x}} = \frac{\sigma_x}{\sqrt{N-1}}, \tag{3.5}$$

where N is the number of *random* samples taken of the value x and σ_x is the standard deviation of x. The standard error in the variance of x is given by:[22]

$$\sigma_{\sigma_x^2} = \sqrt{\frac{2}{N-1}}\sigma_x^2. \tag{3.6}$$

$$\sigma_{\sigma_x} = \frac{\sigma_x}{\sqrt{2(N-1)}}. \tag{3.7}$$

The uncertainty in a covariance can be estimated by noting that

$$U_{ij} = \rho_{ij}\sigma_i\sigma_j, \tag{3.8}$$

where ρ_{ij} is the correlation coefficient of the i^{th} and j^{th} variable. Propagation of the errors in σ_i and σ_j leads to the following expression for the uncertainty in a covariance:

$$\sigma_{U_{ij}} = \sqrt{\frac{1+\rho_{ij}}{N-1}}\rho_{ij}\sigma_i\sigma_j. \tag{3.9}$$

As U_{ii} is given by $\rho_{ii}\sigma_i\sigma_i$ and $\rho_{ii} = 1$, Equation 3.9 reduces to Equation 3.6 for $i = j$. The derivation of Equation 3.9 neglects the error in the correlation coefficient. To ensure the standard error is not artificially smaller as a result of this, a value of $\rho_{ij} = 1$ is used in all calculations to give an upper limit to the uncertainty. The uncertainty in a bond length has been calculated by propagation of the uncertainties in the positions of the two atoms in question.

An MD simulation does not randomly sample a quantity. A smooth and stable trajectory requires correlations between values in different steps. The result of this is that the preceding equations underestimate the standard errors in the mean and variance. This can be overcome by including only every n^{th} step in analysis of the data. Alternatively the correlation can be removed using a blocking procedure in which adjacent data points are iteratively averaged so that $N' = N/2$.[22] Averaging of correlated data points will not change the mean but it will increase the variance, whilst N' decreases, resulting in the standard error of the mean rising until the correlation is removed or blocked out. A drawback of the blocking method is the uncertainty in the standard error itself:

$$\sigma_{\bar{x}}^2 = \frac{\sigma_x^2}{N-1} \pm \sqrt{\frac{2}{N-1}}\frac{\sigma_x^2}{N-1}. \tag{3.10}$$

$$\sigma_{\bar{x}} = \sqrt{\frac{\sigma_x^2}{N-1}} \pm \left(\frac{1}{\sqrt{2(N-1)}} \times \sqrt{\frac{\sigma_x^2}{N-1}}\right). \tag{3.11}$$

The result is that for a completely blocked dataset (with $N' = 2$) the uncertainty in the standard error is the error itself divided by $\sqrt{2}$. Typically the largest value of $\sigma_{\bar{x}}$ obtained with the blocking method is taken as a reasonable estimate of the uncertainty. The uncorrelated uncertainty in the variance must be estimated from the ratio between the correlated and uncorrelated mean. In general this ratio will be same for the mean and the variance.[20] In general, the uncorrelated uncertainties in the simulations of ND_3 are an order of magnitude larger than the correlated values.

As well as determining the standard mean and ADPs for comparison with experiment, the MD simulation can be used to determine the numerical PDF. The positions adopted by an atom in the course of the simulation can be binned to form 1–, 2– or 3–dimensional histograms. These numerical PDF's can then be fitted to analytical functions (such as those presented in Chapter 1). Code has been written to post-analyse MD trajectories from a variety of DFT and classical MD programs, providing the multi-dimensional histograms as well as the "blocked" mean and variances of each asymmetric atomic position. Analysis of the classical and PIMD simulations for ND_3 was performed "on the fly" because of the large volume of data produced. As a result the blocking method could not be applied to these simulations. Instead only every 5th step was included in the analysis of the trajectories. The resulting uncertainties are so small that a uncertainty of ±1 is assumed in the last reported digit.

The equilibrium experimental structure is determined by using the differences between the theoretical equilibrium and time-averaged structures as correction to the experimental time-averaged structure. The correction vectors are defined relative to the crystallographic system, so care must be taken in applying corrections where the experimental and theoretical molecular orientations are different. Overlapping the experimental and theoretical principal axes systems should overcome this problem. As the initial study on ammonia is focused on benchmarking the MD method this procedure has not been applied here; instead the theoretical distance corrections are reported for comparison with the **TLS** corrections of Hewat and Reikel. Analysis of differences between the anharmonic and harmonic mean positions and fitting of the numerical distributions will be described in Chapter 5.

3.3 Results and Discussion

3.3.1 Equilibrium geometry

The equilibrium geometry of ammonia as determined using the two supercell sizes and DFT functionals is given in Table 3.1. The agreement of the theoretical values with the experimental ones of Hewat and Reikel is reasonable. The calculated N–H bond length is 0.02 Å larger than the experimental value. This is most likely a result of the tendency of GGA functionals to over-estimate bond lengths. At 2 K we expect only very small thermal motion effects. The theoretical equilibrium cell vector is 2.6% bigger than the 2 K experimental value.

3.3.2 Thermostatting and ergodicity

In studying ammonia the principal aim was to use it as a system to benchmark various theoretical methods and analysis techniques from the crystallographic viewpoint. NPT simulations should reproduce the experimental conditions the best. However, such simulations often require a large PW cut-off energy (1.5–2 times that of an NVT simulation) to converge the stress tensor and plane-wave

Table 3.1: Equilibrium atomic positions (fraction coordinates), interatomic distances and angles and the optimised lattice constant, a, for ammonia determined using PW-DFT, together with experimental[5] values at 2 K.

	1×1×1[a]	2×2×2[b]	Experiment
D_x	0.3460	0.3471	0.3750(3)
D_y	0.2714	0.2711	0.2712(4)
D_z	0.0910	0.0932	0.1129(3)
N_x	0.1935	0.1925	0.2109(3)
r(N–D)/ Å	1.0347	1.0361	1.012(2)[c]
r(N···D) / Å	2.3354	2.3319	2.357(2)
∠(D–N–D) / °	107.12	106.01	107.5(2)
a / Å	5.1846	5.1846[d]	5.048

[a] CASTEP; PW91/USPP; 400eV cut-off.
[b] CPMD; PBE/NCPP; 800eV cut-off.
[c] Uncorrected for librational effects.
[d] Fixed at CASTEP unit-cell value.

grids adequately.[23] A drawback of not performing NPT simulations is that the pressure of the system may deviate from the experimental conditions we wish to compare with. In particular, using the optimised cell geometry will lead to pressures larger than 1 bar. For small systems (such as 1×1×1 and 2×2×2 cells of ammonia) the pressure can be poorly defined and oscillate substantially so attempts at barostatting will be futile unless very long simulations are performed to allow the cell parameters and other quantities to converge properly. As a result initial simulations focused on 1×1×1 unit-cell simulations of ND_3 in the NVE and NVT ensembles. It is important to note that simulations of a unit cell will neglect lattice vibrations with periods longer than unit cells. The positional parameters and ADPs determined from such simulations include only the contributions of Γ-point or zone-centred phonons.

NVE simulations conserve the total energy of the system. However, when equilibrated an NVE simulation will have an average kinetic energy and hence an average temperature. For a harmonic system an initial kinetic energy will be equi-partitioned between the kinetic and potential energies of the system.[24] If we start the simulation from an equilibrium geometry with a temperature T then the system should converge to an average temperature of $T/2$.

Thermostatting to reproduce the NVT ensemble would help ensure ergodicity.

However, dynamic information could then be lost or distorted. While the main interest is the static distribution of atomic positions it is prudent to try and maximise the information these potentially expensive MD simulations can produce. Therefore, initial simulations applied no thermostat. Attempts to simulate the crystal structure at 180 K failed. Performing this simulation required an initial temperature of 360 K, far in excess of the melting point of ammonia ($\approx$ 195 K). This large initial kinetic energy lead to significant deviations from the initial starting point. Some form of thermostatted equilibration might permit such a simulation but this was not possible with the CASTEP program.

Experimental data at 77 K also exists so three NVE simulations were performed with an initial temperature of 155 K. The average temperatures and positions are given in Table 3.2. The temperatures of the simulations are reasonably close to the desired temperature of 77 K. However, there are clear differences between the theoretical averages and distance corrections from the three simulations. Simulations 1 and 2 agree reasonably but simulation 3 suggests a smaller distance correction. While the theoretical results are within 3 to 4 σ of each other, it must be remembered that the blocking method provides *worst case* estimates of the errors. Repeating the simulations a number of times gives us a better idea of the uncertainties, although three simulations is sufficient only for qualitative observations. Encouragingly, the uncertainties themselves are smaller than the experimental uncertainties. The experimental (**TLS**) distance correction of 0.051 Å is much much larger than the mean correction of 0.0067 Å obtained from theory. The disagreement between the simulations and experiment is more evident from the variances or ADPs, which are given in Table 3.3. There are large and statistically significant differences between the theoretical variances. The experimental ADPs are much larger than the theoretical ones and the larger experimental distance correction makes sense in terms of the larger experimental ADPs. It is clear that the NVE simulations do not provide reproducible results. Small differences between runs is acceptable and expected but the differences in the ADPs are large and should disappear with some form of thermostatting.

A further three MD simulations were performed in the NVT ensemble with a

Table 3.2: The length, average temperature, standard deviation of the temperature, fractional coordinates, N–D bond length and difference in theoretical equilibrium and time-averaged length for each of the three ND_3 NVE runs together with the experimental neutron diffraction positions at 77 K.[5]

	Run 1	Run 2	Run 3	Experimental
Simulation length /ps^a	30	37	35	–
$\langle T \rangle$ / K	73.5	80.1	77.4	77
σ_T / K	11.2	12.3	12.3	–
$\langle \mathrm{D}_x \rangle$	0.3520(3)	0.3525(4)	0.3515(1)	0.3694(6)
$\langle \mathrm{D}_y \rangle$	0.2697(1)	0.2696(2)	0.2699(1)	0.2694(6)
$\langle \mathrm{D}_z \rangle$	0.0965(2)	0.0971(4)	0.0957(2)	0.1141(11)
$\langle \mathrm{N}_x \rangle$	0.1975(5)	0.1977(7)	0.1969(3)	0.2108(11)
$r(\mathrm{N–D})_{\mathrm{av}}$ / Å	1.0270(28)	1.0272(39)	1.0301(17)	0.988(9)
$\Delta r(\mathrm{N–D})^b$/ Å	0.0077(28)	0.0075(39)	0.0047(17)	0.051(22)^c

^{a} 1 ps = 10^{-12} s
^{b} $\Delta r = r_\mathrm{e} - r_\mathrm{a}$
^{c} **TLS** distance correction.

Table 3.3: Γ-point thermal ADPs of the N and D atoms of the asymmetric unit of ND_3 extracted from the three 77 K NVE-MD simulations, together with experimental values of Hewat and Reikel.[5]

ADP / Å^2	Run 1	Run 2	Run 3	Experiment
N				
U_{ii}	0.0047(3)	0.0059(4)	0.0033(1)	0.0290(22)
U_{ij}	−0.0010(1)	−0.0011(2)	−0.0008(1)	−0.0015(15)
D				
U_{11}	0.0091(2)	0.0120(2)	0.0068(1)	0.0467(36)
U_{22}	0.0076(2)	0.0079(2)	0.0062(1)	0.0407(38)
U_{33}	0.0097(2)	0.0117(2)	0.0071(1)	0.0552(30)
U_{12}	−0.0027(1)	−0.0032(1)	−0.0024(1)	−0.0096(21)
U_{13}	0.0026(1)	0.0041(1)	0.0020(1)	0.0091(34)
U_{23}	−0.0005(1)	−0.0009(1)	−0.0005(1)	−0.0027(24)

Nosé-Hoover (NH) thermostat.[25] It has been shown that a single NH thermostat does not ensure ergodicity so a chain of five thermostats was used.[26] Chaining the thermostats, so that the temperature of each "heat bath" is controlled by another promotes ergodicity as it randomises the thermostat's effect. The resulting average temperatures and positions are given in Table 3.4, while the ADPs are given in Table 3.5. The temperature is now much closer to the desired temperature of 77 K. Unfortunately, the agreement between the time-averaged positions is no better than for the NVE simulations. The ADPs are also still different by a significant amount. The value of U_{11} for the D atom during each simulation is shown in Figure 3.2. The oscillations in the value are not large and to some extent all three simulations look as if they are reasonable converged, even though the final values are very different. Larger systems, in terms of both supercell and molecule size should yield better results. However, it is evident that strong thermostatting is required for the the present system to achieve meaningful results.

Table 3.4: The length, average temperature, standard deviation of the temperature, fractional coordinates, bond length and difference in theoretical equilibrium and time-averaged lengths for each of the three ND_3 NVT runs.

	Run 1	Run 2	Run 3
Simulation length /ps	50	33	35
$\langle T \rangle$ / K	77.0	76.9	76.9
σ_T / K	16.1	16.2	16.3
$\langle \mathrm{D}_x \rangle$	0.3519(3)	0.3517(2)	0.3525(5)
$\langle \mathrm{D}_y \rangle$	0.2699(1)	0.2701(2)	0.2696(3)
$\langle \mathrm{D}_z \rangle$	0.0968(2)	0.0963(3)	0.0974(2)
$\langle \mathrm{N}_x \rangle$	0.1974(4)	0.1973(3)	0.1978(3)
$r(\mathrm{N–D})_{\mathrm{av}}$ / Å	1.0271(22)	1.0283(20)	1.0261(27)
$\Delta r(\mathrm{N–D})^a$/ Å	0.0076(22)	0.0063(20)	0.0086(27)

^{a} $\Delta r = r_{\mathrm{e}} - r_{\mathrm{a}}$

Table 3.5: Γ-point thermal ADPs of the N and D atoms of the asymmetric unit of ND_3 extracted from the three 77 K NVT-MD simulations.

ADP / Å^2	Run 1	Run 2	Run 3
N			
U_{ii}	0.0050(3)	0.0044(3)	0.0061(1)
U_{ij}	−0.0003(1)	−0.0007(2)	−0.0007(1)
D			
U_{11}	0.0102(2)	0.0078(2)	0.0126(1)
U_{22}	0.0086(2)	0.0083(2)	0.0089(1)
U_{33}	0.0103(2)	0.0089(2)	0.0126(1)
U_{12}	−0.0028(1)	−0.0024(1)	−0.0035(1)
U_{13}	0.0038(1)	0.0022(1)	0.0044(1)
U_{23}	−0.0003(1)	0.0000(1)	−0.0007(1)

The CASTEP code implements the Langevin dynamics method,[20,27] which adds a friction term to the momenta of the particles in the system. This friction term represents interactions of the particles with a solvent or gas, which can be used to control the temperature of the system in a similar manner to the Anderson thermostat, which effectively models collisions of gas-phase particles with the

Figure 3.2: Cumulative value of the D atom U_{11} displacement parameter during the course of the three NH NVT-MD simulations at 77 K.

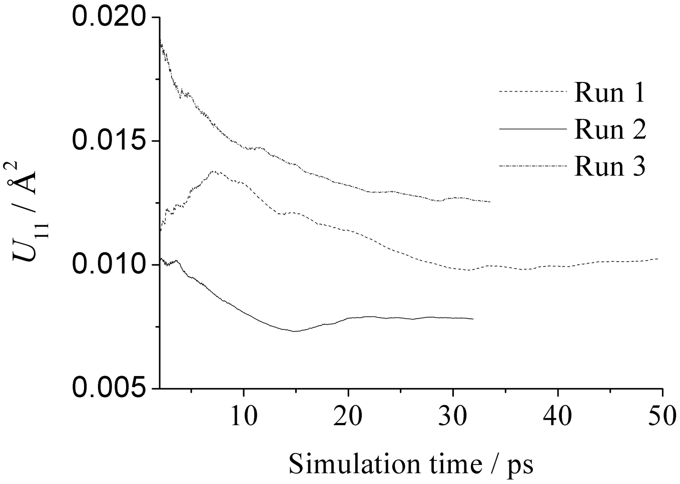

system. Two Langevin dynamics simulations were performed in unit cells of ND_3 at 77 K. A relaxation time equivalent to 100 MD steps was used. The resulting mean positions and ADPs are given in Tables 3.6 and 3.7. The effect of the Langevin thermostat on the time-averaged parameters is dramatic, with all of the time-averaged parameters now within 2–3 σ of each other. It is likely that small differences will always arise between simulations unless they are run for a computationally excessive amount of time. The results of Tables 3.6 and 3.7 may represent the best precision attainable for such a system. The disagreement between the unit-cell ADPs and the experimental values remains.

3.3.3 Supercell size and quantum effects

There are a number of potential sources for the disagreement between the theoretical and experimental ADPs. The simulation pressure might play an important role. Fixing the cell vector at its optimised value generates an average pressure of 0.1 GPa during the 77 K simulation. This will restrict the thermal motion in the system. The reduction in thermal motion between experiment and theory would suggest that a pressure of 0.1 GPa has a substantial effect on the potential energy surface. This seems unlikely as the structure of Phase-I ammonia

Table 3.6: The length, average temperature, standard deviation of the temperature, fractional coordinates, bond distances and difference in theoretical equilibrium and time-averaged positions for both of the ND_3 Langevin NVT runs.

	Run 1	Run 2
Simulation length /ps	50	34
$\langle T \rangle$ / K	76.4	76.9
σ_T / K	16.4	16.3
$\langle \mathrm{D}_x \rangle$	0.3522(3)	0.3518(5)
$\langle \mathrm{D}_y \rangle$	0.2698(1)	0.2701(1)
$\langle \mathrm{D}_z \rangle$	0.0968(2)	0.0966(3)
$\langle \mathrm{N}_x \rangle$	0.1975(4)	0.1974(7)
$r(\mathrm{N–D})_{\mathrm{av}}$ / Å	1.0279(22)	1.0270(42)
$\Delta r(\mathrm{N–D})^a$/ Å	0.0068(22)	0.0077(42)

[a] $\Delta r = r_{\mathrm{e}} - r_{\mathrm{a}}$

Table 3.7: Γ-point thermal ADPs of the N and D atoms of the asymmetric unit of ND_3 extracted from the two 77 K Langevin NVT-MD simulations.

ADP / Å^2	Run 1	Run 2
N		
U_{ii}	0.0046(1)	0.0048(4)
U_{ij}	−0.0006(1)	−0.0006(1)
D		
U_{11}	0.0089(1)	0.0092(2)
U_{22}	0.0084(1)	0.0084(2)
U_{33}	0.0095(2)	0.0098(2)
U_{12}	−0.0028(1)	−0.0027(1)
U_{13}	0.0028(1)	0.0029(1)
U_{23}	−0.0003(1)	−0.0002(1)

is stable up to 1.4 GPa[11] and the vibration frequencies are changed by less than 5 cm^{-1} over this pressure range.[28] While pressure may play a role a more likely explanation is offered by the use of only a unit cell. As detailed above, simulations of a unit cell restrict the types of lattice vibrations that occur in the system to having periods of a single unit cell. Thus non-Γ-point phonon modes are neglected by the calculations presented in the previous section. Of particular importance will be the low-frequency large-amplitude acoustic phonons that appear away from the Γ-point. At the Γ-point these modes correspond to the translational degrees of freedom of the crystal. To partly address their omission a DFT simulation of a 2×2×2 supercell of ND_3 was performed using the CPMD code.

The CPMD code, however, only supports the use of Nosé–Hoover thermostats, which were shown earlier to perform poorly. To encourage ergodicity a "massive" NH thermostat was used.[29] The resulting ADPs and bonded distance correction from a 15 ps simulation are given in Table 3.8. The agreement between theory and experiment is somewhat better with the ADPs being 50–100% larger than those of the single unit-cell simulations. The distance correction is only slightly larger than that for the Langevin dynamics simulations (~ 0.0071 Å). This in not unexpected as the acoustic modes have predominantly translational character; they have a significant impact on atomic displacements but little effect on intramolecular distances. Other non-Γ-point librational modes will have similar types of motion to those already present at the Γ-point.

Table 3.8: ADPs (in Å^2) of the N and D atoms of the asymmetric unit of ND_3 together with the time-averaged bonded distance and distance correction extracted from the 77 K 2×2×2 supercell NVT-MD simulation. Experimental values of Hewat and Reikel[5] are provided for comparison.

ADP / Å^2	DFT-MD	Experiment
N		
U_{ii}	0.0103(6)	0.0290(22)
U_{ij}	−0.0010(1)	−0.0015(15)
D		
U_{11}	0.0147(4)	0.0467(36)
U_{22}	0.0155(2)	0.0407(38)
U_{33}	0.0163(3)	0.0552(30)
U_{12}	−0.0038(1)	−0.0096(21)
U_{13}	0.0025(1)	0.0091(34)
U_{23}	−0.0004(1)	−0.0027(24)
$r(\text{N–D})_{\text{av}}$ / Å	1.0281(36)	0.988(9)
$\Delta r(\text{N–D})^a$/ Å	0.0083(36)	0.051(22)^b

^{a} $\Delta r = r_e - r_a$

^{b} **TLS** distance correction.

Another likely source of disagreement is the application of classical Newtonian mechanics for simulations at such a low temperature (77 K). The neglect of quantum effects could lead to significant underestimation of the ADPs. Performing a DFT-PIMD simulation would be very computationally intensive. However, a NVT simulation of the structure at the higher temperature of 180 K can be performed as the initial temperature will not be as high as in the NVE case. Agreement between theory and experiment at the higher temperature should be better if quantum effects play a role. A 15 ps simulation of a 2×2×2 supercell was performed at 180 K in the same manner as for the 77 K simulation. The resulting ADPs and bonded distance correction are presented in Table 3.9. The results show a large increase in both the ADPs and the distance corrections. While the agreement between the ADPs is somewhat better, substantial differences remain.

Table 3.9: ADPs (in Å^2) of the N and D atoms of the asymmetric unit of ND_3 together with the time-averaged bonded distance and distance correction extracted from the 180 K 2×2×2 supercell NVT-MD simulation. Experimental values of Hewat and Reikel[5] are provided for comparison.

ADP / Å^2	DFT-MD	Experiment
N		
U_{ii}	0.0176(4)	0.0384(8)
U_{ij}	−0.0013(2)	−0.0014(5)
D		
U_{11}	0.0260(3)	0.0575(16)
U_{22}	0.0272(3)	0.0709(22)
U_{33}	0.0287(3)	0.0676(23)
U_{12}	−0.0066(1)	−0.0186(11)
U_{13}	0.0051(1)	0.0093(14)
U_{23}	−0.0005(1)	−0.0029(14)
r(N–D)$_{\text{av}}$ / Å	1.0213(36)	0.989(5)
Δr(N–D)^a/ Å	0.0152(31)	0.069(9)^b

^{a} $\Delta r = r_{\text{e}} - r_{\text{a}}$

^{b} **TLS** distance correction.

Figure 3.3 shows the theoretical thermal ellipsoids of the ammonia molecule. The plotted thermal ellipsoids seem reasonable in size and orientation. The experimental ellipsoids are much larger and at larger probability contours, greater than 90%, they begin to overlap. The **TLS** distance corrections are also very large and suggest a much longer equilibrium distance (1.058 Å as determined at 180 K) than the DFT calculations using the PBE and PW91 functional. This value is also much longer than the time-averaged interatomic N–D distance of 1.005(1) Å determined by diffuse scattering.[7] MD simulations will determine thermal ADPs, that is ADPs that result from thermal motion. Disorder in a crystal structure and errors in data analysis can contribute to ADPs and may explain the discrepancies encountered here.

Leclercq *et al.*[30] re-refined the original dataset of Hewat and Reikel using a curvilinear structure factor. This structure factor treated the D atoms as rotating

Figure 3.3: Calculated crystal structure of ND_3 at 180 K. (Ellipsoids plotted at 50% probability level.)

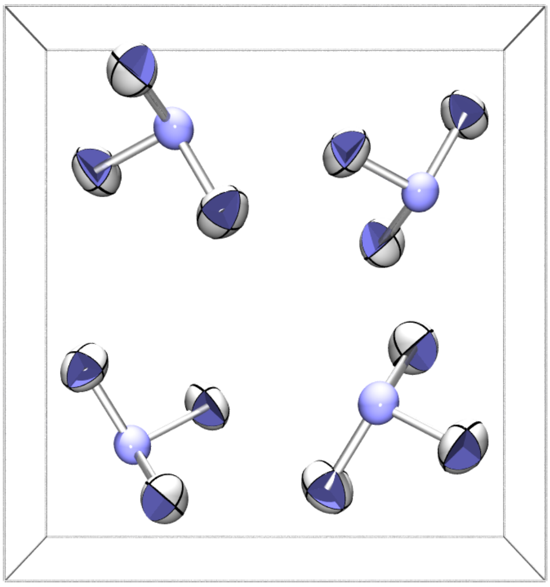

around the C_3 axis of the ammonia molecule and was defined in an internal coordinate system of the molecule. As a result the refinement using this structure factor yielded distances free from the effects of librational motion. Isotropic estimates of the amount of thermal motion of the D atoms were also obtained. Table 3.10 gives the U_{eq} values as determined at 77 K and 180 K from the 2×2×2 supercell DFT-MD simulations and the two experimental refinements. At 77 K there is much closer agreement between the MD values and those of Leclercq *et al.* At the higher temperature the results are within 3 σ for the N atom and within 6 σ for the D atom. This shows that the original refinement of Hewat and Reikel was most likely flawed. The discrepancy in the values at 77 K is likely the results of neglecting quantum mechanics in the motions of the atoms. Leclercq determined an equilibrium distance of 1.001(7) Å. Applying the MD distance correction of 0.0152 Å at 180 K to the time-averaged distance of Hewat and Reikel yields an r_{e} value of 1.004(6) Å. The agreement is encouraging but to determine the equilibrium structure correctly a more reliable experimental time-averaged geometry must be determined. The geometry determined by Leclercq *et al.* neglects internal vibrations of the molecule, which may also affect the atomic positions and interatomic distances.

The theoretical equilibrium bond length in the gas phase is 1.0107 Å, determined using the coupled cluster method and extrapolation of large basis-set results, while the empirical experimental equilibrium value (calculated using experimental microwave spectroscopic results and theoretical vibrational corrections) is 1.01139(60) Å.[31] With solid-state H-bonding the N–D/H equilibrium bond length would be expected to be longer than the gas-phase value but the solid-state values from diffuse scattering and the present work are both shorter than the gas-phase values, although they are within the estimated uncertainties. More precise solid-state structural studies would confirm whether this observation has any physical significance.

Table 3.10: Isotropic displacement parameters (U_{eq}) of the N and D atoms in ND_3 from DFT-MD simulations and refinements by Leclercq *et al.*[30] and Hewat and Reikel.[5]

	N – U_{eq} / Å^2	D – U_{eq} / Å^2
77 K DFT-MD	0.0103(6)	0.0155(3)
77 K Leclercq *et al.*	0.0144(3)	0.0222(4)
77 K Hewat and Reikel	0.0290(22)	0.0475(40)
180 K DFT-MD	0.0176(4)	0.0273(3)
180 K Leclercq *et al.*	0.0166(4)	0.0243(5)
180 K Hewat and Reikel	0.0384(8)	0.0653(24)

3.3.4 Empirical potential simulations

Further validation of the DFT results presented in the preceding section would require PIMD simulations or the use of larger supercells. Simulations with a small number of path-integral beads are feasible, as might be simulations with a 3×3×3 supercell. However, converging these results would require a number of beads and supercell size that is not possible with DFT-MD simulations. To probe the importance of these factors we can turn to empirical-potential simulations. While the accuracy of these simulations may not be as good as that for DFT, they should provide a useful qualitative picture of the dynamics of ammonia.

The optimised cell parameter was determined from a number of MC-NPT runs using different initial cell sizes. A 4×4×4 supercell was used because a cell of this size should give a sufficiently converged value. At 77 K a value of ∼ 4.82 Å was found, while at 180 K the lattice constant was ∼ 4.89 Å. Table 3.11 gives the isotropic displacement parameter for the N and D atoms determined for a variety of supercell sizes using a 30 ps NVT simulation. The results are discouraging as they suggest quite large super-cells are required to converge the displacement parameters properly. However, an important parameter in empirical simulations is the cut-off distance, r_{cut}, after which intermolecular dispersion interactions are neglected. The Ewald summation method ensures that electrostatic interactions take into account the long-range order of the lattice. However, to avoid particles interacting with their periodic images the cut-off must be less than the lattice constant. Thus in empirical MD simulations a large cell can be required for an atom to interact with enough particles to behave as if it was in the solid state. In a DFT simulation the periodicity of the wavefunctions ensures that this problem does not arise; the importance of supercells in DFT simulations is to allow flexibility in thermal motions and avoid self-interactions for small systems. The poor convergence of the displacement parameters with the smaller cells may be the result of a small value of r_{cut}. Previous liquid-phase simulations of ammonia,[18] using the same electrostatic model as the HC model and a LJ potential proposed by Impey and Klein,[32] suggested that there was no significant finite-size effect with a 32-molecule system, which is equivalent to a 2×2×2 supercell. It is evident from Table 3.11 that for solid-state simulations using empirical potentials at least a 4×4×4 supercell is required to have meaningful results.

Table 3.11: Isotropic displacement parameters (U_{eq}) of the N and D atoms in ND_3 from 77 K NVT simulations with a variety of supercell sizes.

	$N_{U_{\mathrm{eq}}}$ / Å^2	$D_{U_{\mathrm{eq}}}$ / Å^2	r_{cut} / Å
2×2×2	0.00584(1)	0.01355(1)	4.82
3×3×3	0.00678(1)	0.01437(1)	7.23
4×4×4	0.00741(1)	0.01519(1)	9.64
6×6×6	0.00789(1)	0.01559(1)	14.46

The effect of pressure on the system can also be studied using the EP simulations. Calculations were performed with a 4×4×4 cell of ND_3 with the 77 K ambient pressure cell vector (4.82 Å) and two different cell vectors to explore how the displacement parameters change with pressure. The results are given in Table 3.12. The pressure has been calculated using the standard virial estimator.[20,33] The ambient pressure of 0.05 GPa is quite large but illustrates the problem of converging the cell vector with respect to pressure. This is partially a result of the bonding Morse potential's large contributions to the virial. Changing the cell length by only 0.07 Å results in substantial changes in the pressure. Encouragingly, going from nearly 0 GPa to 0.63 GPa only leads to changes of the order of 15% in the thermal parameters. As the pressure in the DFT simulations is much smaller at 0.1 GPa it is therefore likely that pressure will not play a significant role in the DFT results.

Table 3.12: Isotropic displacement parameters (U_{eq}) of the N and D atoms in ND_3 from 4×4×4 77 K NVT simulations with different lattice constants.

a / Å	$\mathrm{N}_{U_{\mathrm{eq}}}$ / Å^2	$\mathrm{D}_{U_{\mathrm{eq}}}$ / Å^2	$\langle P \rangle$ / GPa
4.75	0.00624(1)	0.01363(1)	0.63
4.82	0.00741(1)	0.01519(1)	0.05
4.89	0.00891(1)	0.01699(1)	−0.35

PIMD simulations were performed at 77 K and 180 K to compare with classical-MD trajectories. Again the simulations were carried out using a 4×4×4 supercell. The results are given in Table 3.13. The displacement parameters are 180 K are much larger than those determined by the DFT simulations but it is not surprising that the potential over-estimates thermal motion as it was optimised for the liquid phase. The U_{eq} values are still smaller than those of Hewat and Reikel. Comparison of the 1 and 32 bead simulations shows that quantum effects could easily explain the majority of the disagreement between the DFT values and those of Leclercq *et al.* at 77 K. A 64 bead simulation shows that a 32 bead simulation is sufficient for modelling ammonia at 77 K and higher temperatures. Better agreement between the EP and DFT results could be obtained using a more sophisticated potential. Janerio-Barral *et al.* have recently updated the HC model to include polarisible charges and intermolecular parameters fitted to more modern quantum-chemical calculations.[34]

Table 3.13: Isotropic displacement parameters (U_{eq}) of the N and D atoms in ND_3 from 4×4×4 simulations at 77 K and 180 K with different Trotter dimensions, P.

P	T / K	$\mathrm{N}_{U_{\mathrm{eq}}}$ / Å^2	$\mathrm{D}_{U_{\mathrm{eq}}}$ / Å^2
1	77	0.00741(1)	0.01519(1)
32	77	0.00979(1)	0.02649(1)
64	77	0.00966(1)	0.02666(1)
1	180	0.02196(1)	0.04565(1)
32	180	0.02284(1)	0.05358(1)

A final validation of the DFT-MD simulations was carried out by comparison of the NVE DFT-MD vibrational frequencies, determined from the Fourier-transform of the velocity autocorrelation function,[20] for NH_3 and ND_3 with experimental phonon and vibron data. Approximate eigenvectors were also determined from the MD trajectories. Full details of the analysis and results are provided elsewhere.[35] The DFT-MD frequencies or eigenvalues agree well with experimental and hybrid-DFT lattice dynamics (LD) results. However, the MD and LD eigenvectors suggested a number of changes in the assignments of the experimental symmetry assignments, which resolve the conflicting experimental reports of the phonon spectrum of phase I ammonia. This provides further justification for the use of DFT-MD simulations in studying ammonia.

3.3.5 Vibrational probability density functions

The numerical PDFs determined from the MD trajectories can be visualised and analysed in a variety of ways. The harmonic information is easy depicted using the normal thermal ellipsoid approach as in Figure 3.3. Information about anharmonicity can be viewed using 1-, 2- or 3-D histograms. The 2–D histograms of the D atom at 180 K are given in Figure 3.4. It is relatively easy to orientate the numerical PDF along the harmonic principal axes of thermal motion. In the case of the D atom the resulting PDFs do not appear to deviate that much from a Gaussian distribution. There is a significant amount of high-frequency noise that distorts the distributions. This noise may be removed using low-pass Fourier filters to aid visualisation. Difference maps of the numerical PDF minus an equivalent harmonic PDF can be used to illustrate anharmonicity that is not readily visible in the anharmonic distribution. The analysis and visualisation of numerical PDFs will be detailed more in Chapter 5.

Figure 3.4: 2–D vibrational probability distributions of the D atom in ND_3 at 180 K plotted along the three harmonic principal axes. (x is the longest axis; z the shortest.)

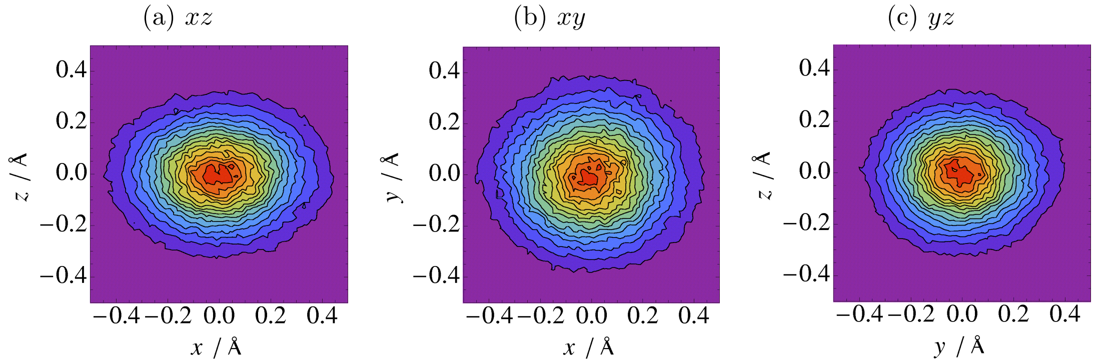
(a) xz (b) xy (c) yz

3.4 Conclusion

A series of DFT and empirical-potential simulations of the phase-I crystal structure of ammonia have been performed with the aim of determining the experimental equilibrium crystal structure. The results have highlighted serious flaws in the neutron powder-diffraction structure determined by Hewat and Reikel. Excellent agreement has been found between the isotropic displacement parameters and vibrationally-corrected N–H/D distance determined using the DFT simulations and those found by Leclercq *et al.* at 180 K by re-refining the data of Hewat and Reikel. Lower temperature simulations have highlighted the importance of quantum dynamics on the vibrational parameters determined by crystallography. The results show that a new neutron diffraction study of ammonia would be useful to remove doubts surrounding the Hewat and Reikel dataset. Quantitative comparison with X-ray studies (even the recent multipole refinement of Boese *et al.*) is difficult because the fitting process can distort the vibrational information. Boese's study was performed at 150 K with NH_3. At that temperature, with H atoms, we expect quantum effects to still be important.

When performing the MD simulations it was found that strong thermostatting, preferably using an Anderson thermostat or the related method of Lagevin dynamics, was essential to obtain converged results. The single unit cell simulations using Nosé-Hoover chains gave substantially different results in a series of simulations.

Although the uncertainty in the experimental values complicates matters, it is clear that the present study has successfully applied and benchmarked the MD methodology for determining equilibrium structures. The next step in developing this method is to study larger molecules that will have significant contributions from internal degrees of freedom (such as torsions).

Bibliography

[1] J. v. Eerden, S. Harkema and D. Feil, *Acta Cryst. B*, 1990, **46**, 222.

[2] A. Alberti, E. Fois and A. Gamba, *Am. Mineral.*, 2003, **88**, 1.

[3] N. M. Glykos, *Acta Cryst. D*, 2007, **63**, 705.

[4] J. W. Reed and P. M. Harris, *J. Chem. Phys.*, 1961, **35**, 1730.

[5] A. W. Hewat and C. Riekel, *Acta Cryst. A*, 1979, **35**, 569.

[6] R. Boese, N. Neiderprüm, D. Bläser, A. Maulitz, M. Yu. Antipin and P. R. Mallinson, *J. Phys. Chem. B*, 1997, **101**, 5794.

[7] P. Damay and F. Leclereq, *Phys. Rev. B*, 1990, **41**, 9676.

[8] O. S. Binbrek and A. Anderson, *Chem. Phys. Lett.*, 1972, **15**, 421.

[9] J. S. Holt, D. Sadoskas and C. J. Pursell, *J. Chem. Phys.*, 2004, **120**, 7153.

[10] M. Powell, G. Dolling, G. S. Pawley and J. W. Leech, *Can. J. Phys.*, 1980, **58**, 1703.

[11] M. M. Siddick, G. J. Ackland and C. A. Morrison, *J. Chem. Phys.*, 2006, **125**, 64707.

[12] A. Hinchliffe, D. G. Bounds, M. L. Klein, I. R. McDonald and R. Righini, *J. Chem. Phys.*, 1981, **74**, 1211.

[13] S. J. Clark, M. D. Segall, C. J. Pickard, P. J. Hasnip, M. J. Probert, K. Refson and M. C. Payne, *Z. Kristallogr.*, 2005, **220**, 567.

[14] (*a*) J. P. Perdew, J. A. Chevary, S. H. Vosko, K. A. Jackson, M. R. Perderson, D. J. Singh and C. Fiolhais, *Phys. Rev. B*, 1992, **46**, 6671; (*b*) J. P. Perdew, J. A. Chevary, S. H. Vosko, K. A. Jackson, M. R. Perderson, D. J. Singh and C. Fiolhais, *Phys. Rev. B*, 1993, **48**, 4978.

[15] *CPMD, Version 3.13.2, IBM Corp. 1990-2008, MPI für Festkörperforschung, Stuttgart, 1997-2001.*, 2008.

[16] J. P. Perdew, K. Burke and M. Ernzerhof, *Phys. Rev. Lett.*, 1996, **77**, 3865.

[17] R. Car and M. Parrinello, *Phys. Rev. Lett.*, 1985, **55**, 2471.

[18] M. Diraison, G. J. Martyna and M. E. Tuckerman, *J. Chem. Phys.*, 1999, **111**, 1096.

[19] H. C. Anderson, *J. Chem. Phys.*, 1980, **72**, 2384.

[20] M. P. Allen and D. J. Tildesley, *Computer Simulation of Liquids*, Oxford University Press, 1989.

[21] C. Scheringer, *Acta Cryst. A*, 1986, **42**, 356.

[22] H. Flyvbjerg and H. G. Petersen, *J. Chem. Phys.*, 1989, **91**, 461.

[23] M. J. McGrath, J. I. Siepmann, I. W. Kuo, C. J. Mundy, J. VandeVondele, J. Hutter, F. Mohamed and M. Krack, *Comp. Phys. Chem.*, 2005, **6**, 1894.

[24] W. G. Hoover, *Computational Statistical Mechanics*, Elsiver, 1991.

[25] (*a*) S. Nosé, *J. Chem. Phys.*, 1984, **81**, 511; (*b*) W. G. Hoover, *Phys. Rev. A*, 1985, **31**, 1695.

[26] G. J. Martyna, M. L. Klein and M. Tuckerman, *J. Chem. Phys.*, 1992, **97**, 2635.

[27] T. Schneider and E. Stoll, *Phys. Rev. B*, 1978, **17**, 1302.

[28] C. L. Nye and F. D. Medina, *Phys. Rev. B*, 1985, **32**, 2510.

[29] D. J. Tobias, G. J. Martyna and M. L. Klein, *J. Phys. Chem.*, 1993, **97**, 12959.

[30] F. Leclereq, P. Damay and M. Foukani, *J. Chem. Phys.*, 1995, **102**, 4400.

[31] C. Puzzarini, *Theor. Chem. Acc.*, 2008, **120**, 325.

[32] R. W. Impey and M. L. Klein, *Chem. Phys. Lett.*, 1984, **104**, 579.

[33] W. Smith, T. R. Forrester and I. T. Todorov, *The DL_POLY User Manual*.

[34] P. E. Janeiro-Barral, M. Mella and E. Curotto, *J. Phys. Chem. A*, 2008, **112**, 2888.

[35] A. M. Reilly, D. S. Middlemiss, M. M. Siddick, D. A. Wann, G. J. Ackland, C. C. Wilson, D. W. H. Rankin and C. A. Morrison, *J. Phys. Chem. A*, 2008, **112**, 1322.

Chapter 4

Anharmonic thermal motion in nitromethane

4.1 Introduction

To develop and apply molecular dynamics (MD) simulations to the study of thermal motion from a crystallographic viewpoint it is important to choose simple, yet interesting systems. Nitromethane, CH_3NO_2, is one such system. It crystallises in the $P2_12_12_1$ space group with four molecules in the unit cell as shown in Figure 4.1.[1] The methyl group of nitromethane has a very low barrier to rotation, which results in large-amplitude motions of the hydrogen atoms around the axis of the C–N bond. This motion makes the H atoms appear to be closer to their centroid and results in smaller C–H distances than would be expected. This phenomenon is routinely seen for methyl groups in many crystal structures, even in cases where the methyl-group rotation is hindered.[2] Nitromethane is therefore a model system for one of the most common manifestations of the effects of thermal motion in crystallography.

Figure 4.1: Unit cell of d_3-nitromethane.

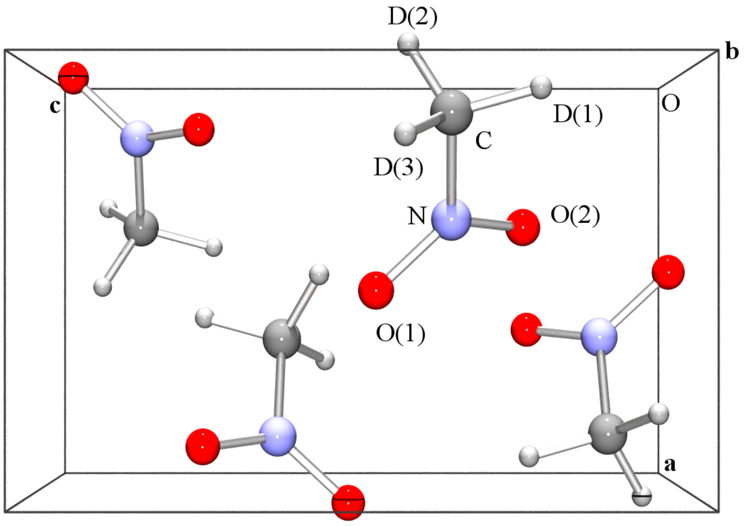

Many of the structural and dynamical studies previously reported for nitromethane have focused on the thermal motion of the methyl group. All three neutron diffraction studies of deuterated nitromethane (d_3-nitromethane) have applied some form of experimental method for correcting the C–D distances for the effects of libration and were performed at low temperatures (4.2–78 K) to minimise the amplitude of this motion.[1,3,4] Other studies have applied neutron scattering techniques to investigate the potential surface and barrier governing the methyl group libration.[5,6]

Most of the recent interest in nitromethane has focused on its role as an energetic material. A number of studies of its behaviour under high pressure[7,8] have been made as well as theoretical simulations of its physical properties.[9] Many of the theoretical simulations have applied a force field developed by Sorescu *et al.*[10] This force field is used for all of the simulations presented in this chapter as it has been widely applied to both solid-state and liquid nitromethane and has been demonstrated to reproduce key physical properties such as the thermal expansion and bulk modulus. Normally, it would be preferable to use DFT to perform the MD simulations but a previous study of nitromethane with DFT by Byrd *et al.* showed that the lack of dispersion forces in mainstream DFT functionals limited the accuracy of DFT-calculated cell vectors and other properties for this material.[11] Recent work,[12] however, has shown that Grimme-type dispersion corrections[13] improve the DFT modelling of nitromethane. Nevertheless our choice of empirical potentials will allow us to simulate larger supercells and to acquire longer trajectories, which would be at the limit for DFT-based modelling approaches. Crucially, the computational speed of force-field-based methods permits us to perform path-integral molecular dynamics (PIMD) simulations. Such simulations are essential for comparison with the low-temperature experimental data. We can also study nitromethane over a large temperature range, gathering data over an appreciable number of points to study temperature dependence of the anharmonicity and anisotropic displacement parameters (ADPs). It is important to characterise the effects of thermal motion over a large temperature range as the chemical and physical nature of a system does not always permit studies at very low temperatures ($<$ 10 K).

4.2 Experimental and theoretical methods

4.2.1 EP simulations

Empirical-potential MD simulations of d_3-nitromethane were carried out using an "in-house" PIMD simulation code written by Mr. T. Markland and Dr. S. Habershon, both of the University of Oxford, which was modified to use the force field of Sorescu *et al.*[10] Morse potentials are used to represent bond stretches, while angle bends are represented using harmonic functions. It should be noted that the harmonic bending constants given in the original paper were incorrect; the values reported by Agrawal *et al.*[14] have been used instead. The important O–N–C–D torsions were modelled as having three-fold symmetry (in the absence of the crystal field) using a cosine function:

$$V(\phi) = V_0 \left[1 + \cos(m\phi - \delta)\right], \tag{4.1}$$

where m is 3 and δ is the phase of the potential, which adjusts its minima. In the original paper values of ±90° were used. Trial and error suggested that values of ±70° reproduced the experimental torsional angles better. The agreement is still not perfect but as we might expect thermal motion to affect the experimental values we can only hope to be close enough to obtain valid corrections, not absolute agreement. Intermolecular dispersion and repulsion interactions were modelled using a Buckingham potential (Equation 2.27) with parameters originally developed for the explosive hexahydro-1,3,5-trinitro-1,3,5-*s*-triazine.[15] These parameters have been shown to be transferable to a wide range of nitro-group based energetic materials. Finally, the electrostatic interactions were modelled using a Columbic interaction evaluated using an Ewald summation.

A 5×4×3 supercell was used for all simulations. A cell of this size is roughly cubic and allows a cut-off distance of $\sim$ 10 Å, which has been used for previous simulations reported in the literature.[9,10,14]

Classical MD NVT simulations were run at a number of temperatures ranging from 4.2 K to 228 K. Sorescu *et al.* determined time-averaged lattice constants at a number of temperatures using NPT simulations. These lattice constants were either used for the equivalent NVT simulations or where no NPT simulation had been performed data from adjacent temperatures were used to estimate lattice vectors, assuming linear expansion of the cell. The temperatures and corresponding lattice parameters are given in Table 4.1. A time step of 0.5 fs was used in all simulations, together with an Anderson thermostat to ensure ergodicity. Simulations above 78 K were run for 30 ps, while those below 78 K were run for 20 ps.

Table 4.1: Temperatures and lattice parameters used in the classical-MD and PIMD simulations of nitromethane. Lattice parameters were taken from, or extrapolated from, the values of Sorescu *et al.*[10]

T / K	a / Å	b / Å	c / Å
4.2	5.2116	6.3416	8.6464
8.0	5.2119	6.3451	8.6550
15.0	5.2125	6.3516	8.6652
25.0	5.2134	6.3608	8.6935
50.0	5.2184	6.3494	8.7266
78.0	5.2195	6.3794	8.7543
100.0	5.2222	6.4173	8.7734
125.0	5.2267	6.4229	8.7979
150.0	5.2298	6.4605	8.8204
175.0	5.2373	6.4889	8.8608
200.0	5.2452	6.5167	8.8808
228.0	5.2534	6.5481	8.9195

Path-integral MD simulations were run at the same temperatures as the classical simulations using the same cell sizes. PIMD simulations at temperatures as low as 4.2 K require very large Trotter dimensions, P (Section 2.3.3). To increase the speed of the simulations the ring-polymer contraction method of Markland and Manolopoulos was applied.[16] This method exploits the fact that the electrostatic and intermolecular forces acting on the beads representing the same atom will be very similar and need only be evaluated for a subset of beads and extrapolated for the rest of them. Intramolecular contributions and the harmonic forces tethering beads together must still be evaluated in full but these calculations are far less computationally intensive than the intermolecular calculations. The result is that the computational time can reduced by a significant amount. In the case of a 32-bead simulation of liquid water the PIMD simulation only took six times as long as the classical ($P = 1$) simulation. Different values of P can be used to calculate the electrostatic interactions and the dispersion interactions. Simulations with different values of P were performed for low T simulations to converge the Trotter dimension properly. The number of beads used for each temperature is given in Table 4.2.

Table 4.2: Trotter dimensions used for PIMD simulations at different temperatures.

T / K	P_{total}	P_{vdW}	$P_{\text{electrostatic}}$
4.2	500	149	151
8.0	500	149	151
15.0	500	149	151
25.0	500	99	101
50.0	200	99	101
78.0	200	99	101
$\geq$ 100.0	100	49	51

Analysis of the trajectories was performed on the fly during the course of the simulation using every 10th step. Means, variances and covariances of each atom in the molecule were calculated using the full space-group and supercell symmetry. The uncertainties were calculated in the same manner as used for the simulations of ammonia (see Section 3.2.3). As the analysis was performed on the fly the blocking method could not be used. In some cases when comparing to experimental data the theoretical values for the 3-D probability density functions (PDFs) were also determined for each atom. As the methyl group rotates even at very low temperatures the D atoms were assigned at each step by determining the dihedral angle of each D atom relative to the equilibrium O(1)-N-C fragment. Equilibrium geometries were determined by performing 0 K MD simulations for up to 30 ps.

4.2.2 Distance corrections and conventions

There are a number of possible different structural parameters that can be determined using theory and experiment and it is important to define properly what type of parameter is being reported for the purpose of comparison. Table 4.3

shows the various types of distances that will be discussed in this chapter and others. All of these distances (apart from the **TLS** derived distance) are determined using methods that yield complete geometries so there are equivalent bond angle, dihedral angles *etc.* as well. The Gram-Charlier and Edgeworth series methods (Section 1.3.3) determine "probable" positions: they determine the maxima of the 3-D atomic PDFs, which correspond to the free-energy minima of each atom in the mean field of all other atomic motions in the crystal structure. In the case of intramolecular parameters it is likely that the probable and equilibrium parameters will be the same.

Table 4.3: Definition of different types of structural parameters.

Name	Definition
$r_{\mathrm{a,\ MD}}$	MD time-averaged distance
$r_{\mathrm{a,\ exp}}$	Experimental time-averaged distance
r_{e}	Equilibrium geometry determined using theoretical calculations
$r_{\mathrm{e,\ MD}}$	Experimental equilibrium distance determined using MD positional corrections
$r_{\mathrm{p,\ GC}}$	Experimental probable distance determined using Gram-Charlier series refinement
$r_{\mathrm{p,\ EW}}$	Experimental probable distance determined using Edgeworth series refinement
$r_{\mathbf{TLS}}$	Experimental distance determined using **TLS** corrections
Δr_{MD}	$r_{\mathrm{e}} - r_{\mathrm{a,\ MD}}$

To obtain the $r_{\mathrm{e,\ MD}}$ structure the MD distance corrections must be applied in some fashion to the experimental structure. Initially, the manner suggested in Section 3.2.3 was used to apply the MD corrections. In this approach the principal axes of the theoretical and experimental time-averaged structures are overlapped to ensure differences in the orientations of the systems perturb the results as little as possible. This is important because the corrections are defined relative to the crystal lattice and not to the molecule. If the experimental and theoretical molecular orientations differ, then the positional corrections may lead to different experimental and theoretical corrections for bond lengths and other parameters. However, this method gave spurious results for bonded distances (particularly for the 4.2 K structure discussed in Section 4.3.3), which resulted from the slightly different geometries of the experimental and theoretical molecules (*i.e.* torsions and bends) affecting the relative orientation of the molecules. Instead of overlapping the molecules, the position corrections were applied directly to the fractional coordinates of the experimental structure. In this way the experimental equilibrium structure can be obtained in a simple and consistent manner. The effect of the experimental and theoretical systems having different orientations and geometries will often be negligible and of the order of the experimental uncertainty.

Where experimental data are not available, or direct comparison is not possible, it is useful to calculate the theoretical corrections such as Δr_{MD} to give an idea of the magnitude of the effect of thermal motion.

4.3 Results and Discussion

4.3.1 Effect of quantum dynamics

The ring-polymer contraction method allows us to apply the PIMD method over the complete temperature range that solid nitromethane exists (at ambient pressure). Previous lattice dynamics studies[17] and the MD simulations of ammonia (Chapter 3) have shown that quantum dynamics can be very important to include when simulating materials at low temperatures. PIMD simulations, even using EP or semi-empirical methods, can not always be performed so it is important to understand the effects and limitations of a classical approach.

Figure 4.2: Classical (C) and quantum (Q) variances, U_{ii}, of the C and D(1) atoms in d$_3$-nitromethane from 4.2 K to 228 K.

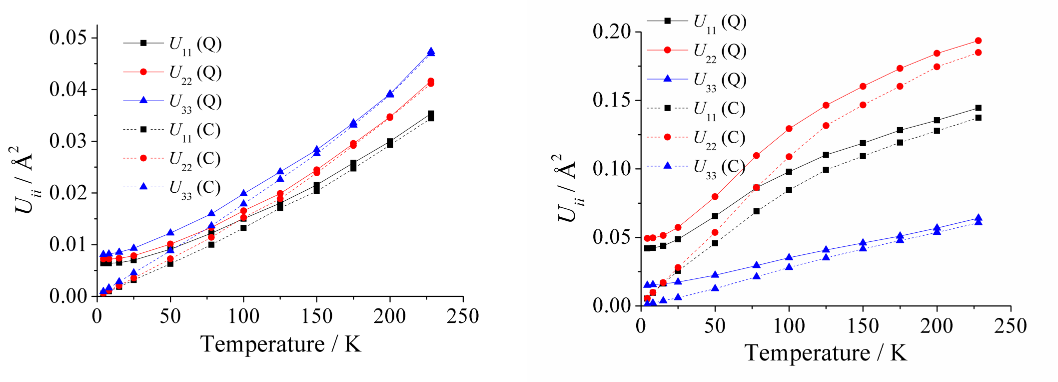

(a) C

(b) D(1)

The classical and quantum temperature dependences of the C and D(1) atom variances are shown in Figure 4.2. As expected the quantum ADPs level out as the temperature approaches 0 K, while the classical values fall rapidly to zero in the absence of any zero-point motion. By 78 K the classical D atom ADPs are 80% of the quantum value, which rises to 95% by 228 K. The remaining quantum contribution probably arises from the high-frequency internal degrees of freedom such as stretches and bends. High-frequency motions require a higher temperature to be faithfully reproduced by classical simulations. This is because a quantum harmonic oscillator with a large frequency has a larger zero-point energy contribution. The classical simulation must reach a higher temperature to compensate for this fully. For the C atom agreement at 228 K between the classical and quantum simulations is slightly closer as a result of the more low-frequency vibrations it is involved in. The shapes and orientations of the ellipsoids are very similar even at 78 K, which is encouraging. The thermal ellipsoids are determined by assuming that the probability distribution is a harmonic trivariate Gaussian. Figure 4.3 shows the thermal ellipsoids from the classical and quantum simulations at 228 K and 78 K. Figure 4.4 shows the classical and quantum 2–D xz probability density functions (PDFs) for the D(1) atom at 78 K. From this we can observe that the distributions are highly anharmonic, with both curvature and asymmetry clearly visible. It appears that the longest principal axis is reproduced well by the classical simulations but the shortest is not as big as in the quantum case. Even if we can not use classical simulations for direct comparison with experiment they may still be useful for qualitative analysis of systems with highly anharmonic potential-energy surfaces.

The differences between the classical and PIMD simulations arise because of zero-point motion and quantum-mechanical tunnelling. Quantifying this difference *a priori* is difficult as at a given temperature some vibrational modes may be better approximated than others, depending on their vibrational frequency. Feynman and Hibbs proposed a quasi-classical potential that would account for some of the quantum behaviour.[18] In this model the classical potential for a particle, $V(r)$ is

Figure 4.3: Classical and quantum thermal ellipsoids of nitromethane simulated at 228 K and 78 K.

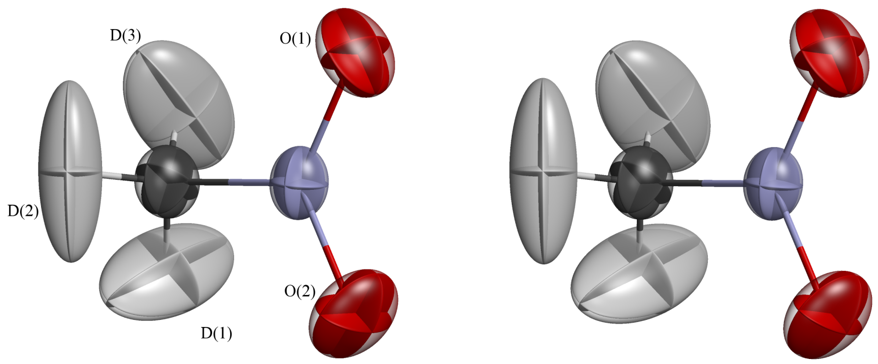

(a) Classical – 228 K

(b) Quantum – 228 K

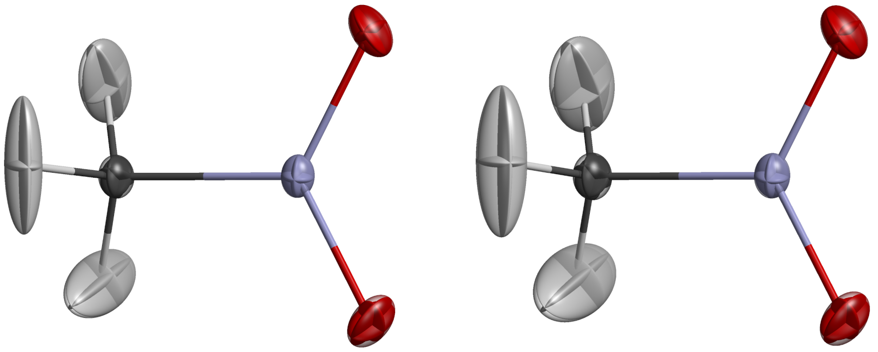

(c) Classical – 78 K

(d) Quantum – 78 K

Figure 4.4: Classical and quantum 2–D probability distributions of the D(1) atom at 78 K in the xz plane, where x is longest principal axis and z the shortest.

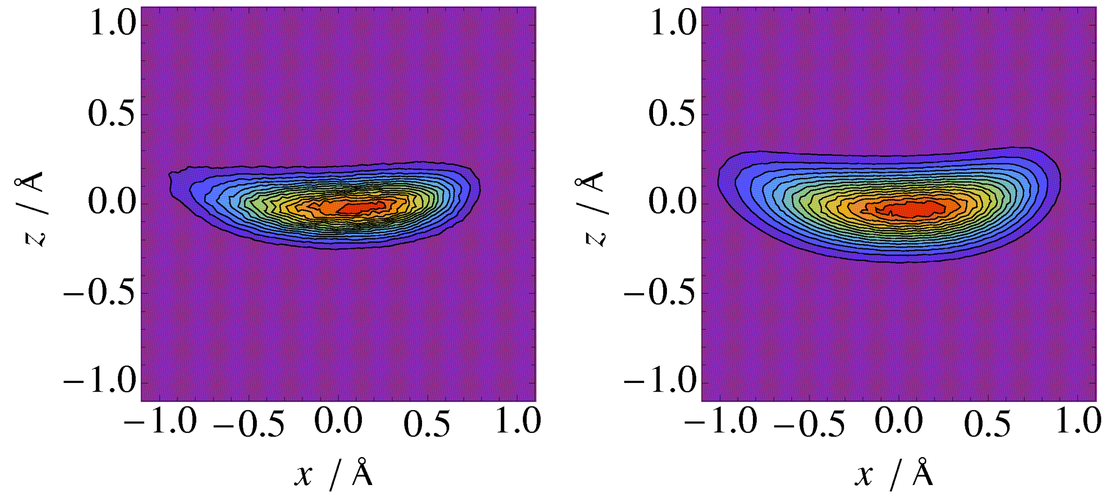

(a) Classical

(b) Quantum

replaced by an effective potential:[18]

$$V_{\text{eff}}(r_\text{c}) = \frac{1}{\sqrt{\pi \Delta r^2}} \int_{-\infty}^{\infty} V(r_\text{c} + r) \exp\left(\frac{-r^2}{\Delta r^2}\right) \text{d}r, \tag{4.2}$$

where Δr^2 is related to the free-particle radius of gyration, $r_{\text{G, free}}$, and the thermal wavelength, $\Lambda(T)$, of the free particle:[18,19]

$$\Delta r^2 = \frac{\Lambda(T)^2}{8\pi} = \frac{2}{3} r^2_{\text{G, free}} = \frac{\beta \hbar^2}{6m}, \tag{4.3}$$

where β is $1/k_\text{b}T$ and m is the mass of the particle. In Equation 4.2 the classical potential is convoluted or smeared by an isotropic Gaussian distribution. Voth showed that the quasi-classical probability density is also given by a convolution of the classical density and a Gaussian with a width of $\frac{2}{3} r^2_{\text{G, free}}$. The convolution of two isotropic Gaussians with widths a and b is a Gaussian with a width of $a+b$ so the Feynman-Hibbs (FH) approximation can be investigated by comparison of the difference between the classical and quantum values of the isotropic displacement parameter, ΔU_eq, with $\frac{2}{3} r^2_{\text{G, free}}$. These are plotted for the C atom in Figure 4.5. Note that for this analysis it is best to consider a heavy atom as the D atoms are likely to undergo some amount of tunnelling.

The plot shows that $r^2_{\text{G, free}}$ is much larger than the difference between the classical and quantum U_eq values. Therefore, the FH method significantly overestimates the quantum swelling effect. This is perhaps not that surprising as the free-particle radius of gyration is unlikely to be suitable for solid-state simulations. The FH approximation has usually been used for simulations of fluids.[20,21] In our solid-state simulations the atoms are far more confined and take part in more high-frequency vibrations. The actual radius of gyration, r^2_G, of the C-atom ring polymer might prove a more useful approximation. This could be estimated from relatively short trajectories and used to correct much longer simulations. However, as Figure 4.5 shows, this is also much larger than the difference in the U_eq values, clearly showing that the ring-polymer dynamics are not simply the smeared out dynamics of the classical system.

Figure 4.5: Plot of the free-particle radius of gyration, actual radius of gyration and difference between the classical and quantum values of U_{eq} for the C atom versus temperature. The lines through the points are provided as a guide to the eye.

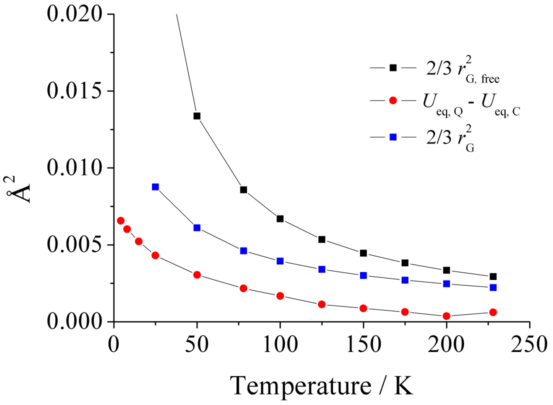

4.3.2 Comparison with previous experimental datasets

Single-crystal neutron diffraction

As detailed in the introduction, nitromethane has been studied a number of times using neutron and X-ray diffraction with an emphasis on correcting for thermal motion effects. Single-crystal neutron diffraction studies have been limited to the work of Jeffrey *et al.* at 15 K.[1] Their study determined positions and ADPs to a good degree of precision. Table 4.4 gives the experimental and theoretical (PIMD) ADPs. The agreement between the two sets of ADPs is quite good, with many of the displacement parameters being within 3σ of each other. Only the D(1) ADPs differ substantially from the experimental values. It is satisfying that the PIMD simulation yields ADPs in such good agreement with experiment. There has been renewed interest[22] in the use of *ab initio* methods to predict ADPs for use in multipole X-ray or high-pressure structural refinements. This work has demonstrated that MD simulations may offer a robust method for estimating ADPs.

The good agreement between the experimental and theoretical ADPs means that the differences between the theoretical time-averaged and equilibrium structures

Table 4.4: Experimental[1] and theoretical ADPs (in Å^2) of d$_3$-nitromethane at 15 K.

		U_{11}	U_{22}	U_{33}	U_{12}	U_{23}	U_{31}
C	Expt.	0.0059(3)	0.0074(3)	0.0103(3)	0.0015(2)	−0.0005(2)	−0.0005(2)
	MD	0.0065(1)	0.0074(1)	0.0086(1)	0.0019(1)	−0.0004(1)	−0.0009(1)
N	Expt.	0.0047(2)	0.0055(2)	0.0074(2)	0.0006(2)	0.0000(2)	0.0002(2)
	MD	0.0048(1)	0.0050(1)	0.0058(1)	0.0005(1)	−0.0002(1)	0.0001(1)
O(1)	Expt.	0.0064(3)	0.0091(3)	0.0100(3)	0.0008(3)	0.0001(3)	−0.0021(3)
	MD	0.0072(1)	0.0099(1)	0.0086(1)	0.0010(1)	0.0006(1)	−0.0023(1)
O(2)	Expt.	0.0093(3)	0.0084(3)	0.0108(3)	0.0012(3)	−0.0037(3)	0.0003(3)
	MD	0.0104(1)	0.0096(1)	0.0089(1)	0.0020(1)	−0.0036(1)	0.0006(1)
D(1)	Expt.	0.0353(6)	0.0439(7)	0.0185(4)	0.0234(6)	−0.0017(5)	−0.0087(5)
	MD	0.0438(1)	0.0514(1)	0.0161(1)	0.0317(1)	−0.0030(1)	−0.0091(1)
D(2)	Expt.	0.0184(5)	0.0259(5)	0.0610(8)	0.0046(4)	0.0149(5)	0.0190(5)
	MD	0.0163(1)	0.0225(1)	0.0599(1)	0.0020(1)	0.0090(1)	0.0170(1)
D(3)	Expt.	0.0229(5)	0.0165(4)	0.0461(6)	0.0050(4)	−0.0145(4)	−0.0084(4)
	MD	0.0212(1)	0.0171(1)	0.0435(1)	0.0029(1)	−0.0146(1)	−0.0032(1)

should provide suitable positional corrections for the experimental structure. Even at 15 K these corrections are sizeable, ranging in magnitude from 0.021 Å for the N atom to 0.115 Å for D(1). The refinement of Jeffrey *et al.* employed a **TLS** model to correct bond lengths for librational effects. The original **TLS** method could only be performed on rigid bodies. This could not be used to model the internal rotation of the methyl groups so Jeffrey *et al.* used a segmented rigid-body method,[23] whereby the CNO$_2$ and CD$_3$ were treated as rigid fragments. In addition, an anharmonic distance correction was also applied to the C–D distances to correct for potential lengthening effects due to the anharmonic nature of the bond stretching motion. The **TLS** distance corrections therefore provide a useful benchmark for the MD corrected values. The differences in distances between the experimental equilibrium and time-averaged structures are compared to the **TLS** values in Table 4.5. Very small corrections, insignificant compared to the experimental uncertainties, are found for the heavy-atom bond lengths. These are of the same magnitude but opposite in sign to the **TLS** corrections. The experimental corrections neglect the Morse contributions that result in longer experimental bonds than expected. For the C–D distances both methods determine large corrections of approximately 0.015–0.02 Å. The agreement between the two methods is not that surprising because at low temperatures the "harmonic" librational effects, that the **TLS** method deals with very well, will dominate. As the C–D corrections are more that 14 times the bond length uncertainties they are highly significant.

Table 4.5: Experimental time-averaged bond lengths of nitromethane, $r_{\mathrm{a,\ exp}}$, together with theoretical distance corrections.

	$r_{\mathrm{a,\ exp}}$ / Å	$\Delta r_{\mathbf{TLS}}{}^{a-c}$/ Å	$\Delta r_{\mathrm{MD}}{}^{d}$/ Å
rC–N	1.4855(9)	0.002	−0.0040(9)
rN–O(1)	1.2270(9)	0.004	−0.0028(9)
rN–O(2)	1.2225(9)	0.002	−0.0014(9)
rC–D(1)	1.0751(13)	0.018	0.0159(13)
rC–D(2)	1.0736(14)	0.018	0.0183(14)
rC–D(3)	1.0739(13)	0.017	0.0144(13)

[a] $\Delta r = r_{\mathbf{TLS}} - r_{\mathrm{a,\ exp}}$

[b] **TLS** corrected distances were reported to only three decimal places with no uncertainties.

[c] The C–D distances include an extra anharmonic distance correction of $-1.3168(U_D^{\|} - U_C^{\|})$, where $U_C^{\|}$ and $U_D^{\|}$ are the components of the C and D atoms' ADPs parallel to the bond.

[d] $\Delta r = r_{\mathrm{e,\ MD}} - r_{\mathrm{a,\ exp}}$

Table 4.6 gives some of the intramolecular valance angles and torsions in the experimental time-averaged and equilibrium structures. Thermal motion seems to affect the valance angles only slightly but there are substantial corrections to the torsion angles, which are greater than 30 σ. The **TLS** method is based on a assumption of harmonic curvilinear motion. It is evident in nitromethane that the rotation of the methyl group is anharmonic. This can be seen easily in the 78 K probability density function for D(1) (Figure 4.4).

Most force fields are fitted or validated based on comparison of equilibrium structures with experimental data. In the case of nitromethane such an approach will be flawed in some respect when dealing with the torsions because of the significant effect of thermal motion. As one of the principal interests in nitromethane is in the dynamics and bonding of the methyl group it is important to ensure that force fields and theoretical calculations are fitted or compared to the correct structural parameters.

As stated above there has been interest previously in the O$\cdots$C–D hydrogen bonding in nitromethane.[1] The 15 K experimental structure has a number of

Table 4.6: Selected experimental time-averaged bond angles ($\angle$) and torsions (ϕ) of d_3-nitromethane, together with the experimental equilibrium values.

Angle / °	Time-averaged	Equilibrium	Δ_{MD} [a]
$\angle$C–N–O(1)	118.2(1)	118.1(1)	−0.1
$\angle$O(1)–N–O(2)	123.7(1)	123.8(1)	0.1
$\angle$N–C–D(1)	107.7(1)	107.4(1)	−0.3
ϕ[O(1)–N–C–D(1)]	151.7(1)	148.0(1)	−3.7
ϕ[O(1)–N–C–D(2)]	−89.4(1)	−92.9(1)	−3.5
ϕ[O(1)–N–C–D(3)]	29.9(1)	26.4(1)	−3.5

[a] $\Delta_{MD} = \angle_e - \angle_a$ or $\phi_e - \phi_a$

short contacts between O atoms and D atoms. The N–O distances also differ by 0.0045(15) Å in the time-averaged experimental structure suggesting that they have different intermolecular bonding environments as a result of hydrogen bonding. The MD simulations suggest that this difference is significant with small and similar corrections to the N–O distances (Table 4.5). Table 4.7 gives some of the O$\cdots$D short contacts. The corrections to the distances are large and in every case statistically significant, with values ranging from 10 to 40 times the uncertainty in a distance. The corrections do not alter the conclusions of Jeffrey *et al.* that O(1) has four H-bonds while O(2) has none. However, having such large corrections at 15 K shows the pitfalls of ignoring thermal motion effects.

Increasingly, structural studies are focusing on comparing intermolecular distances, particularly for understanding more about the processes of co-crystallisation and polymorphism. When precision is essential it is now common to study materials at low temperatures (as was the case with nitromethane with two reports of crystal structures at 4.2 K and one at 15 K). While going to lower temperatures reduces the affect of thermal motion it does still remain significant. Methyl groups will always be extreme cases, due to the potential for large-amplitude rotations of the groups. In nitromethane there are still significant corrections for heavy-atom intermolecular distances. For example the N$\cdots$N intermolecular experimental equilibrium distance of 4.004(2) Å is 0.024 Å longer in the time-averaged structure. More studies, on a wide range of crystal structures, are required to understand the extent of this issue, especially with crystal structures being used to fit force fields and parametrise semi-empirical methods (such as the PM6 method,[24] which used structural information from the Cambridge Structural Database[25]) and also as direct input into computational techniques such as the Pixel method,[26] which uses theoretical calculations to determine lattice and intermolecular binding energies.

Table 4.7: Selected experimental time-averaged intermolecular distances (in Å) of d_3-nitromethane, together with the MD-corrected experimental equilibrium values.

Distance	$r_{\text{a, MD}}$	$r_{\text{e, MD}}$	Δr^a	Molecule
rO(1)$\cdots$D(1)	2.386(1)	2.404(1)	0.018	$\frac{1}{2}-x, 2-y, \frac{1}{2}+z$
rO(1)$\cdots$D(2)	2.582(2)	2.572(1)	−0.010	$\frac{1}{2}+x, \frac{3}{2}-y, 1-z$
rO(1)$\cdots$D(3)	2.566(1)	2.605(1)	0.039	$\frac{1}{2}+x, \frac{5}{2}-y, 1-z$
rO(1)$\cdots$D(2)	2.465(2)	2.453(2)	−0.012	$1+x, y, z$
rO(2)$\cdots$D(1)	2.692(2)	2.703(2)	0.011	$-x, -\frac{1}{2}+y, \frac{1}{2}-z$
rO(2)$\cdots$D(3)	2.859(2)	2.779(2)	−0.080	$\frac{1}{2}-x, 2-y, -\frac{1}{2}+z$

[a] $\Delta r = r_{\text{e}} - r_{\text{a}}$

4.3.3 Previous powder neutron diffraction studies

4.2 K high-resolution powder diffraction data

The crystal structure of d_3-nitromethane has been studied a number of times using powder neutron diffraction. The most precise study was performed by David *et al.*[3] using the HRPD machine at the ISIS facility. The large volume of data collected by the HRPD machine allowed for the refinement of ADPs. This study focused on comparing powder diffraction results with the 15 K single-crystal work of Jeffrey *et al.* that was discussed above. To ensure the comparison was meaningful the same **TLS** approach that was used for the 15 K data by Jeffrey was applied to correct the 4.2 K bond lengths for thermal effects. Table 4.8 compares the MD and **TLS**-determined equilibrium distances at 4.2 and 15 K. Being able to compare equilibrium structures at two temperatures is very important as the equilibrium structures (particularly bond lengths and angles) should be very similar if the corrections and indeed experimental structures are correct. The work by David *et al.* found that the single-crystal data were superior and the larger uncertainties in the 4.2 K distances ensure that the data from the two temperatures are in reasonable agreement. It is highly encouraging that differences between the equilibrium geometries at the two temperatures are smaller when the MD corrections are used in all but one case. The sole discrepancy is in the C–D(1) distance, which has a very small Morse correction compared to D(2) and D(3) due to the unusual orientation of the ADPs. We would expect very similar corrections for the three distances.

Table 4.8: Experimental equilibrium and **TLS** bond lengths of nitromethane determined at 4.2 and 15 K.

	4.2 K		15 K			
	$r_{\text{e, MD}}$ / Å	$r_{\mathbf{TLS}}$ / Å	$r_{\text{e, MD}}$ / Å	$r_{\mathbf{TLS}}$ / Å	$\Delta r_{\text{e, MD}}{}^{a}$	$\Delta r_{\mathbf{TLS}}$
rC–N	1.4803(27)	1.4867	1.4815(9)	1.4887	0.0012	0.0020
rN–O(1)	1.2294(29)	1.2402	1.2242(9)	1.2309	−0.0052	−0.0093
rN–O(2)	1.2237(31)	1.2318	1.2211(9)	1.2253	−0.0026	−0.0065
rC–D(1)	1.0809(38)	1.0926	1.0910(14)	1.0911	0.0101	−0.0015
rC–D(2)	1.0880(41)	1.0838	1.0922(14)	1.0929	0.0042	0.0091
rC–D(3)	1.0877(37)	1.0858	1.0883(14)	1.0908	0.0006	0.0050

^{a} $\Delta r = r_{15\text{ K}} - r_{4.2\text{ K}}$

4.2 K and 78 K datasets

Powder neutron diffraction data were also collected at 4.2 K and 78 K by Trevino *et al.*[4] Unlike the studies detailed above, this work did not refine ADPs for all of the atoms. Instead isotropic displacement parameters were refined for the N and O atoms, while ADPs were determined for the C and D atoms. To facilitate the refinement of the ADPs a C_3 axis of symmetry was assumed for the methyl group ADPs (about the C–N bond), significantly reducing the number of parameters. This also permitted a third-order Edgeworth series term (Section 1.3.3) to be included in the structure factors for the D atoms. The cumulant terms were determined using the results of a **TLS** rigid-body calculation. The assumption of symmetry and use of different types of structure factors (*i.e.* isotropic, anisotropic and anharmonic) means that direct comparison of the experimental structure with the MD simulations is not easily achieved.

It is still useful to compare the experimental isotropic displacement parameters

Table 4.9: Experimental isotropic displacement parameters (in Å^2) of d$_3$-nitromethane as determined by Trevino *et al.*[4] at 4.2 K and 78 K, together with the MD values.

	4.2 K		78 K	
U_{eq}	Expt.	MD	Expt.	MD
C	0.0113(8)	0.00726(1)	0.0197(21)	0.01396(3)
N	0.0043(5)	0.00498(1)	0.0099(9)	0.01142(2)
O(1)	0.0103(5)	0.00835(1)	0.0218(9)	0.01778(4)
O(2)	0.0103(5)	0.00927(1)	0.0218(9)	0.02127(4)
D[a]	0.0283(14)	0.0311	0.0712(38)	0.0661

[a] In the experiment structures the D atoms are assumed to be related by symmetry and therefore have the same U_{eq}; the quoted theoretical value is the average of the three values for the D atoms.

with the MD values. Table 4.9 lists them at 4.2 and 78 K. The agreement between the values is reasonable although the difference in the C-atom values at 4.2 K is quite large (5 σ). The two O atoms have identical displacement parameters in the experimental structures. There is no mention in the original paper of the values being constrained to be the same but it seems highly likely given the fact that they are different in the MD simulations and also in the other powder neutron structures. The change in a bond length going from one temperature to another should be comparable to the difference in the MD corrections (Δr_{MD}) between those two temperatures. Unfortunately in this case the agreement is not good. We expect bonds to appear shorter at high T as the librational effects dominate. However, some of the experimental r_{a} values actually increase with temperature; the 78 K C–N bond length is 0.008 Å longer than the 4.2 K one. This is possible but unlikely, especially above 20 to 30 K, where librational motion will begin to exceed the intramolecular motions that might lead to apparently longer bond lengths and interatomic distances. While the uncertainties are large enough to account for the differences the data should be reasonably consistent as they were collected from the same sample and apparatus.

Further disagreement between the MD simulations and experimental data occurs when comparing the time-averaged C–D bond lengths. In the experimental 78 K structure the average C–D bond length is 1.001(9) Å suggesting an equilibrium distance correction of the order of 0.09 Å. However, the MD distance correction,

Δr_{MD}, averaged over the three C-D distances is 0.058 Å. The good agreement between the MD and experimental ADPs/U_{eq} values at 4.2 and 78 K means that we should get good agreement with the experimental distances. The mix-and-match nature of the experimental refinement may account for these discrepancies.

4.3.4 Multi-temperature analysis

The reasonable agreement of the MD simulations with the previous structural studies, particularly the 15 K single-crystal study, should spur us on to extract quantitative information on the temperature dependence of the anharmonic motion. This can be obtained in a variety of ways. We can examine the ADPs and how they change with temperature. Figure 4.6 shows the U_{11} values of the co-variance matrix of the O(1) atom as a function of temperature. The U value for a harmonic oscillator is given by:[27]

$$U_{\mathrm{harm}} = \frac{\hbar}{2\omega m} \times \coth\left(\frac{\hbar\omega}{2k_{\mathrm{b}}T}\right) \tag{4.4}$$

where ω is the frequency of vibration of the oscillator and m is the oscillator mass. A fit of this function to U_{11} for O(1) is shown as a solid line in Figure 4.6. At large values of T the function will be linear while at low T it converges to a finite value representing the zero-point contribution to the motion. Deviations from the ideal harmonic behaviour were defined by Bürgi *et al.*[27] as "positive anharmonicity" when the thermal motion increased faster than the low-temperature linear behaviour would suggest and "negative anharmonicity" when the thermal motion increased less than expected. At higher temperatures more of the free-energy surface is explored. Thus positive anharmonicity represents a broadening of the free-energy surface away from the equilibrium point while a steeper surface is the case with negative anharmonicity. In Figure 4.2 the D atom clearly shows negative anharmonicity, whilst the O(1) and C atom ADPs have positive anharmonicity. In the case of the D atoms, there is an upper limit on the size of ADPs due to the pseudo axis of symmetry of the D atoms. The fact that the U_{33} value of the D(1) atom behaves normally is an indication that the anharmonicity is primarily in the x and y directions, which makes sense in terms of the orientation of the D(1) atom and the axis of rotation. Negative anharmonicity is likely to occur for rotating groups or systems with static or dynamic disorder that is modelled using split-atom sites.

Figure 4.6: U_{11} value of the O(1) atom as a function of temperature. The squares represent the MD values. The straight and dashed lines are the harmonic and quasi-harmonic fits to the MD data.

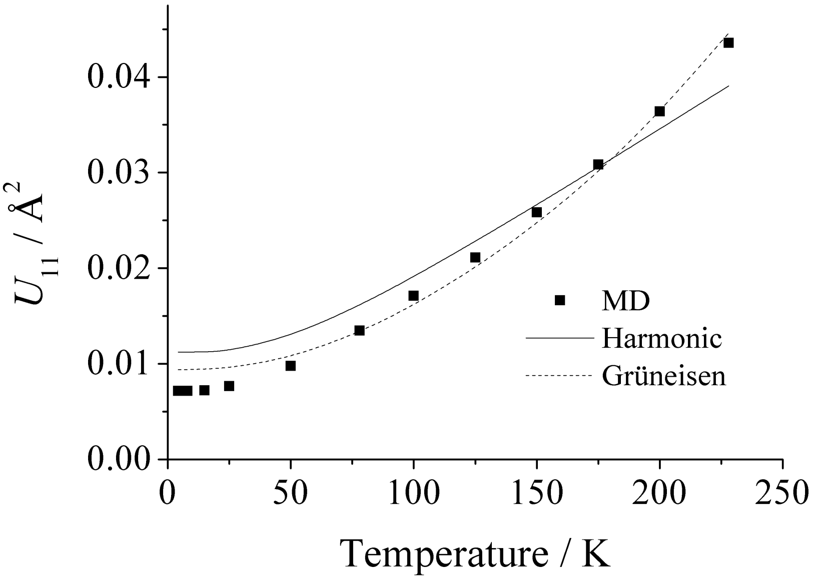

The anharmonicity in the temperature dependence of ADPs can be modelled using an effective frequency, $\omega_{\text{eff}}(T)$, in Equation 4.4. The effective frequency can be defined by a Grüneisen parameter, γ:[27]

$$\omega_{\text{eff}}(T) = \omega \left[1 - \gamma \left(\frac{V(T) - V_{\text{min}}}{V_{\text{min}}} \right) \right] \tag{4.5}$$

where V is cell volume and V_{min} is the volume at the lowest experimental temperature. The volume term is equivalent to the thermal expansion coefficient, χ_T. This approach is referred to as a quasi-harmonic model. Bürgi *et al.* analysed the temperature dependence of the ADPs of hexamethylenetetramine (HMT) by treating the molecule as a rigid body, modelling the three translational and three librational modes. Values for γ of between 2.3 and 5.3 were determined for a variety of models applied to the ADPs of HMT over the range of 15 to 298 K. For comparison, Equation 4.4, with the effective frequency given by Equation 4.5, was used to fit the U_{11} values of the O(1) atom. The thermal expansion χ_T was fitted to the function $a_1T + a_2T^2$ after Schwarzenbach *et al.*[28] and the harmonic frequency was treated as a fitting parameter. The dashed line in Figure 4.6 represents the quasi-harmonic fit, which models the temperature dependence significantly better than the harmonic model, although a multi-frequency model would yield an even better fit. The fit gives a value of 3.0(5) for the Grüneisen parameter. It has been shown by Bürgi that multi-temperature ADP data can, with a number of approximations, be used to determine correlated motions between *different* atoms.[27,29] The ADPs give information on the motions of individual atoms; information on the motion of atoms relative to each other is not available in a single diffraction experiment. Another potential use of multi-temperature MD simulations is to evaluate and study further Bürgi's approach.

Figure 4.7: Bonded distance corrections ($r_\mathrm{e} - r_\mathrm{a,\,MD}$) as a function of temperature. The lines through the points are provided as a guide.

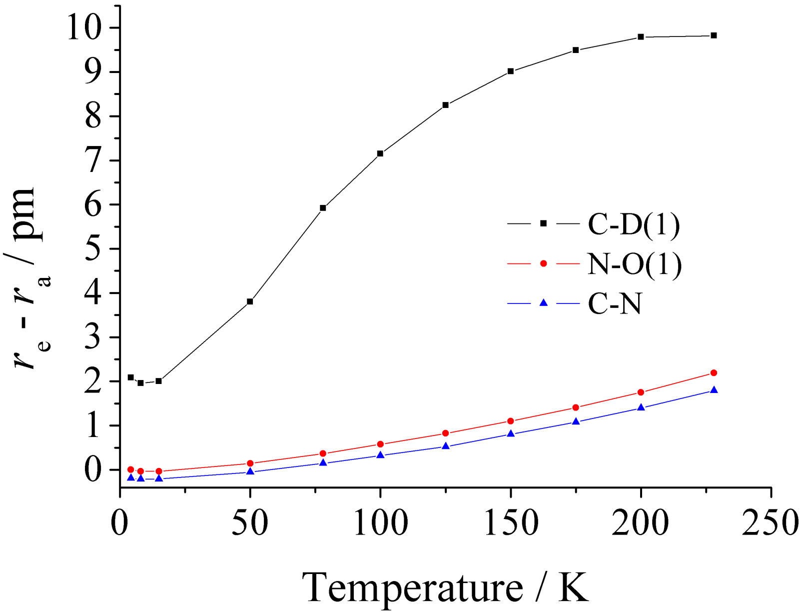

As well as studying the harmonic information contained in the ADPs we can look at the distance corrections and the numerical PDFs. Figure 4.7 shows the bonded distance corrections as a function of temperature. The C–D corrections rise to very large values of ~ 0.1 Å. As we might expect from the ADP behaviour the correction begins to plateau at higher T. In contrast the smaller C-N and N-O(1) corrections continue to rise. This tallies with the concept of positive anharmonicity, where the free-energy surface appears more anharmonic as the temperature rises. We can correlate this with the PDFs: Figure 4.8 shows the O atom xz PDF at 15 K and 228 K. At 15 K the PDF appears reasonably elliptical. However, by 228 K the distribution is egg (or pear)-shaped. The D atoms also have highly anharmonic distributions. In particular, the D(2) atom PDF (Figure 4.9) does not resemble a Gaussian PDF at all. Such anharmonic distributions can be fitted with a Gram-Charlier series or some other form of probability distribution. This will be the focus of the following chapter.

Figure 4.8: O(1) atom xz 2-D PDF at 15 K and 228 K. The x axis corresponds to the longest principal axis of the harmonic ellipsoid, while the z axis is the shortest axis.

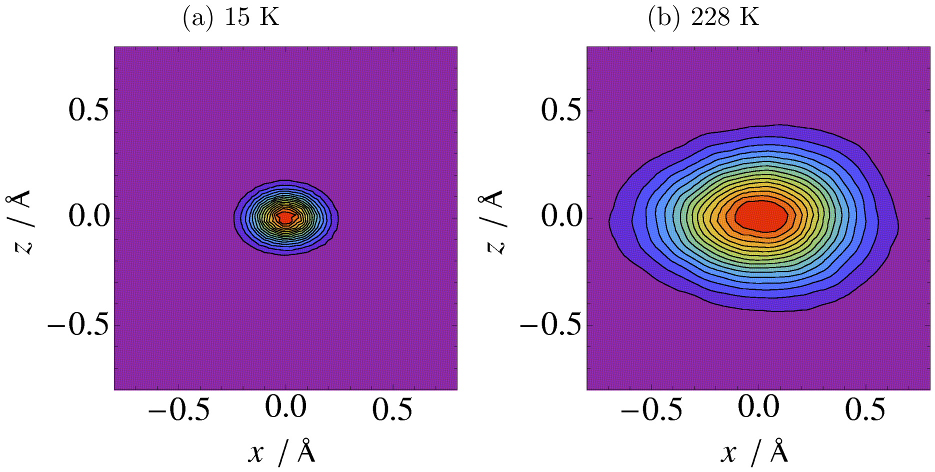

(a) 15 K

(b) 228 K

Figure 4.9: The xz 2-D PDF of the D(2) atom at 228 K.

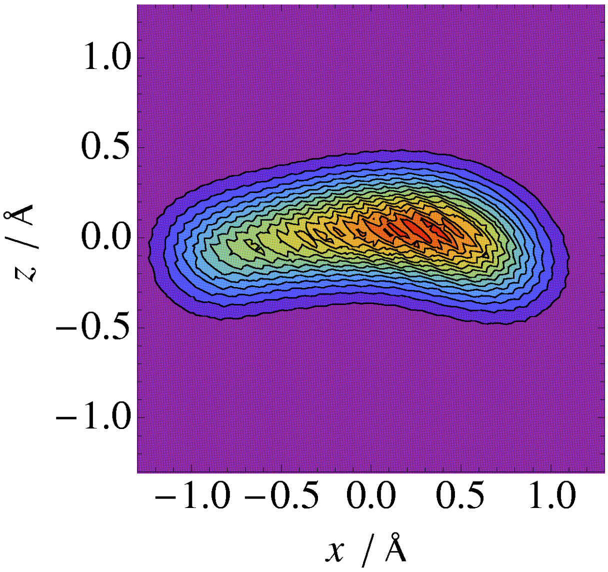

4.4 Conclusion

A series of empirical-potential path-integral MD simulations have been performed on d$_3$-nitromethane over the temperature range of 4.2 to 228 K. The results have compared favourably to the existing low-temperature neutron diffraction datasets. In particular, the experimental equilibrium structures have been determined at 4.2 and 15 K. The corrections to atomic positions are large in magnitude, ranging from 0.02 to 0.1 Å at 15 K. As a result, corrections to C–D distances, intermolecular distances and torsions are large and significant, highlighting the importance of including thermal motion effects in diffraction studies.

The use of the path-integral MD method has been crucial for determining the distance corrections at such low temperatures. A comparison was made between the full PIMD simulations and an approximation based on the work of Feynman and Hibbs, which has been used a number of times for liquid simulations. Unfortunately, the FH approximation substantially overestimates the swelling effect of the quantum regime. This is most likely a result of the stronger intra- and intermolecular forces found in the solid state.

The temperature dependence of the ADPs and correction has also been explored. The ADPs deviate significantly from the ideal behaviour expected for harmonic oscillators. It has been shown that a simple quasi-harmonic model can model the temperature dependence adequately. The deviations can be correlated with the numerical PDFs and distance corrections. In studying nitromethane the MD method has been applied to the important class of methyl groups, which are the classical example of curvilinear/anharmonic motion. However, the simulation also gives us a useful example of a skewed Gaussian distribution in the form of the pear-shaped PDFs obtained for the O atoms at high temperatures. The various numerical PDFs can be used to assess whether or not it may be possible to simplify current methods of performing anharmonic refinements, enabling the routine analysis of anharmonicity in crystal structures.

Bibliography

[1] G. A. Jeffrey, J. R. Ruble, L. M. Wingert, J. H. Yates and R. K. McMullan, *J. Am. Chem. Soc.*, 1985, **107**, 6227.

[2] C. C. Wilson, *Cryst. Rev.*, 2007, **13**, 142.

[3] W. I. F. David, R. M. Ibberson, G. A. Jeffrey and J. R. Ruble, *Physica B*, 1992, **180-181**, 597.

[4] S. F. Trevino, E. Prince and C. R. Hubbard, *J. Chem. Phys.*, 1980, **73**, 2996.

[5] S. F. Trevino and W. H. Rymes, *J. Chem. Phys.*, 1980, **73**, 3001.

[6] A. Heidemann, I. Anderson, B. Jeffryes and B. Alefeld, *Z. Phys. B*, 1982, **49**, 123.

[7] D. T. Cromer, R. R. Ryan and D. Schiferl, *J. Phys. Chem.*, 1985, **89**, 2315.

[8] M. Citroni, F. Datchi, R. Bini, M. Di Vaira, P. Pruzan, B. Canny and V. Schettino, *J. Phys. Chem. B*, 2008, **112**, 1095.

[9] L. Zheng, S.-N. Luo and D. L. Thompson, *J. Chem. Phys.*, 2006, **124**, 154504.

[10] D. C. Sorescu, B. M. Rice and D. L. Thompson, *J. Phys. Chem. B*, 2000, **104**, 8406.

[11] E. F. Byrd, G. E. Scuseria and C. F. Chabalowski, *J. Phys. Chem. B*, 2004, **108**, 13100.

[12] M. W. Conroy, I. I. Oleynik, S. V. Zybin and C. T. White, *J. Phys. Chem. A*, 2009, **113**, 3610.

[13] S. J. Grimme, *J. Comput. Chem.*, 2004, **25**, 1463.

[14] P. M. Agrawal, B. M. Rice and D. L. Thompson, *J. Chem. Phys.*, 2003, **119**, 9617.

[15] D. C. Sorescu, B. M. Rice and D. L. Thompson, *J Phys. Chem. B*, 1997, **101**, 798.

[16] (*a*) T. E. Markland and D. E. Manolopoulos, *J. Chem. Phys.*, 2008, **129**, 024105; (*b*) T. E. Markland and D. E. Manolopoulos, *Chem. Phys. Lett.*, 2008, **464**, 256.

[17] T. Pilati, F. Demartin and C. M. Gramaccioli, *Phys. Chem. Minerals*, 1998, **26**, 149.

[18] G. A. Voth, *Phys. Rev. A*, 1991, **44**, 5302.

[19] T. E. Markland, S. Habershon and D. E. Manolopoulos, *J. Chem. Phys.*, 2008, **128**, 194506.

[20] B. Guillot and Y. Guissani, *J. Chem. Phys.*, 1998, **108**, 10126.

[21] P. Kowalczyk, R. Hołyst, M. Terrones and H. Terrones, *Phys. Chem. Chem. Phys.*, 2007, **9**, 1786.

[22] A. Ø. Madsen, B. Civalleri, F. Pascale, R. Dovesi and S. Larsen, *Acta Cryst. A*, 2008, **64**, C148.

[23] C. K. Johnson, *Thermal Neutron Diffraction*, Oxford University Press, 1970, p. 132.

[24] J. J. P. Stewart, *J. Mol. Model.*, 2007, **13**, 1173.

[25] F. H. Allen, *Acta Cryst. B*, 2002, **58**, 380.

[26] A. Gavezzotti, *Z. Kristallogr.*, 2005, **220**, 499.

[27] H. B. Bürgi, S. C. Capelli and H. Birkedal, *Acta Cryst. A*, 2000, **56**, 425.

[28] D. Schwarzenbach, H. Birkedal, M. Hostettler and P. Fischer, *Acta Cryst. B*, 2007, **63**, 828.

[29] H. B. Bürgi and S. C. Capelli, *Acta Cryst. A*, 2000, **56**, 403.

Chapter 5

Fitting anharmonic atomic probability density functions

5.1 Introduction

Molecular dynamics (MD) simulations can provide us with great insight into the dynamics of molecular crystals. These insights can be particularly useful from the point of view of crystallography as the preceding chapters have shown. While it is very useful to be able to use MD simulations to determine equilibrium structures, the ultimate focus of performing these types of simulations is to collection datasets that can be used to assess the current and potential methods for modelling anharmonic thermal motion.

In this chapter the numerical probability density functions (PDFs) of ammonia, nitromethane and two other compounds have been modelled using a variety of different functions. This study is by no means complete but should serve to demonstrate how useful the numerical datasets can be. With the numerical PDFs we can assess how well the probable ($\mathbf{r}_\mathrm{p}$; defined in Section 1.3.2) and equilibrium positions of atoms agree. Such a comparison is only possible with a theoretical dataset and is very important for understanding whether it is possible to compare theoretical and (anharmonically refined) experimental structures directly without the need for some form of correction. Initial results suggest that the differences may be significant, preventing the routine determination of equilibrium structures from experimental data alone. As a further example of the usefulness of the MD datasets, two new types of anharmonic PDF are tested by fitting to the various numerical PDFs.

5.2 Simulation and analysis methods

5.2.1 MD simulations

The results of a number of MD simulations are presented and used in this chapter. The details of the simulations of ammonia and nitromethane are detailed in Sections 3.2 and 4.2.1 respectively. In the case of ammonia, only the results of the DFT simulations are used here.

Urea-phosphoric acid (1:1)

The 1:1 adduct of urea and phosphoric acid (UPA) has attracted considerable interest in the literature owing to the short, strong hydrogen bond between the urea oxygen proton and an oxygen of phosphoric acid (Figure 5.1). UPA has been studied using neutron diffraction[1] and computational methods, including plane-wave DFT.[2,3] The experimental and theoretical results show that the proton migrates from the urea to the phosphoric acid as a function of temperature and that its effective potential is likely to be skewed, particularly at lower temperatures.

Figure 5.1: Molecular structure of the 1:1 adduct of urea and phosphoric acid.

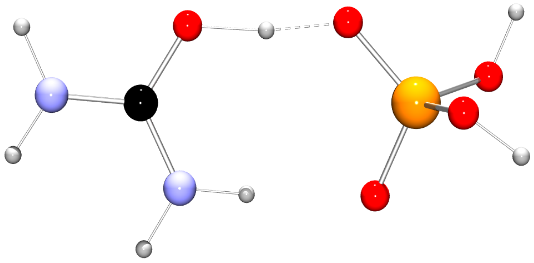

Simulations of UPA were performed at 150 K and 350 K. The simulations were carried out on unit cells (fixed at the experimental cell vectors) using the CPMD code[4] and simulation method.[5] The plane-wave cut-off energy was 1400 eV and Troullier-Martins norm-conserving pseudopotentials were used to represent the core-valence interactions.[6] The PBE functional[7] was used to model the exchange and correlation energies. An electronic timestep of 0.0725 fs was used. The temperature was regulated using a chain of Nosé-Hoover (NH) thermostats for the ions and the electrons. The 150 K MD simulation was run for a total of 24 ps, while the 350 K simulation was run for 30 ps, with data being collected every fifth CPMD step in both simulations. Analysis of the trajectories was carried out in a similar fashion to that for ND_3 using the same Fortran90 code (Section 3.2.3).

Dimethyl-urea oxalic acid (2:1)

The 2:1 adduct of dimethyl and urea oxalic acid (DMUOX) (Figure 5.2) is another structure that features short, strong hydrogen-bonding behaviour. Gaussian plane-wave (GPW) DFT[8] MD simulations of phase I of DMUOX[9] were performed by Dr. C. A. Morrison using the CP2K program.[10] The electronic wavefunction was represented in real space using double-ζ Gaussian basis functions with polarisation functions,[11] while plane-waves were used in reciprocal space to represent the electron density. A density cut-off energy of 4000 eV was used. Valence-core interactions were modelled using the GPW-optimised analytical pseudopotentials of Goedecker, Teter, and Hutter.[12,13] An NH chain was used to regulate the temperature during a Born-Oppenheimer MD simulation. A timestep of 0.55 fs was used for each simulation.

Figure 5.2: Molecular structure of the 2:1 adduct of Dimethyl-urea and oxalic acid.

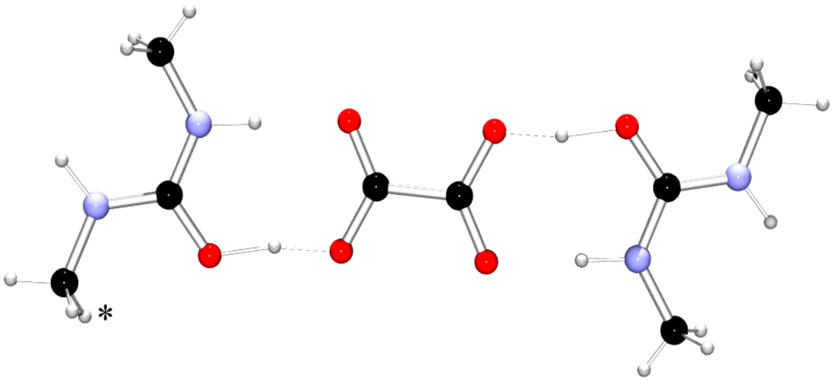

Initial analysis of the trajectory from a 350 K simulation showed that a significant amount of methyl group rotation was occurring. The trajectory was analysed further using the same method as for UPA and ND$_3$. For brevity, only the PDF of the H atom marked by an asterisk in Figure 5.2 is discussed here.

5.2.2 Analysis and fitting of probability density functions

The MD trajectories were used to determine numerical PDFs by “binning” each position adopted by an atom over the course of the MD simulation. This procedure results in 3-D histograms, which when normalised yield a PDF. 2-D and 1-D PDFs that represent marginals of the 3-D PDF with one or two variables integrated out, were determined in a similar fashion, or where the 3-D distribution was determined on the fly, by numerical integration of the 3-D distribution and re-normalisation. In most cases the histograms were determined in the coordinate system of the harmonic approximation so the distributions were centred on the numerical mean and orientated so that $U_{ij} = 0 \quad (i \neq j)$, with the longest principal axis directed along the x axis and the shortest along the z axis. Visualisation and manipulation of the data are greatly simplified in this coordinate system. For nitromethane the on-the-fly distributions were determined with a histogram of 200^3 bins. The process of analysing the datasets used only 100^3 bins as this grid was more than sufficient for fitting the PDFs. The 200^3 histogram was orientated and then re-binned to produce the coarser PDF. An artefact of this process was that this process introduced some high-frequency noise into the datasets. To aid visualisation, a low-pass Fourier filter may be applied to the numerical distribution.

The analysis and fitting of PDFs has been carried out using the Mathematica program,[14] with the fitting of the various models performed using the `NonlinearRegress` function. This uses a variety of fitting methods to find the best possible fit of a function to a dataset. It provides uncertainties and can also provide estimates of correlations. However, the latter is a time-consuming process. The maximum or mode of a distribution was found using the `FindMaximum` function in Mathematica. The function does not provide uncertainties and evaluating them would be difficult. It is a reasonable assumption that the maximum has an uncertainity similar to (but perhaps slightly larger than) that of the refined mean position. These are still smaller than typical experimental values. It is convenient to have a measure of how well a particular function fits the numerical PDFs. This is defined in a similar manner to the R factor in crystallography:

$$R = \frac{\sum |P_n(\mathbf{u}) - |P_f(\mathbf{u})||}{\sum P_n(\mathbf{u})} \times 100, \tag{5.1}$$

where P_n is the numerical (or observed) PDF and P_f is the model or fitted PDF. By definition P_n must be positive over all space and so there is no need to take its modulus. It is hard to assess what a good R-factor is for this situation so the R factor should simply be taken as a measure of the relative quality of the fit of two models to the MD dataset. Note that if high-frequency noise is present in the numerical dataset (as a result of the binning process or a short trajectory) this will adversely affect the R factor but should not affect the fitting process as this focuses on the broad, low-frequency features of the distribution.

5.3 Positions and variances

5.3.1 Harmonic and anharmonic means and variances

The Gaussian approximation of thermal motion (Section 1.3.1) has remained the most widely used method in crystallography due to its simplicity. The functions involved can be readily implemented in refinement software and the values of parameters determined can be interpreted with ease. It determines the mean (or time-averaged) position of the atom and the variance of the PDF. The variance is in part a measure of the size or extent of the PDF and therefore how far the atom moves from the mean position. In contrast the statistical methods for incorporating anharmonicity involve much more complex equations and yield parameters such as quasi-moments that are difficult to relate to the physics or chemistry of the crystal in question. However, it is important to note that the mean and variance determined from a harmonic fit may differ from the true mean, $\langle u \rangle$ (the average position adopted by the atom over time), or variance, $\langle u^2 \rangle$ (the average square displacement from the mean), that is obtained from the true probability function, P, by integration:

$$\langle u^n \rangle = \int_{-\infty}^{\infty} u^n P(u)\,\mathrm{d}u. \tag{5.2}$$

If the distribution is centred on the mean then $\langle u^1 \rangle = 0$ and $\langle u^2 \rangle$ is the variance. Some forms of anharmonic PDF [such as the Gram-Charlier (GC) series (Equation 1.28)] are formulated so that the mean and variance are determined directly as the parameters of the harmonic part of the PDF. There have only been a few studies that have considered the difference between the harmonic and anharmonic values. Scheringer[15] has shown that the differences between the harmonic and anharmonic mean bond lengths (*i.e.* the distance between the mean position of two atoms) of urea were of the order of 0.002–0.01 Å at room temperature. This effect seems small but could still be significant for a precise experiment. It is therefore useful to use the MD-derived numerical PDFs to assess how important this issue might be.

The true mean and variance of a PDF can be readily calculated numerically using Equations 3.2 and 3.3. The term “numerical” will be used to refer to the values calculated directly from the trajectory in this fashion. The difference between means obtained from harmonic and anharmonic models can be determined by fitting the MD-derived PDFs to a harmonic PDF and to a GC PDF, respectively. To simplify the analysis each of the MD-derived numerical datasets has been centred on the numerical mean position and oriented along the eigenvectors of the numerical co-variance matrix. For a harmonic system these eigenvectors correspond to the principal axes of the thermal ellipsoid. The Gaussian PDF used to model the data was of the form:

$$P(\mathbf{v}) = \frac{det(\mathbf{U}^{-1/2})}{8\pi^3} \exp(-\frac{1}{2}\mathbf{v}^T\mathbf{U}^{-1}\mathbf{v}), \tag{5.3}$$

where $\mathbf{U}$ is the co-variance matrix and $\mathbf{v} = (x - u_1, y - u_2, z - u_3)$ so that the mean position is given by $\mathbf{x} = (x, y, z)$. (PDFs used in crystallography are usually defined as describing the Cartesian displacement, $\mathbf{u}$, about a fractional mean, $\mathbf{x}$.) As the PDF is orientated along the numerical principal axes, the co-variance matrix was chosen to be of the form,

$$\mathbf{U} = \begin{pmatrix} U_{11} & 0 & 0 \\ 0 & U_{22} & 0 \\ 0 & 0 & U_{33} \end{pmatrix}. \tag{5.4}$$

The GC series PDF is of the same form as Equation 1.28. Equation 1.27 defines Hermite polynomials, H_{jkl}, centred on the mean position (where $\mathbf{u} = 0$ by definition). This expression results in the correct definition of the Debye-Waller factor for use in crystallographic refinements but for refinements of the numerical PDFs in real space it is necessary to include parameters for the mean:[16]

$$H(\mathbf{v})_{\alpha\beta\gamma\ldots} = (-1)^p \exp\left(\frac{1}{2}U_{jk}^{-1}v^j v^k\right)\left[\frac{\partial^p}{\partial v_\alpha \partial v_\beta \partial v_\gamma \ldots}\exp\left(-\frac{1}{2}U_{jk}^{-1}v^j v^k\right)\right], \tag{5.5}$$

where all indices that are repeated twice are implicitly summed over $j, k, \alpha, \beta, \gamma, \ldots = 1, 2, 3$ and the order of the polynomial, p, is given by the number of subscripts on H. The use of a diagonal co-variance matrix greatly simplifies the resulting polynomials, speeding up the fitting process. The resulting polynomials are also directed along the principal axes of thermal motion, an advantage which will be discussed further in Section 5.4. Equation 5.5 generates 10 unique third-order polynomials and 15 unique fourth-order polynomials. The odd-order polynomials skew the distribution in a variety of ways, changing the mean and probable positions of the distribution, while the even-order terms affect the variance and “peakedness”.

Table 5.1 lists the mean positions (x, y, z) obtained fitting the numerical PDFs for ammonia, nitromethane and UPA to harmonic PDFs (Equation 5.3), and anharmonic PDFs using third-order GC series PDFs. An advantage of the GC series is that the mean is still given by the harmonic part of the distribution. In general the difference between the numerical (*i.e.* the raw MD) and harmonic means is less than 1 pm (10^{-12} m). Only for the D(1) atom of nitromethane at the high temperature of 228 K is the value larger than 1 pm. For all but one case, the use of the GC series improves the agreement between the fitted mean and the numerical value. For the D(1) atom at 228 K the agreement is made worse but the strong, curvilinear anharmonicity of the D atoms in nitromethane is likely to be difficult to represent adequately with just a third-order GC series (see Section 5.5), resulting in erroneous values. The number of values in Table 5.1 is not enough to draw any meaningful conclusion. However, it is encouraging that the differences are relatively small (even at high temperatures) and that, in general, the anharmonic model improves the agreement. This means that the harmonic model is adequate for getting a good picture of the structure and estimating the mean positions. Even the values for the D(1) atom of nitromethane are small in comparison to the equilibrium positional corrections.

Table 5.1: Harmonic and anharmonic mean of selected atomic PDFs. The numerical mean is $(0, 0, 0)$.

		Harmonic mean / Å			Anharmonic mean / Å		
Atom	T / K	x	y	z	x	y	z
D – ND_3	180	−0.0037(2)	−0.0056(2)	−0.0027(1)	−0.0021(4)	−0.0005(3)	0.0010(3)
C – $MeNO_2$	15	−0.0001(2)	−0.0007(2)	−0.0002(1)	0.0000(3)	0.0000(2)	0.0001(2)
D(1) – $MeNO_2$	15	0.0077(3)	−0.0031(1)	−0.0087(1)	−0.0005(4)	0.0006(2)	0.0009(1)
O(1) – $MeNO_2$	15	0.0004(2)	−0.0006(2)	0.0013(1)	0.0000(3)	−0.0001(3)	−0.0002(2)
C – $MeNO_2$	228	−0.0029(1)	−0.0006(1)	−0.0015(1)	−0.0002(2)	0.0001(2)	−0.0008(2)
D(1) – $MeNO_2$	228	0.0072(5)	0.0085(3)	−0.0151(1)	−0.0088(7)	0.0243(3)	0.0259(3)
O(1) – $MeNO_2$	228	0.0051(1)	−0.0048(1)	0.0071(1)	−0.0005(3)	0.0000(2)	0.0000(1)
H – UPA	150	−0.0011(1)	−0.0028(1)	0.0009(1)	0.0018(3)	−0.0007(2)	−0.0006(1)
H – UPA	350	−0.0070(3)	0.0046(3)	−0.0005(2)	0.0043(6)	0.0033(5)	−0.0007(4)

The variance of the PDF is affected only by even-order terms in a polynomial expansion. A harmonic PDF models the atom as having a quadratic free-energy surface. Higher-order polynomial terms permit the potential to be broader or steeper than this. For a nearly-Gaussian distribution the three H_{iiii} $(i = 1, 2, 3)$ polynomials will have the most important contribution if these polynomials are directed along the principal axes of the system. This is because in this case they are functions of only a single variable (like in Figure 1.4) and will affect the peakedness of the three orthogonal directions separately, in keeping with the approximation of independent variables implicit in the Gaussian approximation. A GC series with only the fourth-order diagonal, H_{iiii}, terms was used to fit a number of PDFs; the harmonic, anharmonic and numerical values of the largest of the three variances, U_{11}, are given in Table 5.2. In the case of the C and O atoms of nitromethane, small differences are seen between the harmonic and numerical values. The anharmonic fit improves the agreement in some cases but taking the uncertainties into account the discrepancies are not significant. However, for the D atoms of ND_3 and nitromethane large and significant differences are found between the harmonic and numerical values. For the D atom of ND_3 the anharmonic model reduces this difference to within error. The disagreement is particularly serious at 228 K for the D(1) atom with the harmonic value being nearly 33% larger than the numerical value. The inclusion of the H_{1111} parameter does improve the agreement significantly. A full third- and fourth-order GC series would improve things further but higher-order terms might still be important. Figure 5.3 shows the numerical 2-D xz and 1-D x PDFs of the D(1) atom at 228 K, which clearly illustrate the high degree of anharmonicity that leads to both the harmonic and anharmonic fits deviating from the true mean and variance values.

Table 5.2: Harmonic, anharmonic and numerical values of U_{11} (in Å^2) for a series of atomic PDFs.

Atom	T / K	Harmonic	Anharmonic	Numerical
D – ND_3	180	0.03443(6)	0.03575(17)	0.03555(3)
C – $MeNO_2$	15	0.00980(3)	0.00978(6)	0.00968(1)
D(1) – $MeNO_2$	15	0.08342(10)	0.07626(20)	0.08065(4)
O(1) – $MeNO_2$	15	0.01046(3)	0.01049(7)	0.01041(1)
C – $MeNO_2$	228	0.04646(5)	0.04692(10)	0.04699(5)
D(1) – $MeNO_2$	228	0.38550(60)	0.25840(40)	0.28068(15)
O(1) – $MeNO_2$	228	0.07803(7)	0.07871(10)	0.07929(8)

The data in Tables 5.1 and 5.2 highlight the importance of remembering that the mean and variance determined by the standard harmonic model are still primarily fitting parameters. While they may and often are close to or within the error of the true mean or variance, their physical significance cannot be taken for granted. The temperature dependence of the ADPs (see Section 4.3.4 for an example) may give an indication of where this might be an issue.

5.3.2 Probable and equilibrium position

A single diffraction experiment tells us about the 3-D effective free-energy surface that an atom experiences in the mean field of the motions and interactions of the

Figure 5.3: Nitromethane D(1) atom PDFs at 228 K obtained by integrating 3-D PDFs.

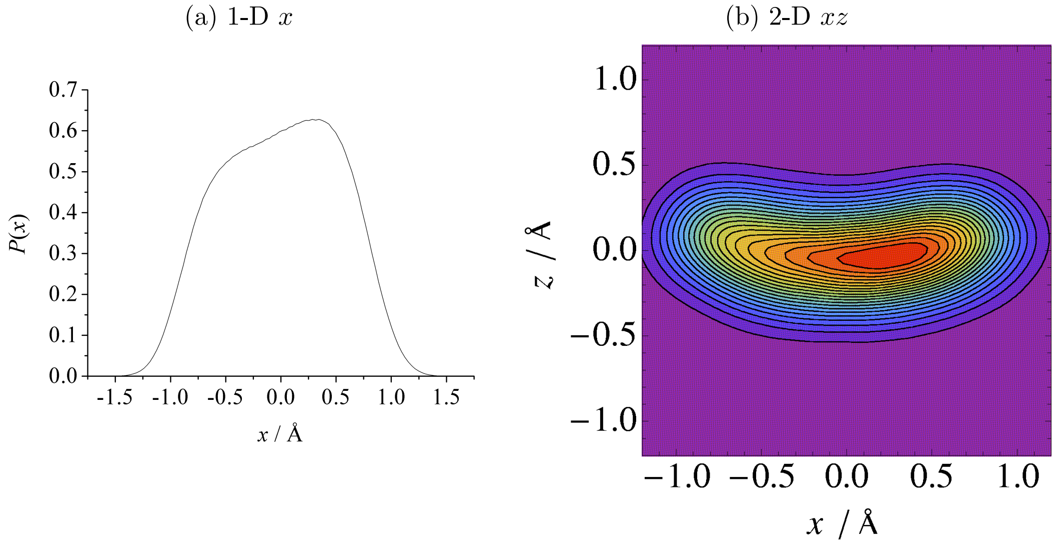
(a) 1-D x

(b) 2-D xz

other atoms in the system. A 3-D PDF describes how the atom moves on this surface. Its maximum or mode (*i.e.* where the derivative is zero) corresponds to the minimum of the surface. This mode position is termed $\mathbf{r}_\mathrm{p}$, with p standing for probable. If the potential is harmonic, then this probable position will correspond to the average position the atom adopts over time, $\mathbf{r}_\mathrm{a}$. For a harmonic system this also corresponds to that atom's minimum on the $(3N-3)$-dimensional potential-energy surface, otherwise known as its equilibrium position, $\mathbf{r}_\mathrm{e}$. If, the effective surface is anharmonic, then the fitted mean, probable and equilibrium positions may all differ.

Relating the potential and free-energy surfaces to each other requires some assumptions or the use of theory. The MD simulations allow us to determine the mean and probable positions, while geometry optimisations yield the equilibrium geometry of the system. We can therefore use the MD datasets to see how the probable and equilibrium positions compare.

Nitromethane

It is best to consider a case in which the positional corrections should be quite large to ensure that limitations of the anharmonic model (particularly in the definition of means *etc.*) do not affect the results. The magnitude of the positional correction to the nitromethane D(1) atom is 0.1153 Å at 15 K. In the thermal motion coordinate system (*i.e.* centred on the numerical mean and principal axes) $\mathbf{r}_{\mathrm{p,\ GC}}$ was, in Å, $(0.0151, -0.0063, -0.0173)$ when modelled with a third-order GC series PDF. The numerical correction from the mean $(0, 0, 0)$ to the equilibrium position, $\mathbf{r}_{\mathrm{e}}$, is $(0.1149, -0.0033, -0.009)$. The difference between the equilibrium and probable positions is very large and naturally discouraging. Figure 5.4 shows the numerical 2-D xz PDF of the D(1) atom at 15 K with equilibrium and third-order GC probable positions marked. It is clear the the discrepancy is not a result of the probable position being wrong: the GC determined maximum is clearly very close to the maximum of the numerial PDF, which in turn is far from the equilibrium position. A similar situation is found for the other D atoms as well, with the majority of the equilibrium correction being along the longest principal axis in each case. This implies that the methyl group rotates going from the equilibrium to probable structure. The value of $\mathbf{r}_{\mathrm{p}} - \mathbf{r}_{\mathrm{a}}$ is very small for the C atom, with a magnitude of only 0.0016 Å. The magnitude of the equilibrium correction is much bigger at 0.0365 Å. Similar corrections are seen for the other heavy atoms. In general there is a large contribution to the equilibrium correction for each atom that grows with temperature and is not accounted for by the probable correction. However, for the D(2) atom the magnitude for the correction is ~ 0.057 Å over the full temperature range. This may be a result of the "static" equilibrium correction cancelling the part that arises from thermal motion.

Ammonia

For the D atom of ammonia the agreement between the probable and equilibrium corrections is much better, with $\mathbf{r}_{\mathrm{e}} - \mathbf{r}_{\mathrm{p}} = (-0.0012, -0.0043, -0.0013)$. The magnitudes of the corrections are much smaller than in nitromethane with $|\mathbf{r}_{\mathrm{e}}|$ being only 0.0176 Å, and taking the uncertainties in the positions and the nature of the fitting process into account, the differences between the probable and equilibrium positions are not that significant. The small size of the corrections may stem from the much higher symmetry of the ammonia crystal structure.

Figure 5.4: The xz 2-D PDF of the D(1) atom at 15 K. The black dot indicates the third-order GC probable position, while the white dot is the equilibrium position.

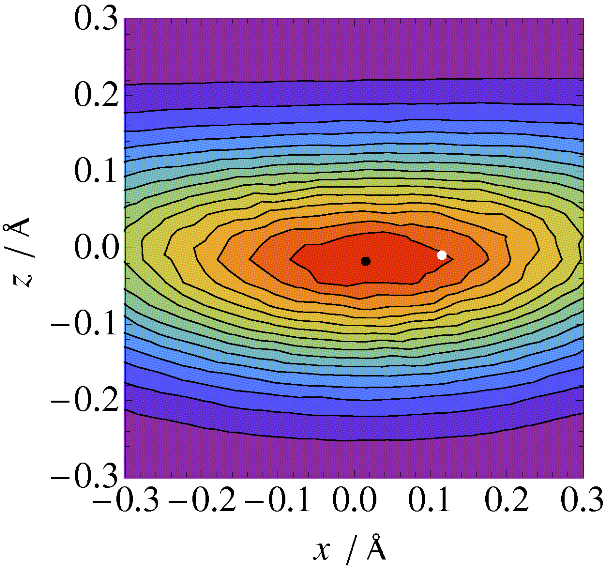

This makes the potential and free-energy surfaces less complicated.

UPA

The migratory proton of UPA has, as we might expect from its behaviour, a non-Gaussian PDF. The 150 K distribution [shown in Figure 5.5(a)] is asymmetric or egg-shaped. The distribution features far more high-frequency noise compared to the nitromethane and ammonia distributions because the size and nature of the nitromethane and ammonia simulations permitted longer trajectories and larger datasets. In general, DFT-MD simulations will produce noisier distributions. At 350 K the distribution, which is shown in Figure 5.5(b), appears to be more Gaussian like. The shape and temperature dependence of the free-energy surface of the migratory proton has been of considerable interest in recent publications.[2,3]

A consequence of thermal expansion is that different cell vectors were used for the two simulations. This means that the equilibrium positions must be different in the two structures. However, the equilibrium O–H and O$\cdots$H distances are not affected by this; the latter is 1.344 Å at 150 K and 1.346 Å at 350 K. To determine the probable positions of the two O atoms and the H atom a third-order GC series was fitted to each of the MD datasets at both temperatures. The equilibrium position of the H atom at 150 K (relative to the numerical mean) is $(-0.0169, 0.0273, 0.0104)$. The GC probable position is $(-0.0212, 0.0056, 0.0024)$ giving magnitudes of 0.0338 Å for the equilibrium correction and 0.0225 Å for the probable (GC) correction. At 350 K the equilibrium correction for the H atom is 0.0677 Å but the probable correction is only 0.0190 Å. A more direct measure of how the system changes would be to compare the probable bond lengths at the two temperatures. At 150 K rO–H = 1.1089 Å and rO$\cdots$H = 1.3289 Å. At 350 K rO–H = 1.1468 Å and rO$\cdots$H = 1.2981 Å. The minimum of the effective potential might change due to the change in cell vectors but if the potential is the same at the two temperatures then the bond lengths calculated from the probable positions ($\mathbf{r}_\mathrm{p}$) should be the same.

This illustrates that for atoms with very shallow potential-energy surfaces (such as that for a migratory proton) the probable position may be unsuitable for determining “equilibrium” bond lengths. However, in fitting the anharmonic PDF we do learn a considerable amount about the proton’s migration. In the past simulations have been used to get this sort of information but if sufficient quality data are collected then the anharmonicity and temperature dependence of the potential could be studied experimentally.

Figure 5.5: The simulated xz 2-D PDF of the migratory H-atom of UPA.

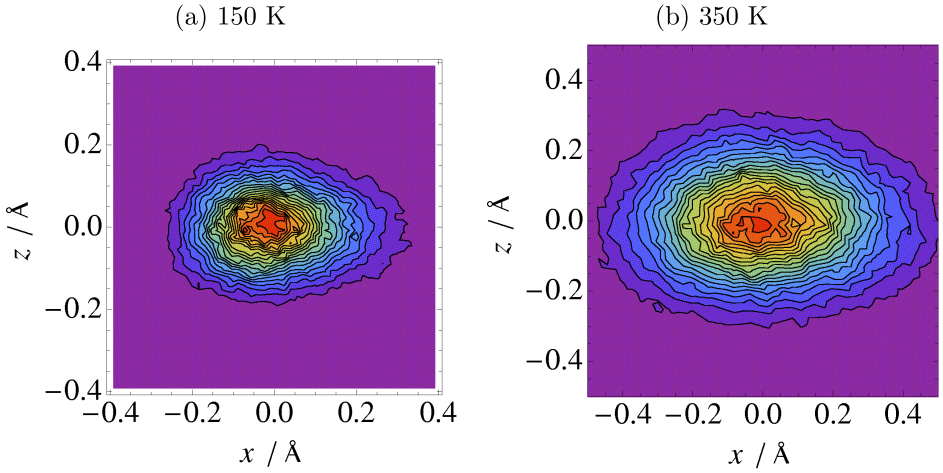

Experimental equilibrium structures

The MD simulations allow us to determine experimental equilibrium structures but at significant cost in terms of computational time and effort. While this might change with better theoretical methods and computational hardware and software for the present it would be highly desirable to determine the equilibrium geometry directly from the experiment without the need for time-consuming MD simulations. This goal was a major motivation for the present work. Unfortunately, the results of the calculations to date, particularly for nitromethane and UPA, suggest that this will not be possible, because there are large differences between correction to the equilibrium position and that to the most probable position. In nitromethane the effect is quite large and repeated attempts were made to optimise the equilibrium geometry to ensure it represented the true minimum. However, annealing MD simulations (where the temperature is gradually lowered to 0 K) starting from 40 and 100 K both gave essentially the same equilibrium geometry and position corrections as the initial optimisation.

That we can not determine equilibrium geometries experimentally is naturally quite discouraging but it is physically reasonable. The structure factor relies on an assumption that each atom can be treated independently: we only obtain a picture of what an atom does in the mean field of all the other (vibrating) atoms. This is a further manifestation of the phase effect. The 3-D PDFs obtained from a diffraction experiment are marginals of the full PDF that corresponds to the $(3N-3)$ dimensional free-energy surface. The minimum of this distribution might well provide a better estimate of an equilibrium geometry. Constructing such a $(3N-3)$ distribution is difficult without any information on the correlation of each 3-D PDF with another to each other.[17,18] The correlations do affect the shape of the 3-D distributions and as Bürgi *et al.* have shown[18–20] this sort of information is obtainable from multi-temperature analyses.

It should be stressed that the present study is limited to only a few compounds. A broader study is necessary for firm conclusions. Such a study might extract information on correlations from the MD simulation and use them to calculate the full ($3N - 3$) PDF, which may shed light on whether the corrections found in nitromethane and the other molecules do make sense physically.

Nevertheless, the refinement of probable positions is still very useful for a number of reasons. First, the R factor and therefore reliability of the structure will be greatly improved for systems where anharmonic motion is important. It is quite likely that a number of structures are deemed unacceptable for publication or deposition simply because the approximation of thermal motion is inadequate. Secondly, the correlations between atoms will still be apparent in the 3-D PDFs. We would expect that bonded distances and angles will be very close to their equilibrium values because of the strength of bonding interactions. At the very least the probable and anharmonic mean are more useful and meaningful parameters to report than the harmonic mean alone. The C–D(1) bond length obtained from the probable positions of the C and D atoms at 15 K is 1.0886 Å. The equilibrium value is 1.0880 Å. The close agreement is perhaps somewhat fortuitous as improvements could be made to the anharmonic model (see Section 5.5) but the result is at least encouraging.

5.4 Orientation of anharmonic PDFs

The preceding sections have employed GC series centred and orientated along the principal axes of thermal motion using a coordination transformation based on the numerical co-variance matrix. In crystallographic use the GC series is defined by Equation 1.27, with the standard co-variance matrix, $\mathbf{U}$, having non-zero off-diagonal elements.[16] Perhaps surprisingly, the resulting Hermite polynomials are not directed along the crystallographic axes nor are they directed along any particularly significant directions (unless symmetry dictates that this be the case). This can be illustrated using 2-D Hermite polynomials. Figure 5.6(a) shows a bivariate normal distribution, while (b) and (c) show the skewing effect of H_{111} and H_{222}. Neither of the two skewing functions is directed along the principal axes of the PDF. In the case when $U_{ij} = 0$ they are directed along the principal axes.

Figure 5.6: Effect of Hermite polynomials on a bivariate Gaussian PDF with $U_{11} = 1$, $U_{22} = \frac{2}{3}$ and $U_{12} = \frac{1}{2}$.

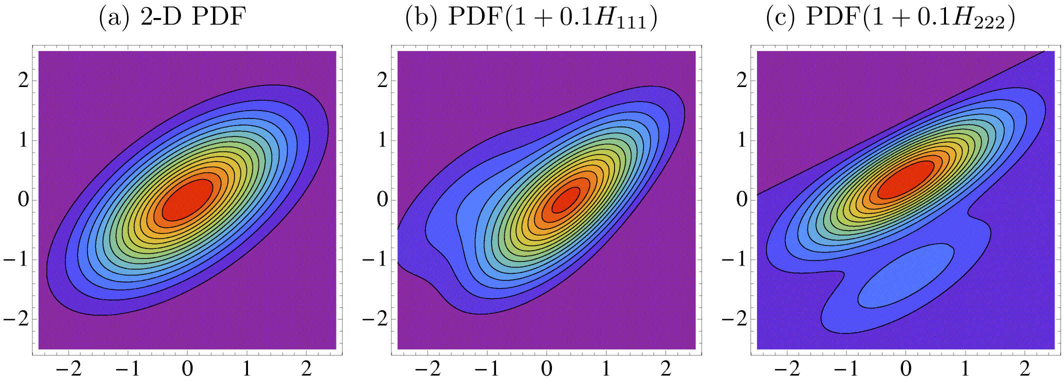
(a) 2-D PDF (b) PDF$(1 + 0.1H_{111})$ (c) PDF$(1 + 0.1H_{222})$

For some situations, such as when the three U values of an atom are very similar or there is a very complex and anharmonic distribution, the standard crystallographic formulation is perfectly acceptable. However, for some simpler forms of anharmonic PDF it may be more economical to use only a few Hermite polynomials and then refine the three parameters that orientate them. Alternatively, the axis system dictated by the harmonic approximation could be used. In nitromethane the anharmonicity in the D atoms is clearly along the largest principal axis. We can compare the general third-order GC fit of one of the PDFs with a fit orientated in the principal axis system. For this comparison, the distributions have both been centred on the anharmonic mean. The general GC expressions become far more complex if the mean is included in the anharmonic part so for both the general and orientated fits the mean has been fixed at the anharmonic value of $(0, 0, 0)$. In a crystallographic refinement the “mean” is fitted separately from the Debye-Waller factor. The resulting third-order quasi-moments for the D(1) atom at 15 K are given in Table 5.3. All ten of the general GC series quasi-moments are large and significant as the $c_{ijk}/\sigma_{c_{ijk}}$ values show. In comparison the oriented distribution has only three large values, c_{111}, c_{112} and c_{113}. The remaining seven quasi-moments are quite small and their corresponding contributions to the probability function are negligible compared to the other three. Another benefit of the orientated frame of reference is that we can associate the quasi-moments with specific contributions. For example, without plotting any density maps, we know that H_{111} skews the PDF along

Table 5.3: Third-order quasi-moments (in Å^3) for the general and orientated fits of the D(1) atom of nitromethane at 15 K. The pre-factor and multiplicities required for use in a crystallographic refinement have been omitted.

	General		Orientated	
	c_{ijk}	$c_{ijk}/\sigma_{c_{ijk}}$	c_{ijk}	$c_{ijk}/\sigma_{c_{ijk}}$
c_{111}	0.000114	100	-0.000593	48
c_{222}	-0.000381	277	0.000006	5
c_{333}	0.000025	113	-0.000001	2
c_{112}	-0.000155	52	0.000524	41
c_{122}	-0.000542	166	0.000059	9
c_{133}	-0.000184	213	0.000018	6
c_{113}	0.000550	376	0.001314	140
c_{123}	0.001457	530	0.000061	9
c_{223}	0.000896	550	0.000046	21
c_{233}	-0.000211	238	-0.000008	5

the longest principal axis. At higher temperatures all of the c_{ijk} values become significant but the c_{111}, c_{112} and c_{113} values still give the largest contribution, being more than a order of magnitude bigger than the other values.

The general GC series Debye-Waller factor (Equation 1.31) is formulated along the crystallographic axes (in keeping with its definition in real space). To use another axis system we must modify the structure-factor equation accordingly. The key component is the transformation matrix, **A**, that relates the crystal lattice axes to the desired axis system. We need to transform the orientated **U** matrix and GC coefficients into the crystal frame of reference. The matrices of third- and higher-order GC *polynomials* are contravariant tensors.[21,22] This means that the same transformation that changes the basis of the crystallographic lattice applies to them. The matrix of *coefficients* of contravariant tensors (such as the matrix of c_{ijk} values or the fractional coordinates) transform with the inverse transpose transformation matrix and are referred to as covariant tensors. For an n^{th} order tensor the transformation from $\mathbf{L}$ to $\hat{\mathbf{L}}$ is given by:

$$\hat{L}_{ijk...} = T_{iq}T_{jr}T_{ks}....L_{qrs..} \quad i, j, k, q, r, s = 1, 2, 3 \ , \tag{5.6}$$

where **T** is the appropriate contra- or co-variant 3×3 transformation matrix and all indices appearing twice are implicitly summed over. The one-particle potential

(OPP) method (Section 1.3.3) is typically formulated along the principal axes of thermal motion and features a power series similar to the GC series. Tanaka and Marumo[23] derived the required expressions for the harmonic and anharmonic parts of an OPP structure factor oriented along an arbitrary set of axes. In their notation,

$$\mathbf{A} = \begin{pmatrix} \mathbf{a}_1.\mathbf{i} & \mathbf{a}_2.\mathbf{i} & \mathbf{a}_3.\mathbf{i} \\ \mathbf{a}_1.\mathbf{j} & \mathbf{a}_2.\mathbf{j} & \mathbf{a}_3.\mathbf{j} \\ \mathbf{a}_1.\mathbf{k} & \mathbf{a}_2.\mathbf{k} & \mathbf{a}_3.\mathbf{k} \end{pmatrix}, \tag{5.7}$$

where $\mathbf{a}_i$ is the i^{th} lattice vector, **i**, **j** and **k** are the unit vectors along the desired axis system. To orientate the probability distribution along the principal axes of thermal motion, the vectors **i**, **j** and **k** should be derived from the eigenvector matrix of **U** (defined in the crystallographic basis). The eigenvector matrix can either be found numerically or take the analytical form of Kronenburg.[24] The inverse transformation is given by:

$$\mathbf{A}^{-1} = \begin{pmatrix} \mathbf{b}_1.\mathbf{i} & \mathbf{b}_1.\mathbf{j} & \mathbf{b}_1.\mathbf{k} \\ \mathbf{b}_2.\mathbf{i} & \mathbf{b}_2.\mathbf{j} & \mathbf{b}_2.\mathbf{k} \\ \mathbf{b}_3.\mathbf{i} & \mathbf{b}_3.\mathbf{j} & \mathbf{b}_3.\mathbf{k} \end{pmatrix}, \tag{5.8}$$

where $\mathbf{b}_i$ is the i^{th} reciprocal-lattice vector. The harmonic Debye-Waller factor orientated along the crystal lattice $[\mathbf{H} = (h, k, l); \mathbf{Q} = 2\pi\mathbf{H}\mathbf{b}$, where $\mathbf{b} = (\mathbf{b}_1, \mathbf{b}_2, \mathbf{b}_3)^T]$ but using the desired **U** matrix is given by:

$$\hat{P}(\mathbf{Q}) = \exp(-2\pi^2\mathbf{H}^T\mathbf{A}^{-1}\mathbf{U}_\text{c}\mathbf{A}^{-1\,T}\mathbf{H}) \tag{5.9}$$

where $\mathbf{A}^T$ is the transpose of **A** and $\mathbf{U}_\text{c}$ is the diagonal variance matrix in the preferred coordinate system. The anharmonic part of the structure factor can be obtained using Equation 5.6 and the appropriate transformation matrix. In Tanaka and Marumo's notation letting $\mathbf{Q} = 2\pi\mathbf{H}\mathbf{A}^{-1}$ produces the correct power-series expansion.

5.5 Curvilinear PDFs

5.5.1 Hermite polynomials

For molecular crystals the most important form of anharmonic motion is librational or curvilinear motion. The GC and Edgeworth series, both of which use Hermite polynomials in real space, have been applied a number of times to model such motion.[25] As well as statistical methods, kinematic models (see Section 1.3.3) have also been employed. As the statistical series expansions are nearly always truncated to third or occasionally fourth order it is difficult to assess their merit in modelling the true PDF. For a third-order GC series, the bending of a distribution is achieved primarily using the H_{iij} (or H_{ijj}) polynomials, as we have seen above for nitromethane. Figure 5.7 shows the probability density contribution of a bivariate H_{122} polynomial. The density contribution of a polynomial is given by $P(\mathbf{u})_{\mathrm{harm}} \times c_{ijk\ldots}H(\mathbf{u})_{ijk\ldots}$. It is evident from Figure 5.7 (and the appropriate equations) that H_{ijj} bends the j^{th} axis about the i^{th} one.

Figure 5.7: The probability density associated with a bivariate Hermite polynomial, H_{122}. (The x axis is horizontal; dark probability densities indicate negative contributions while lighter indicates positive contributions.)

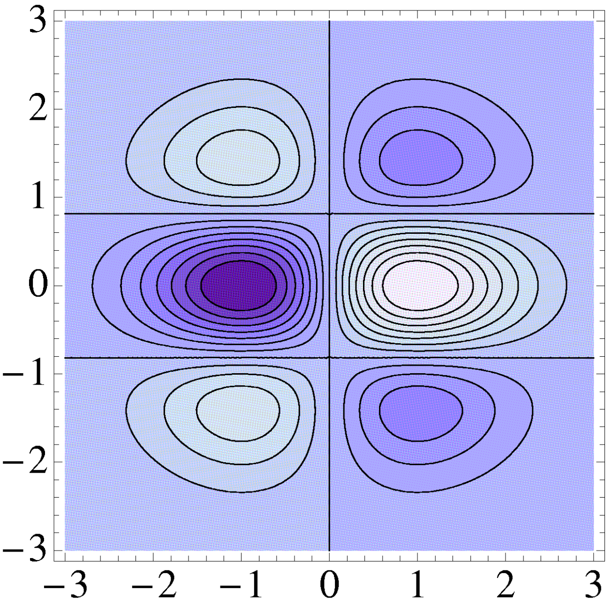

5.5.2 Parabolic coordinate system

As well as perturbing a Cartesian Gaussian PDF with polynomials we might also consider a change of the coordination system. In particular, librational motion could be represented as having a circular, parabolic or higher-order even-polynomial path. Following a suggestion by Dr. K. R. McLean[26] we consider a parabolic transformation of the coordinates, $\mathbf{u}$, of a trivariate Gaussian:

$$\begin{aligned}\hat{u}_1 &= u_1 \\ \hat{u}_2 &= u_2 + k_1 f(u_1) \\ \hat{u}_3 &= u_2 + k_2 f(u_1),\end{aligned} \tag{5.10}$$

where $f(u_1)$ is a function of u_1, which for a parabolic transformation is given by u_1^2 and k_1 and k_2 are the bending constants. This transformation turns lines parallel to the y and z axes into parabolas, bending the coordinate system along the x-axis. For simplicity we can formulate the PDF in a coordinate system where $U_{ij} = 0$; the methods outlined in the previous section can be used to give a general PDF, which takes the form:

$$P(\hat{\mathbf{u}}) = \frac{det(\mathbf{U}^{-1/2})}{8\pi^3} \exp\left[\frac{1}{2}\left(-\frac{u_1^2}{U_{11}} - \frac{(u_2 + k_1 u_1^2)^2}{U_{22}} - \frac{(u_3 + k_2 u_1^2)^2}{U_{33}}\right)\right]. \tag{5.11}$$

Figure 5.8 shows the density contribution of performing this change of basis from Cartesian to parabolic coordinates. The function gives the desired curving effect. A PDF of the form given in Equation 5.11 might be a better approximation for a librating atom because the density contribution is more realistic for curvilinear motion. The Hermite polynomial (Figure 5.7) has two nodes along the longest axis, adding density near the mean, while it removes density further away. To incorporate parameters representing the mean we can use a PDF of the form:

$$\begin{aligned}P(\hat{\mathbf{u}}) = &\frac{det(\mathbf{U}^{-1/2})}{8\pi^3} \\ &\times \exp\left[\frac{1}{2}\left(-\frac{(u_1 - x)^2}{U_{11}} - \frac{(u_2 + k_1 u_1^2 - y)^2}{U_{22}} - \frac{(u_3 + k_2 u_1^2 - z)^2}{U_{33}}\right)\right],\end{aligned} \tag{5.12}$$

where $\mathbf{x} = (x, y, z)$ represents the mean when $k_1 = k_2 = 0$.

Figure 5.8: The difference density map $[P(\mathbf{u}) - P(\hat{\mathbf{u}})]$ of a bivariate distribution with $\hat{u_1} = u_1 + 0.2u_2^2$. (The x axis is horizontal; dark probability densities indicate negative contributions while lighter indicates positive contributions.)

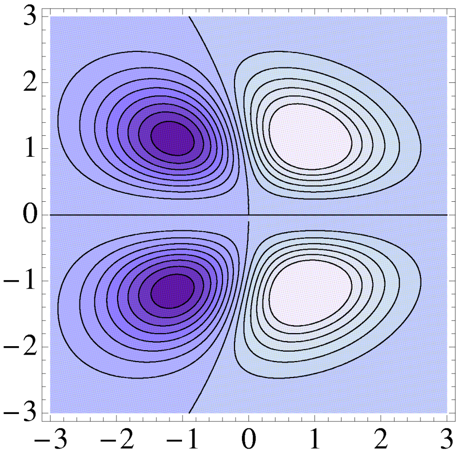

Nitromethane

The D atoms of nitromethane represent a perfect system for studying modelling of the librational motion of methyl groups. However, it is evident from the values in Table 5.3 that the D(1) PDF is skewed as well as being bent. Therefore to model the D atoms properly a PDF of the form:

$$P(\hat{\mathbf{u}})\left(1 - c_{111}H_{111}\right), \tag{5.13}$$

was used. The Hermite polynomials were defined using the normal Cartesian Gaussian PDF. This skewed parabolic PDF gave an agreement factor of 13.6% when fitted to the numerical PDF. The 16 parameter third-order GC fit (3 means, 3 variances and 10 quasi-moments) to the D(1) atom of nitromethane at 15 K gave an R-factor of 14.3%, while the trivariate harmonic model gave a fit of 19.3%. The difference between the GC and parabolic fits may not be significant statistically but it is clear that they both provide a much better fit to the distribution than the harmonic model. The full GC model has 7 more parameters than the parabolic but if we restrict the GC series to the three most important parameters (*cf.* Table 5.3) then they have the same number of parameters.

At 228 K the Gaussian PDF R-factor is 30.3%, while the GC and skewed parabolic fits give values of 23.1 and 22.3%, respectively. The GC and parabolic xz 2-D PDFs are shown in Figure 5.9(b) and (c) together with the numerical PDF. While both distributions are bent, neither match the large asymmetry seen in the numerical PDF. They also extend much further out than the numerical distribution. In Section 5.3.2 it was shown how the fourth-order GC parameters were important for representing the true variance (and hence size) of the D(1) PDF. Including only the H_{111}, H_{112} and H_{113} polynomials the agreement factor is 24.1%, perhaps suggesting that the other parameters are still important at higher temperatures. This is encouraging from the point of view of using the parabolic PDF as it fits better with far fewer parameters. The k_1 and k_2 values are -0.1614 and -0.2134 respectively. While these values have dimensions of Å^{-1}, it is important to remember the value of U_{ii} they are associated with. As U_{33} is much smaller than U_{22} the x axis will be bent mostly in the z direction.

If we include the three diagonal fourth-order Hermite polynomials in the GC model we obtain a fit of 18.5%, while with a distribution of the form

$$P(\hat{\mathbf{u}})\left(1 - c_{111}H_{111} + \sum_{i}^{3} c_{iiii}H_{iiii}\right), \tag{5.14}$$

a fit of 18.2% was obtained. The corresponding 2-D xz PDFs are plotted in Figure 5.9(d) and (e). The inclusion of the fourth-order terms allows the distributions to model the asymmetry much better. Visually, the agreement could still be better; the extent of the PDF remains too large. The parabolic PDF produces a more realistic curvature but evidently requires more even-order Hermite polynomial terms to produce a better fit. Of the three diagonal terms only the H_{1111} term seems important. Its value of -9.96×10^{-3} Å^4 is two orders of magnitude larger than the two other values. Examining the xy, xz and yz 2-D distributions it is clear that the vast majority of the anharmonicity is the xz plane. In two dimensions there are only five unique fourth-order terms. Adding the H_{1111}, H_{1133}, H_{1333} and H_{1113} Hermite polynomials to the expansion in Equation 5.13 reduces the R factor slightly but affects the visual appearance of the distribution marginally suggesting that the H_{1111} term is the most important in this type of system and that a full fourth-order refinement might not improve things that much. Adding in the sixth-order diagonal terms reduces the parabolic PDF agreement index to 17.8% but the general shape is still very similar to that in Figure 5.9(e).

Figure 5.9: 2-D xz PDFs of the D(1) atom of nitromethane at 228 K.

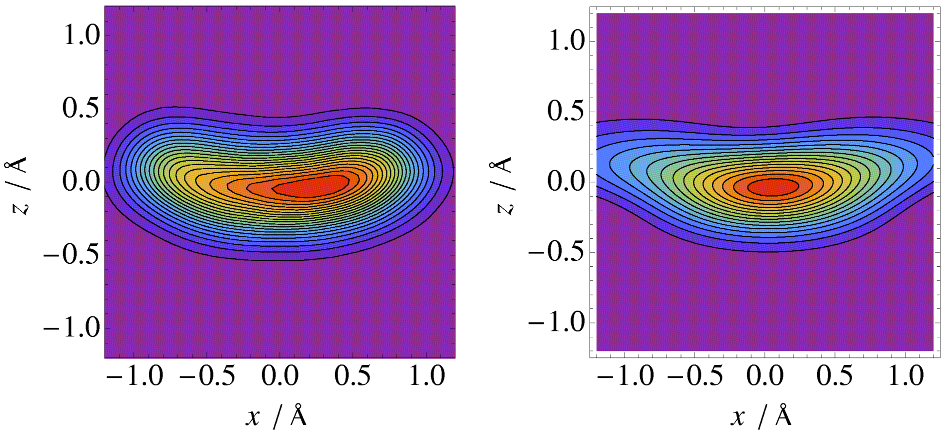

(a) Fourier-filter Numerical PDF

(b) third-order GC series PDF

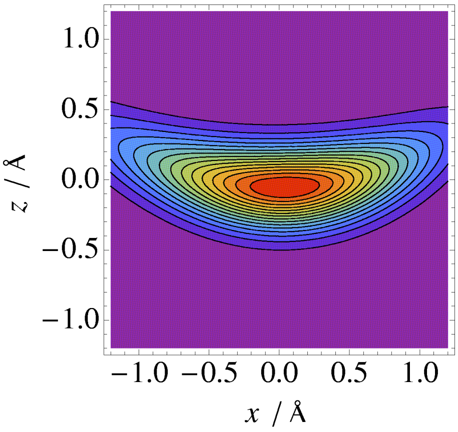

(c) Skewed parabolic PDF

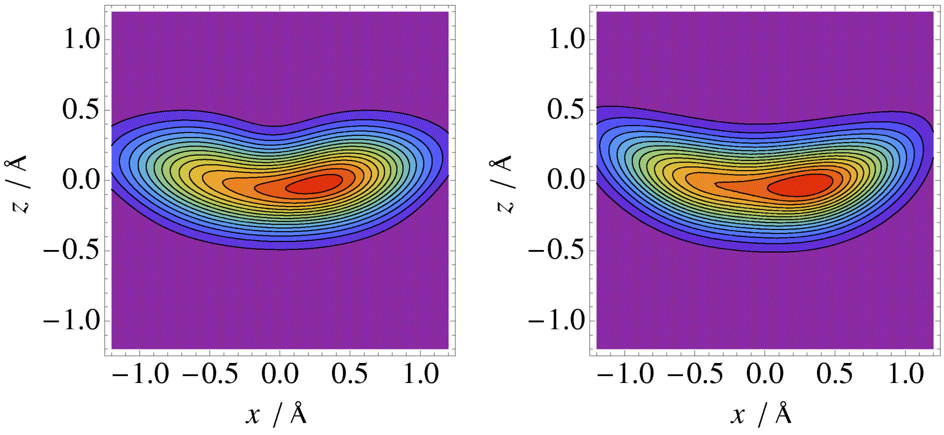

(d) Fourth-order GC series PDF

(e) Fourth-order skewed parabolic PDF

It is hard to assess the relative merit of the GC and parabolic refinements from the R factors alone. The maxima or modes of the respective PDFs may give an indication of how well they model the data. For the full 3-D PDF the fourth-order GC refinement [Figure 5.9(d)] the maximum, relative to the mean, is $(0.1875, -0.0090, -0.0529)$, while the fourth-order parabolic fit [Figure 5.9(e)] has a 3-D maximum at $(0.2995, -0.0052, -0.0343)$. The difference is quite large. Interestingly, if we consider only the xz plane and integrate out the y variable in the PDFs the maxima are $(0.274032, -0.0272024)$ and $(0.290595, -0.0354248)$, for the GC and parabolic fits, respectively. These positions are plotted on the numerical 2-D xz PDF in Figure 5.10. To facilitate comparison, a low-pass Fourier filter was applied to the numerical PDF. In 2-D there is little to choose between the two positions. It does seem more realistic for the maximum of the x coordinate in three dimensions to be close to that in two dimensions as is the case with the parabolic distribution. In fact, looking at the 1-D and 2-D distributions (Figure 5.3) it is evident that the maximum is broad and relatively poorly defined. Fitting a third-order GC series to the C atom and using the parabolic maximum for the D(1) atom, a probable C-D(1) bond length of 1.086 Å is obtained, which compares well with the r_e value of 1.089 Å. The GC series fit for the D(1) atom gives a bond length of 1.074 Å.

Figure 5.10: Numerical 2-D xz PDF of the D(1) atom of nitromethane. The black dot indicates the parabolic PDF maximum, while the white dot is the maximum of the limited fourth-order GC series PDF.

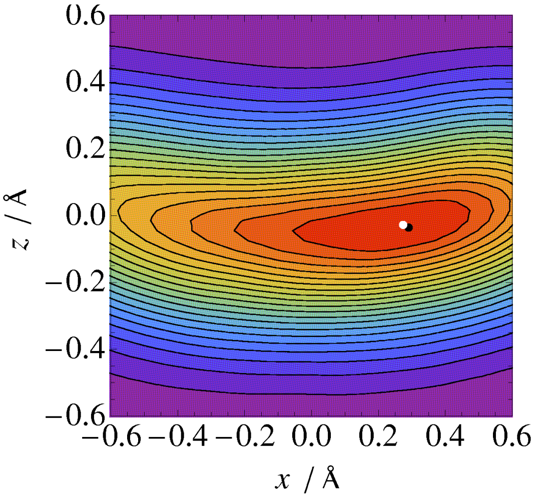

For the D(1) atom of nitromethane the parabolic PDF of Equation 5.14 consistently produced the best agreement with the numerical dataset. This is in part because the direction of curvature matches the principal axes of thermal motion quite well. The D(2) atom of nitromethane has a much more lop-sided PDF [Figure 5.11(a)], which should favour the GC series over the parabolic PDF. Fitting the limited fourth-order GC series leads to an R factor of 17.9%, while the fourth-order parabolic PDF gives a fit of 20.0%. Figures 5.11(b) and (c) show the GC and parabolic 2-D xz PDFs. The skewness of the PDF is such that the third-order H_{111} term dominates the parabolic distribution and leads to regions of negative probability on the right-hand side of the plot. A smaller region of negative probability is encountered in the fourth-order GC series. These regions of negative probability are one of the main disadvantages of PDFs based on polynomial expansions, although in some cases it is acceptable as long as the regions are small.[22,27] Noting that the H_{1111} term was the only fourth-order term to be significant for the D(1) atom we can fit a distribution with the corresponding sixth- and eighth-order terms:

$$P(\hat{\mathbf{u}})\left(1 - c_{111}H_{111} + c_{1111}H_{1111} + c_{111111}H_{111111} + c_{11111111}H_{11111111}\right). \tag{5.15}$$

This fit is shown in Figure 5.11(d). The agreement factor for this model is 16.1%. Refining a third-order GC series with the fourth, sixth and eighth-order x axis terms leads to hardly any improvement over the fit shown in Figure 5.11(b). The probable C-D(2) bond length with the parabolic model is 1.078 Å. The eighth-order GC value is 1.068 Å. The equilibrium value is 1.089 Å, while the r_a value is 0.977 Å, showing that both fits capture most, if not all, of the desired distance correction.

Figure 5.11: 2-D xz PDFs of the D(2) atom of nitromethane at 228 K. The dark purple region indicates the lowest probability, which in some cases is negative.

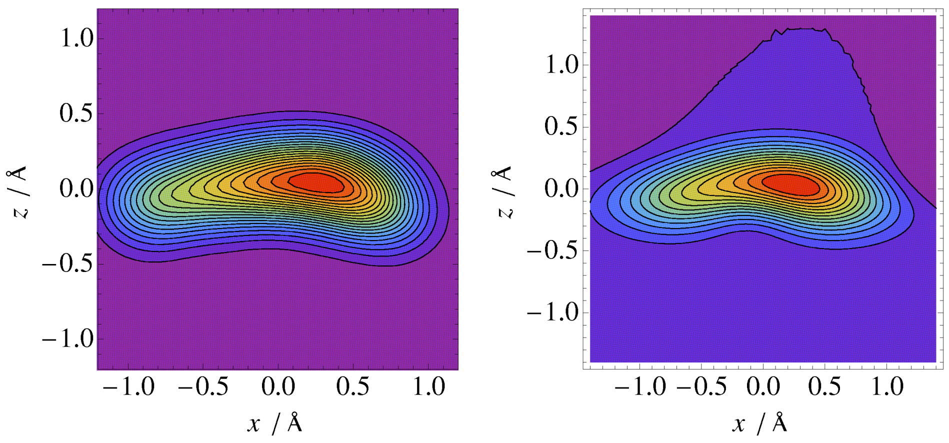

(a) Fourier-filtered numerical PDF

(b) Fourth-order GC PDF

(c) Fourth-order parabolic PDF

(d) Eighth-order parabolic PDF

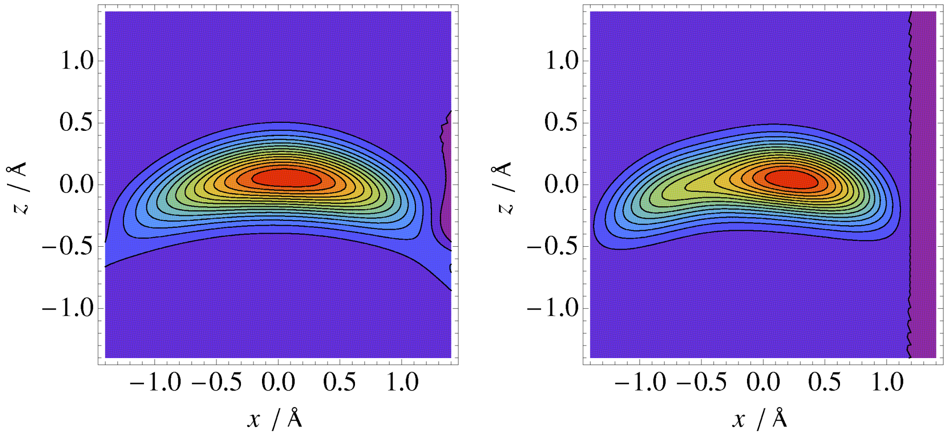

DMUOX

The methyl groups of DMUOX provide a useful dataset to validate the results obtained by applying the parabolic PDFs (Equations 5.13–5.15) to model the PDFs of the D atoms of nitromethane. The PDF of a methyl hydrogen was fitted using the limited fourth-order GC series and Equation 5.15 in the same way as for nitromethane. As with nitromethane the fourth-order parameters were essential to realistically model the asymmetry of the distribution. The numerical and parabolic distributions are shown in Figure 5.12. The parabolic fit appears to be quite good but the numerical distribution is particularly noisy, hindering proper comparison between the parabolic and GC fits.

Figure 5.12: 2-D xz PDFs of one of the H atoms of DMUOX.

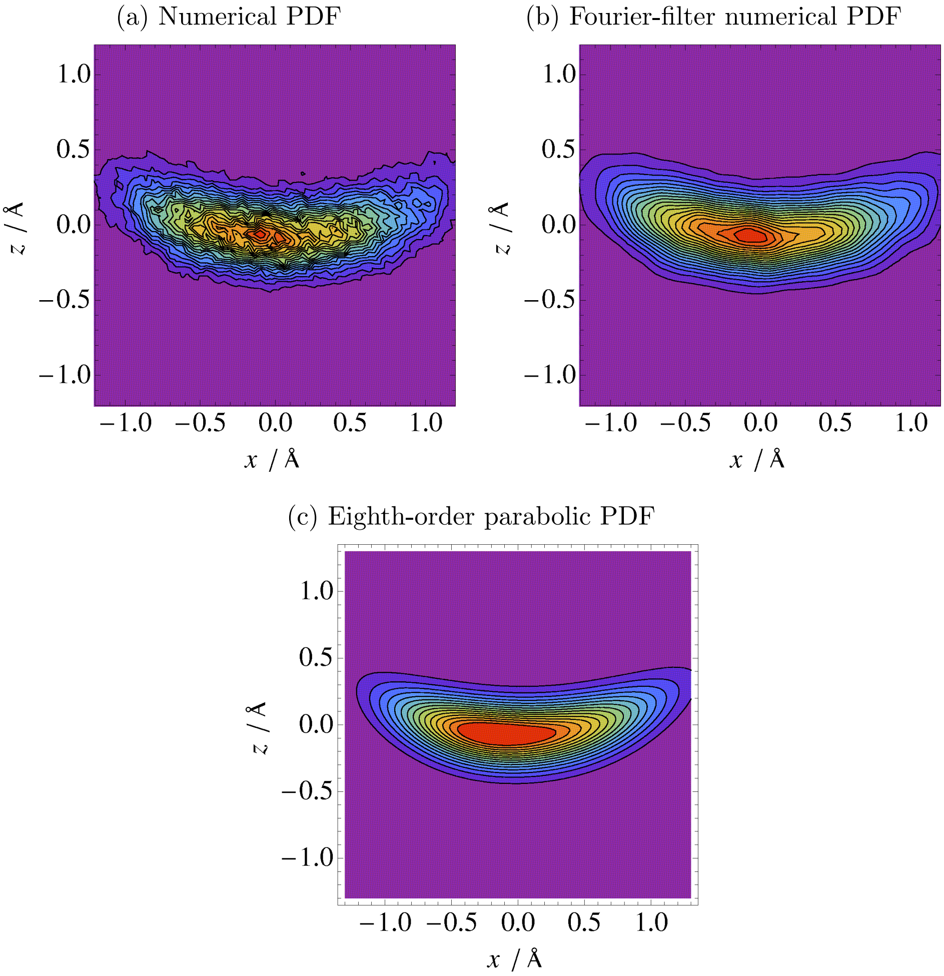
(a) Numerical PDF

(b) Fourier-filter numerical PDF

(c) Eighth-order parabolic PDF

Mean and variance

One of the strengths of the Gaussian, GC and Edgeworth series is that the mean and variances of the model distribution are directly determined as fitting parameters. The nature of the parabolic PDF results in the mean and variance terms from a normal Gaussian distribution no longer corresponding to the actual mean and variances of the distribution. Instead they must be found by applying Equation 5.2. For a PDF of the form given by Equation 5.12 this gives the mean coordinates as

$$\begin{aligned}\bar{u_1} &= x \\ \bar{u_2} &= y - k_1(x^2 + U_{11}) \\ \bar{u_3} &= z - k_2(x^2 + U_{11}).\end{aligned} \tag{5.16}$$

Equation 5.2 yields the non-centred moments of the distribution. For $n = 1$ this gives the mean. For $n = 2$ this gives the variance plus the mean squared. Thence, combining Equations 5.2 and 5.16 yields variances of

$$\begin{aligned}\sigma_1^2 &= U_{11} \\ \sigma_2^2 &= U_{22} + 2k_1^2 U_{11}(2x^2 + U_{11}) \\ \sigma_3^2 &= U_{33} + 2k_2^2 U_{11}(2x^2 + U_{11}).\end{aligned} \tag{5.17}$$

Naturally, when k_1 or k_2 is zero then $\mathbf{x}$ and $\mathbf{U}$ have their usual significance as the mean and co-variance matrix of the distribution.

Structure factor

To use the parabolic PDF in a crystallographic refinement we have to find its Fourier transform or characteristic function. If we consider only curvature along a single direction then letting $k_1 = 0$ and $k_2 = k$ in Equation 5.12 gives a distribution of the form:

$$P(\hat{\mathbf{u}}) \propto \exp\left[\frac{1}{2}\left(-\frac{(u_1 - x)^2}{U_{11}} - \frac{(u_2 - y)^2}{U_{22}} - \frac{(u_3 + ku_1^2 - z)^2}{U_{33}}\right)\right]. \tag{5.18}$$

The characteristic function is found by by finding the expectation value of $\exp(i\mathbf{x}.\mathbf{Q})$ [*i.e.* $\langle\exp(i\mathbf{x}.\mathbf{Q})\rangle$]. This is given by

$$\begin{aligned}\hat{P}(\mathbf{Q}) = &\exp\left(i(yQ_2 + zQ_3)\right) \times \exp\left(-\frac{1}{2}(Q_2^2 U_{22} + Q_3^2 U_{33})\right) \\ &\times \exp\left(-\frac{i(x + iQ_1U_{11})^2}{2U_{11}^2 kQ_3 - iU_{11}} - \frac{x^2}{U_{11}}\right) \times \left(\sqrt{1 + 2iU_{11}kQ_3}\right)^{-1}.\end{aligned} \tag{5.19}$$

The first two exponential terms represent the standard harmonic parts of the Debye-Waller factor for the Q_2 and Q_3 directions. If $k = 0$ then the usual Gaussian distribution is obtained for the Q_1 coordinate as well. For curvature in two directions (*i.e.* like Equation 5.12) only the third and fourth terms in Eqaution 5.19 are affected:

$$\begin{aligned}\hat{P}(\mathbf{Q}) = \hat{P}(Q_2, Q_3)_{\mathrm{harm}} \times \exp\left(-\frac{i(x + iQ_1U_{11})^2}{2U_{11}^2(k_1Q_2 + k_2Q_3) - iU_{11}} - \frac{x^2}{U_{11}}\right) \\ \times \left(\sqrt{1 + 2iU_{11}(k_1Q_2 + k_2Q_3)}\right)^{-1}.\end{aligned} \tag{5.20}$$

Equations 5.19 and 5.20 are of a suitable form and length for use as analytical functions in refinement programs. Unfortunately, when the parabolic PDF is expanded with Hermite polynomials, as in Equations 5.13–5.15, the analytical form for the structure factor is prohibitively complicated and long.

An alternative to using an analytical Debye-Waller factor is to perform a numerical Fourier transform of the analytical PDF. Such an approach has been suggested before for methods such as the OPP approximation.[22] It has also been applied by Hohlwein[28] to calculate structure factors for orientationally-disordered molecules. However, for a variety of reasons the numerical approach has not been widely tested. First, the analytical GC series is considered superior to the OPP approximation, the main anharmonic model that would benefit from a numerical approach. Secondly, the computational effort in terms of coding and more importantly the evaluation time would have been prohibitive when the majority of the investigations of such methods were carried out (the 1970s and 80s). Finally, it is preferable to have an analytical form to determine the various parameters directly in the refinement.

Neither of the second or third reasons is a substantial obstacle to implementing a PDF such as the parabolic one studied here. Harmonic refinements that took a significant amount of computational time and effort ten years ago can be performed in minutes with modern codes and computer hardware. An analytical form for the PDF is preferable but if the model is inadequate then the parameters determined may be wrong, leading to inaccurate crystal structures.

5.6 Skew-normal distribution

Curved (bent) PDFs only demonstrate one effect of anharmonic thermal motion. Skewed or asymmetric PDFs are seen both for nitromethane [Figure 4.8(b)] and for UPA (Figure 5.5). The GC series can effectively model asymmetry using the diagonal odd-order polynomials such as H_{111}. One disadvantage of using polynomial expansions is that for such odd-ordered polynomials there must exist a region of space where the probability is negative. In many cases this region will be far from the atom and also small in magnitude. However, at high temperatures negative regions can be a serious issue[27] and they are clearly visible in the probability distributions fitted to the D(2) atom PDF (Figure 5.11).

The skew-normal (SN) distribution was suggested by Azzalini for modelling asymmetric datasets.[29] For a one dimensional case it has the form

$$P(x)_{\mathrm{SN}} = 2P(x)\Phi(ax), \tag{5.21}$$

where $P(x)$ is a Gaussian with mean, u, and variance, U, and $\Phi(ax)$ is a cumulative density function of the form

$$\Phi(ax) = \frac{1}{2}\left[1 + \mathrm{erf}\left(\frac{a(u-x)}{\sqrt{2U}}\right)\right]. \tag{5.22}$$

where the error function, erf(x), is given by:

$$\mathrm{erf}(x) = \frac{2}{\sqrt{\pi}}\int_0^x \exp(-t^2)\,\mathrm{d}t. \tag{5.23}$$

The error function is limited to the range -1 to 1 and is shown in Figure 5.13. Being limited to that range ensures that a PDF of the form of Equation 5.21 can not have any negative regions. The multivariate SN distribution is defined differently depending on the nature of the problem and whether or not correlation/orientation parameters are necessary. For our purposes it seems reasonable to start by skewing along the principal axes of the distribution. The distribution then takes the form:[30]

$$P(\mathbf{u})_{\mathrm{SN}} = P(\mathbf{u})_{\mathrm{harm}} \prod_{i=1}^{3} \left[1 + \mathrm{erf}\left(\frac{a_i(x_i - u_i)}{\sqrt{2U_{ii}}} \right) \right]. \tag{5.24}$$

The form of Equation 5.24 skews each direction of the PDF in turn. This ensures that the distribution can not have negative probability. When the skew coefficients a_i are zero we recover the normal Gaussian distribution. The mean of the distribution is

$$\bar{u_i} = x_i + \sqrt{\frac{2}{\pi}} \delta_i \sqrt{U_{ii}}, \tag{5.25}$$

with $\delta_1 = a_i / \sqrt{1 + a_i^2}$. The variance is given by

$$\bar{u_i^2} = \sigma_i^2 = U_{ii}(1 - \frac{2}{\pi}\delta_i^2). \tag{5.26}$$

The characteristic function of the PDF given by Equation 5.24 is given by:[30,31]

$$\hat{P}(\mathbf{Q}) = \exp\left(i\mathbf{x}\mathbf{Q}\right) \exp\left(-\frac{1}{2}\mathbf{Q}^T\mathbf{U}\mathbf{Q}\right) \prod_{i=1}^{3} \left[1 + \mathrm{erf}\left(iQ_i\delta_i\sqrt{U_{ii}} \right) \right]. \tag{5.27}$$

Figure 5.13: Functional form of the error function with $a = 1$, $U = 1$ and $u = 0$ (*cf.* Equation 5.22).

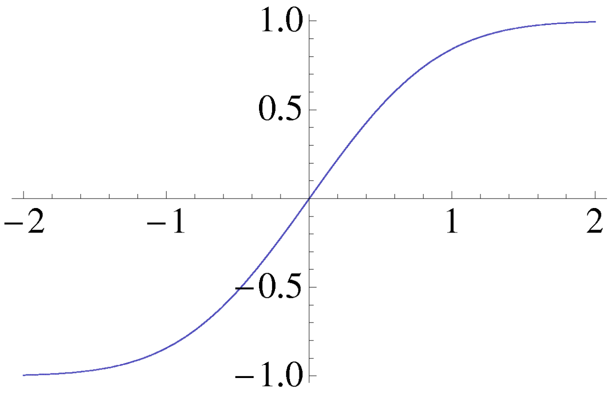

Figure 5.14: 2-D xz PDF of the migratory proton of UPA at 150 K modelled with a SN distribution.

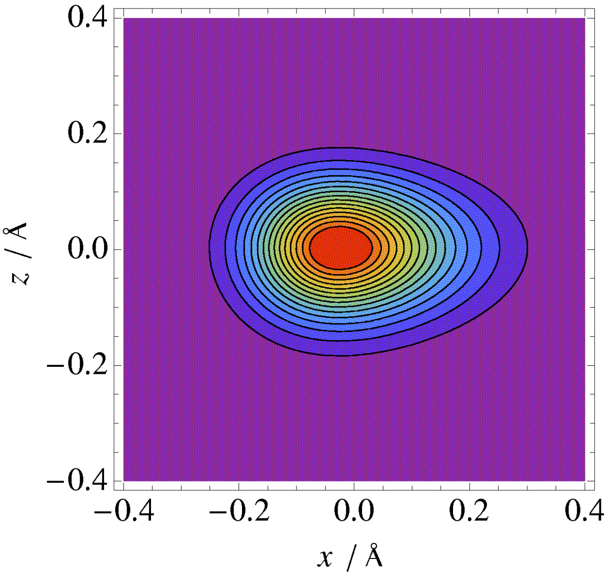

Equation 5.24 can be used to model the anharmonicity seen in the UPA migratory proton and the O atoms of nitromethane. At 150 K an agreement index of 27.5% is obtained in the case of the UPA H atom. The large value is a result of the high-frequency noise. A GC series with only the three H_{iii} polynomials gives essentially the same agreement factor. The full third-order GC series model (with ten polynomials) does give a better fit of 27.1% but all three refinements yield similar values for the probable position. The SN distribution successfully reproduces the egg shape of the xz distribution as shown in Figure 5.14.

For the O atom of nitromethane the agreement is not so good. A standard Gaussian model gives an R factor of 14.9%. The SN distribution gives a value of 14.3%, while the full third-order GC series gives a value of 12.8%. The SN model also gives a distribution that does not match the visual appearance of the numerical distribution very well. However, a GC series PDF with only the three H_{iii} terms produces very similar results to the SN distribution, suggesting that while the SN distribution is as effective as the GC series at skewing the distribution, the off-diagonal GC polynomials are important in this case at least. As well as skewing a harmonic distribution we could "bend" the shortest axis using the H_{iij} polynomials. The correction combination could produce the desired egg-shaped distribution. Whether the bending polynomials are important will probably depend on the profile of the distribution and the correlation between motion in different directions. Gradual asymmetry may be better approximated using skew functions only, whereas distributions that are more harmonic near the maximum may require the flexibility of the full GC series.

5.7 Combining the SN distribution with other PDFs

Despite its poor performance for the nitromethane O atom, the SN distribution may prove useful in crystallography where distributions are skewed. We could incorporate the error function into the parabolic PDF discussed in Section 5.5.2. Fitting the 228 K nitromethane D(2) atom PDF to a distribution of the form:

$$\begin{aligned} &P(\hat{\mathbf{u}}) \times (1 + \operatorname{erf}\left(\frac{a(x-u_1)}{\sqrt{2U_{11}}}\right) \\ &+c_{1111}H_{1111} + c_{111111}H_{111111} + c_{11111111}H_{11111111})\,, \end{aligned} \tag{5.28}$$

gives an R-factor of 15.9%. This is marginally better than the fit obtained with the PDF given by Equation 5.15. As the error function is contained within the GC series expansion it is still possible for the distribution to have negative regions. However, for systems with large amplitudes the error function may be more useful than the H_{iii} functions because it has a limited range, limiting its contribution to negative regions in the PDF. The probable C-D(2) bond length obtained using the probable position of this distribution is 1.081 Å, which is closer to the equilibrium value (1.089 Å) than the other two models discussed in Section 5.5.2.

In fact, the error function may represent a useful way to define a PDF based on polynomial perturbations that cannot have negative regions. We may define a PDF of the form:

$$P(\mathbf{u})_{\mathrm{SN}} = P(\mathbf{u})_{\mathrm{harm}}\left[1 + \operatorname{erf}\left(f\left(\mathbf{u}\right)\right)\right]. \tag{5.29}$$

where $f(\mathbf{u})$ is an appropriate polynomial function. If $f(-\mathbf{u}) = -f(\mathbf{u})$ then Eqaution 5.29 represents a true PDF[31] and therefore must have a characteristic function. The third-order Hermite polynomials satisfy this condition when centred on the mean position. At 15 K the D(1) atom of nitromethane required only three such polynomials to fit. If we let $f(\mathbf{u}) = c_{111}H_{111} + c_{112}H_{112} + c_{113}H_{113}$ then we obtain a R-factor of 14.4%, which is slightly better than the 14.6% obtained by using them directly (*i.e.* without using the error function). The anharmonic parts of the resulting PDF obtained using the two types of perturbation are plotted in Figure 5.15. This shows similar contours lines for both but with different scales.

Figure 5.15: 2-D xz anharmonic components of SN and GC fits to the D(1) atom PDF of nitromethane at 15 K.

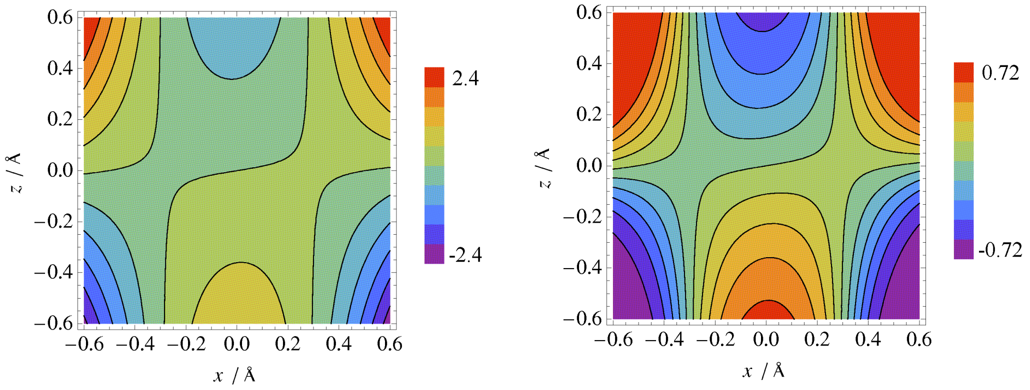

(a) $c_{111}H_{111} + c_{112}H_{112} + c_{113}H_{113}$

(b) $\mathrm{erf}(c_{111}H_{111} + c_{112}H_{112} + c_{113}H_{113})$

Further investigation is obviously required but a PDF of the form of Equation 5.29 may prove useful in crystallography, particularly at high temperatures where the negative probability density inherent to the GC series can be an issue. As the SN distribution represents a current field in statistics there exists the possibility for collaborations with statisticians to develop its application in crystallography.

5.8 Conclusion

The MD-derived numerical PDFs of a variety of atoms in different molecules have been modelled using a number of different analytical functions. In doing so the numerical datasets have shown their use in providing realistic models for understanding the nature and suitability of the various PDFs employed to model them.

The differences between the probable and equilibrium positions of atoms have been studied and the results suggest that in general the positions will be quite different. Encouragingly the bond lengths obtained using probable positions are far closer to the true equilibrium values than the time-average values. The difference between the true and refined values of the mean and variance of a PDF has also been investigated. For systems with strong anharmonicity the harmonic values deviate significantly from the true value evaluated numerically, suggesting that the physical meaning of the fitting parameters is not always assured. In addition, the simulations show large differences between the equilibrium and fitted probable positions of atoms in a number of molecules. This suggests that experimentally-determined probable positions will not give suitable estimates of equilibrium positions. However, further and wider study is required to make firm conclusions.

Two new forms of PDF have been fitted to the numerical PDFs. The first, based on a parabolic coordinate system, models the curvilinear motion of the protons in nitromethane and DMUOX as well as the GC series but with fewer parameters. Irrespective of whether the third-order GC series or parabolic PDF was used to model the curvature, it was essential to include fourth-order GC terms (primarily the H_{iiii} terms) to model the asymmetry of the PDF. To cut down on the number of GC parameters it has been suggested that the Hermite polynomials employed be defined in the harmonic thermal motion coordinate system.

A skew-normal PDF based on the univariate form introduced by Azzalini[29] has also been used to model anharmonic distributions. In this limited study it has been found to be as effective at skewing a PDF as the H_{iii} terms of the GC series but in some cases the flexibility of the full GC series permits it to model the data better. However, the SN distribution may provide a useful basis for a “true” PDF that can not feature negative regions - a significant drawback of existing methods at high temperatures.

Bibliography

[1] (*a*) C. C. Wilson, *Acta Cryst. B*, 2001, **57**, 435; (*b*) C. C. Wilson, K. Shankland and N. Chankland, *Z. Kristallogr.*, 2001, **216**, 303.

[2] (*a*) C. C. Wilson and C. A. Morrison, *Chem. Phys. Lett.*, 2002, **362**, 85; (*b*) C. A. Morrison, M. M. Siddick, P. J. Camp and C. C. Wilson, *J. Am. Chem. Soc.*, 2005, **127**, 4042.

[3] F. Fontaine-Vive, M. R. Johnson, J. Kearley, J. A. K. Howard and S. F. Parker, *J. Am. Chem. Soc.*, 2006, **128**, 2963.

[4] *CPMD, Version 3.13.2, IBM Corp. 1990-2008, MPI für Festkörperforschung, Stuttgart, 1997-2001.*, 2008.

[5] R. Car and M. Parrinello, *Phys. Rev. Lett.*, 1985, **55**, 2471.

[6] N. Troullier and J. L. Martins, *Phys. Rev. B*, 1991, **43**, 1993.

[7] J. P. Perdew, K. Burke and M. Ernzerhof, *Phys. Rev. Lett.*, 1996, **77**, 3865.

[8] G. Lippert, J. Hutter and M. Parrinello, *Mol. Phys.*, 1997, **92**, 477.

[9] C. R. Pulham, Personal communication, 2009.

[10] J. VandeVondele, M. Krack, F. Mohamed, M. Parrinello, T. Chassaing and J. Hutter, *Comp. Phys. Comm.*, 2005, **167**, 103.

[11] I. N. Levine, *Quantum Chemistry*, Prentice Hall, 5th edn., 2000.

[12] (*a*) S. Goedecker, M. Teter and J. Hutter, *Phys. Rev. B*, 1996, **54**, 1703; (*b*) C. Hartwigsen, S. Goedecker and J. Hutter, *Phys. Rev. B*, 1998, **58**, 3641.

[13] M. Krack, *Theor. Chem. Acc.*, 2005, **114**, 145.

[14] W. R. Inc., *Mathematica version 6.0*, location, 2007.

[15] C. Scheringer, *Acta Cryst. A*, 1986, **42**, 356.

[16] *International Tables for Crystallography*, ed. A. J. C. Wilson, Kluwer Academic Publishers, 1995, vol. C, p. 505.

[17] (*a*) C. Scheringer, *Acta Cryst. A*, 1987, **43**, 703; (*b*) C. Scheringer, *Acta Cryst. A*, 1987, **43**, 706.

[18] H. B. Bürgi and S. C. Capelli, *Acta Cryst. A*, 2000, **56**, 403.

[19] H. B. Bürgi, *Annu. Rev. Phys. Chem.*, 2000, **51**, 275.

[20] H. B. Bürgi, S. C. Capelli and H. Birkedal, *Acta Cryst. A*, 2000, **56**, 425.

[21] C. Giacovazzo, H. L. Monaco, G. Artioli, D. Viterbo, G. Ferraris, G. Gilli, G. Zanotti and M. Catti, *Fundamentals of Crystallography*, Oxford University Press, 2nd edn., 2002.

[22] W. F. Kuhs, *Acta Cryst. A*, 1992, **48**, 80.

[23] K. Tanaka and F. Marumo, *Acta Cryst. A*, 1983, **39**, 631.

[24] M. J. Kronenburg, *Acta. Cryst. A*, 2004, **60**, 250.

[25] C. K. Johnson, *Acta Cryst. A*, 1969, **25**, 187.

[26] K. R. McLean, Personal communication, 2007.

[27] C. Scheringer, *Acta Cryst. A*, 1988, **44**, 343.

[28] D. Hohlwein, *Acta Cryst. A*, 1981, **37**, 899.

[29] A. Azzalini, *Scand. J. Statist.*, 1985, **12**, 171.

[30] A. K. Gupta and J. T. Chen, *Ann. Inst. Statist. Math.*, 2004, **56**, 305.

[31] A. Azzalini, *Scand. J. Statist.*, 2005, **32**, 159.

Chapter 6

Further application of MD simulations to crystallography

6.1 Introduction

In the preceding three chapters, molecular dynamics (MD) simulations have been used to shed light on the nature of anharmonic thermal motion and its effect on crystal structure determination. The primary motivation for this work has been to provide useful data to enable the improvement of the formulae used in refinement programs, yielding more accurate and meaningful structures. The use of new or traditional anharmonic Debye-Waller factors is reliant on high-quality data that allows the extra parameters, compared to a harmonic model, to be refined.

Despite the many advances in X-ray and neutron sources and equipment, suitable high-quality data are not always available. Experiments at high pressure or temperature require experimental setups (such as diamond-anvil cells[1]) that can limit the amount of data collected substantially. At high temperatures the Debye-Waller factor has the effect of damping out diffraction at larger values of the scattering angle leading to fewer data. In these circumstances, the data can be so poor as to prohibit the refinement of even anisotropic displacement parameters (ADPs).

The refinement of ADPs for light atoms in single-crystal X-ray diffraction experiments can also be difficult due to the lack of scattering from these atoms. This can be a significant issue for charge-density studies where the asymmetry of the electron density is fitted as part of the refinement. The convolution of the electron density and vibrational probability density function (PDF) means that meaningful interpretation of the refined electron-density maps requires a good description of thermal motion. A variety of methods have been devised to estimate H-atom ADPs from heavy-atom values. The **TLS** method (Section 1.3.3), which assumes rigid motion of molecules, can be used to extrapolate heavy-atom ADPs to H atoms. More sophisticated schemes, including the **TLS**+ONIOM method,[2] combine the rigid **TLS** model with *ab initio* computed estimates of the contribution from internal degrees of freedom. The SHADE web server (http://shade.ki.ku.dk) can perform the requisite **TLS** analysis of an experimental refinement and provides empirical estimates of the contribution of non-rigid motions.[3]

The use of experimental information by way of the **TLS** method ensures that the SHADE web server and other methods give reasonable and sensible results. For systems where there are no heavy-atom ADPs then prediction of thermal parameters can only be achieved readily using lattice dynamics (LD) or MD simulations. Lattice dynamics[4,5] calculations can be performed in a variety of ways but the method in essence uses a series of static calculations of a perturbed system to determine its normal-mode eigenvectors and eigenvalues. Lattice dynamics has been used a number of times to compute ADPs for a number of different types of systems.[6,7] One of the main benefits of lattice dynamics is the direct inclusion of zero-point energy. It is also possible to include the effects of phonon dispersion using calculations at different parts of the Brillouin zone (Section 2.2.4). This incorporates phonon dispersion in a far more economical manner than the use of supercells as in an MD simulation. However, the principal disadvantage of LD calculations is that they are nearly always performed in the harmonic limit. At high temperatures, attempting to fit an anharmonic potential with a harmonic one may lead to spurious results (as is discussed in the following chapter for an equivalent situation in the gas phase). MD simulations have been used for a number of room or high-temperature studies. Recently, Glykos has used empirical-potential MD simulations to calculate ADPs for a small protein crystal structure.[8] The MD simulation predicted displacement parameters roughly a third of the experimental values. However, the theoretical information did prove useful in parametrising the refinement.

With recent advances in computational software and hardware, there has been renewed interest in using LD calculations to estimate ADPs.[9] As LD calculations are liable to be best suited to low-temperature nearly-harmonic systems, MD simulations should be complementary as they are best suited to high-temperature systems (for classical simulations) and can deal with any degree of anharmonicity. In the case of nitromethane (Chapter 4) the MD-derived displacement parameters were in very good agreement with experimental values and the ADPs calculated for ND_3 (Chapter 3) agreed very well with one of two very different descriptions of the thermal motion.

This chapter builds on the previous ones in this regard by using DFT-MD simulations to predict the ADPs of the crystal structure of benzophenone. The DFT simulations are complemented by experimental neutron diffraction data. While the experimental data are not of a sufficiently good quality for detailed analysis, comparison of the simulations with experimental refinements does show that the DFT-MD simulations perform reasonably and also highlights the impact of van der Waals dispersive forces on the ADPs.

6.2 Crystal structure of benzophenone

The solid-state structure of benzophenone ($C_{13}H_{10}O$) has been studied a number of times using X-ray diffraction and two phases or polymorphs are known in the literature, a stable form and a metastable form.[10–12] Indeed, benzophenone was the first organic compound reported to exhibit polymorphism. This present study focuses on the stable α phase, which crystallises in the orthorhombic $P2_12_12_1$ space group. No neutron diffraction structure of either phase has been reported before.

Benzophenone is a much more rigid system than the other molecules studied in the course of this work. The migratory proton of urea-phosphoric acid and the methyl group of nitromethane are examples of atoms/systems that will always show significant thermal motion effects. It is useful to study more rigid systems to assess how serious such effects will be for such molecules. In addition the solid-state interactions of benzophenone will be dominated by dispersion forces, which DFT traditionally models quite poorly. Therefore this study will allow us to investigate how serious the deficiency could be for DFT simulations and whether or not recently developed empirical corrections[13,14] to DFT can improve its modelling of organic solids.

6.2.1 Methods

Experimental

Single-crystal neutron diffraction data were collected on the SXD instrument at the ISIS spallation neutron source, Rutherford Appleton Laboratories, Oxfordshire, UK.[15] The SXD instrument uses the time-of-flight Laue diffraction method and is capable of capturing large amounts of reciprocal space with a stationary crystal due to the large area detectors used in the instrument.

Undeuterated crystals of benzophenone were grown by slow evaporation from hexane after Fleischer *et al.*[10] It was not possible to grow individual crystals of an appropriate size for neutron diffraction, so the multi-crystal method[16] was used with two colourless crystals approximately 1.0×3.0×0.5 mm in size. Data were collected with the assistance of Dr. A. Daoud-Aladine and Dr. D. A. Wann at temperatures of 70 and 300 K. Four crystal orientations were used at each temperature with data being collected for 11 hours in each orientation. The SXD-2001 program was used by Dr. M. J. Gutmann to index the unit cells and to reduce the raw data into a format suitable for refinement. Refinements were carried out using the SHELX97 code,[17] starting from coordinates from a previous X-ray structure of benzophenone.[11]

MD simulations

All of the DFT simulations of the crystal structure of benzophenone were carried out using the Gaussian and plane-wave formalism[18] using the CP2K code.[19] The generalised gradient corrected PBE functional was used together with the PBE-optimized double-ζ basis set provided with the code and a plane-wave density cut-off of 4250 eV. This cut-off energy ensured convergence of the atom forces and the total energy to within 2 meV/Å and 1 meV/atom respectively. For some simulations an empirical correction for van der Waals (vdW) dispersion was added. The vdW-corrected DFT calculations will be referred to as DFT+D calculations. The correction used the functional form of Elstner *et al.*[14] together with the PBE-optimised C_6 and R_0 parameters of Williams *et al.*[20]

Equilibrium geometries were determined for both the DFT and DFT+D levels of theory. As the CP2K program does not currently support symmetry constraints, a 2×2×2 supercell was optimised with $P1$ symmetry and the equilibrium geometry determined by averaging the optimised geometry using the $P2_12_12_1$ set of symmetry operations. The deviations between the symmetry-related positions were of the order of 1 fm, which is well within the error in an experimental structure.

Test simulations using 2×1×1 and 2×2×2 supercells showed that the larger cell would be necessary to obtain even reasonable agreement with preliminary experiment refinements. This may be a combination of a finite-size effect and lack of phonon dispersion. MD simulations were therefore carried out on 2×2×2 supercells both with and without the vdW-correction term. A chain of five Nose-Hoover thermostats[21] was used to maintain the temperature. The 2×2×2 cell contains 768 atoms. The linear scaling of the CP2K code makes MD simulations of such a system feasible.

In total, three production simulations were performed. Initial issues with the experimental data lead to two simulations being performed at 300 K using the previously reported 90 K cell vectors of Moncol and Coppens.[11] The DFT simulation was run for 9 ps, while the DFT+D simulation was run for 14 ps. Using the smaller cell vectors should have the effect of elevating the simulation pressure, which may affect the thermal motion and reduce the magnitude of the ADPs. However, in the empirical potential simulations of ammonia (Section 3.3.4) different pressures (in the range expected here) did not alter the ADPs by any significant amount. Finally, a 13 ps DFT+D simulation was performed at a temperature of 70 K using the cell vectors determined at that temperature as part of this work.

The trajectories were analysed using the same Fortran90 code and procedures as used for ND_3 (Chapter 3). The simulations were performed using the computational resources of the EPRSC National Service for Computational Chemistry (http://www.nsccs.ac.uk) and HECToR, the UK's national high-performance computing service, which is provided by UoE HPCx Ltd. at the

University of Edinburgh, Cray Inc. and NAG Ltd., and funded by the Office of Science and Technology through EPSRC's High End Computing Programme.

6.2.2 Effect of vdW correction

Table 6.1 gives some representative U_{eq} values calculated from the two MD simulations at 300 K, while Figure 6.1 shows the ellipsoids derived from the simulated ADPs. The DFT+D values are within 3–4 σ of the isotropically refined experimental values; this is much closer than the standard DFT simulation. The carbon- and hydrogen-atom parameters that define the vdW correction used in the DFT+D simulation were specifically fitted to modelling benzene and they seem to reproduce the experimental behaviour quite well. The total energy of the equilibrium DFT geometry is −3065.38 eV. The dispersion correction adds a further −2.60 eV. This is only 0.08% of the total energy of the DFT+D equilibrium structure but it makes a substantial difference to the dynamic behaviour of the system.

Minor differences between the computed and experimental U_{eq} values are to be expected, particularly because the experimental refinement models the thermal motion as being isotropic in nature. U_{eq} derived from experimental ADPs would be better for comparison but due to the quality of the data these can not be reliably determined (as will be discussed below in Section 6.2.3).

Table 6.1: Selected simulated (DFT and DFT+D) and experimental U_{eq} values (in Å^2) of benzophenone at 300 K. [See Figure 6.1(a) for atom numbering.]

	DFT[a]	DFT+D[a]	Expt.[b]
C(1)	0.0374(1)	0.0485(1)	0.055(2)
C(2)	0.0340(1)	0.0631(1)	0.065(2)
C(3)	0.0554(1)	0.0696(1)	0.079(2)
H(1)	0.0558(2)	0.0694(2)	0.081(4)
H(2)	0.0781(2)	0.0986(2)	0.099(4)
H(3)	0.0885(2)	0.1074(2)	0.104(5)
O	0.0679(2)	0.0786(2)	0.089(3)

[a] Calculated from the numerical ADPs as $U_{\mathrm{eq}} = \frac{1}{3}(U_{11} + U_{22} + U_{33})$

[b] Isotropic refinement. [See Table 6.5 (model I1) for more details.]

Figure 6.1: Simulated ADPs of benzophenone (50% probability level) at 300 K.

(a) DFT+D

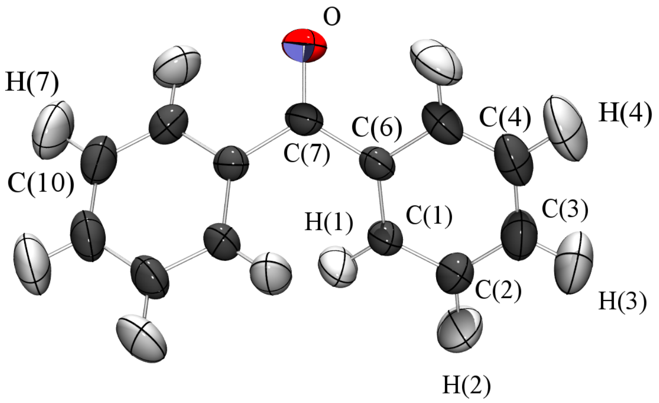

(b) DFT

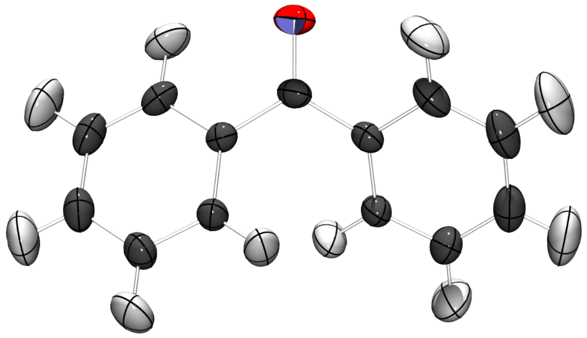

Benzophenone is, in principle, relatively rigid compared to systems like nitromethane, urea-phosphoric acid *etc.*, which have been discussed in previous chapters. The theoretical distance corrections ($\Delta r = r_{\mathrm{e,\,MD}} - r_{\mathrm{a,\,MD}}$) are likely to be reasonably small. Table 6.2 lists some of the corrections determined by the DFT and DFT+D simulations. The DFT+D corrections are typically larger, which makes sense in terms of the larger amplitudes that vibrations have in the DFT+D simulation. How significant these corrections are depends on the final uncertainties in the experimental time-averaged distances. The uncertainties would be expected to be reasonably large due to the temperature of the experiment and the small size of the crystals used. More accurate studies are of course possible and it is useful to have an idea of the magnitude of the effect of thermal motion on structures similar to benzophenone at this temperature.

Table 6.2: Theoretical distance corrections, $\Delta r = r_{\mathrm{e,\,MD}} - r_{\mathrm{a,\,MD}}$ (in Å), for a selection of bond lengths in benzophenone. [See Figure 6.1(a) for atom numbering.]

Distance	DFT	DFT+D
ΔrC(1)–C(2)	0.0082	0.0076
ΔrC(1)–H(1)	0.0113	0.0122
ΔrC(1)–C(6)	0.0090	0.0203
ΔrC(6)–C(7)	0.0036	0.0050
ΔrC(7)–O	0.0135	0.0179

6.2.3 Refinements

70 K

A number of different types of refinement have been carried out using the 70 K and 300 K datasets. The crystallographic data determined at those two temperatures are given in Table 6.3. Significantly more data were collected at 70 K compared to 300 K, which permits the use of ADPs without the need for restraints or constraints. Typically, the merit of a fit is assessed using three values:

$$R = \frac{\sum ||F_{\mathrm{o}}| - |F_{\mathrm{c}}||}{\sum |F_{\mathrm{c}}|}, \tag{6.1}$$

$$wR = \sqrt{\frac{\sum w \times (F_{\mathrm{o}}^2 - F_{\mathrm{c}}^2)^2}{\sum w \times (F_{\mathrm{o}}^2)^2}}, \tag{6.2}$$

$$S = \sqrt{\frac{\sum w \times (F_{\mathrm{o}}^2 - F_{\mathrm{c}}^2)^2}{n - p}}, \tag{6.3}$$

where F_{c} is the calculated value of the structure factor, F_{o} is the observed structure factor value, w is the statistical weight of a particular value of F_{o}, n is the number of reflections and p is the number of parameters. The R and wR values are the traditional measures of the merit of a fit and are based on refining against F or F^2, respectively. The value of R should normally be below 0.1 and that of wR below 0.25.[22] In the present case (and indeed most refinements) F^2 values are used as the overall merit of fit, although the R value is still quoted. The goodness of fit, S, is a measure of the validity of the model in a more statistical sense; S

should ideally be close to unity.[23] A statistical weighting scheme, $w = 1/\left(\sigma^2(F_o^2)\right)$, was used for all refinements discussed here. More sophisticated schemes can be employed to reduce statistical bias but they are more suited to X-ray datasets.[24] Such schemes typically aim to minimise the variance of the dataset and to make S as close to unity as possible. For multi-temperature data the use of a more complex weighting scheme can hinder quantitative comparison of the structures.

Data from different crystals and area detectors can be integrated/reduced separately. In this case two separate datasets were produced. As different scale factors can be refined for the two datasets, merging of Friedel pairs (values of $\mathbf{H}$ that when squared will produce the same value of F^2) was performed only for the final calculation of the R factor. The actual refinement uses all of the data. The quoted reflection-to-parameter ratio only includes the unique reflections.

Table 6.3: Crystallographic data at 70 and 300 K for benzophenone.

	70 K	300 K
Crystal system	orthorhombic	orthorhombic
Space group	$P2_12_12_1$	$P2_12_12_1$
a / Å	7.731(2)	7.988(2)
b / Å	10.253(2)	10.293(3)
c / Å	12.054(3)	12.138(4)
V / Å^3	955.5(4)	998.0(5)
Reflections collected[a]	6710	3057

[a] Total number of reflections before merging/omission of "bad" reflections.

An anisotropic refinement was carried out using the SHELX[17] program by Dr. M. J. Gutmann. The various parameters determined by the refinement are given in Table 6.4. The R and wR factors are close to the limits of acceptability. Lower values of wR and S could be obtained using fully-merged data but this does not affect the R factor significantly and would only hide inconsistencies in the data. At 70 K thermal motion should not affect this structure seriously so the high R and wR factors are disappointing. The large agreement factors may stem from the two crystals used in the sample having different responses to the cooling of the experimental apparatus from 300 K to 70 K. To obtain a stable fit, five of the collected reflections were omitted from the refinement.

Nevertheless, the structure determined is reasonable in appearance. The molecular structure with ellipsoids is shown in Figure 6.2 alongside the MD-derived structure. The theoretical H-atom ellipsoids are typically much smaller than the experimental values while the sizes of the C-atom ellipsoids are reasonably close to the experimental ellipsoids.

Table 6.4: Details of the anisotropic refinement of benzophenone at 70 K. (Distances are given in Å.)

$R[F^2 > 2\sigma(F^2)]$	0.1069
$wR(F^2)$	0.2211
S	4.830
Number of parameters (p)	219
Number of unique reflections used (n)	1532
Data to parameter ratio	6.9
$\max_{\Delta/\sigma}{}^{a}$	<0.0001
$\Delta\rho_{\max}$, $\Delta\rho_{\min}$ / e Å^3	4.36, −2.16
rC(1)–C(2)	1.383(5)
rC(1)–H(1)	1.107(10)
rC(1)–C(6)	1.393(5)
rC(6)–C(7)	1.502(6)
rC(7)–O	1.226(6)

[a] The maximum shift of any parameter divided by its uncertainty, which is a measure of the convergence of the refinement.

Figure 6.2: 70 K experimental and simulated ADPs of benzophenone (plotted at the 70% probability level).

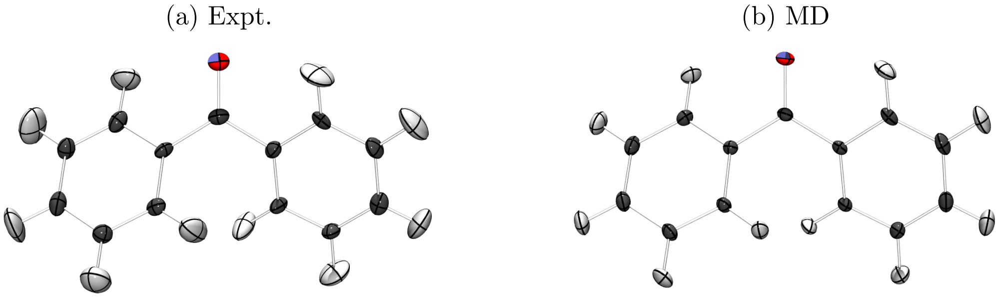
(a) Expt.

(b) MD

300 K

The 300 K data are very much inferior to the 70 K data in terms of the number of reflections. The number of parameters required for a full anisotropic refinement is 219, which gives a reflection-to-parameter ratio of 2.6. To obtain a refinement with a more reasonable ratio either a simpler model of thermal motion has to be adopted or some form of restraint or constraint must be introduced. Instead of an anisotropic refinement a single-parameter isotropic model could be used. Table 6.5 lists the various parameters and selected bond lengths obtained from a freely-refined isotropic model (labelled model I1). The wR and S values are actually smaller than for the anisotropic 70 K refinement, which is a further indication that something is awry with the 70 K data. The R value is large at 0.1331 and the C–H bond lengths vary substantially and some of them are far shorter than their DFT-calculated equilibrium values of ~ 1.09 Å. The DFT+D MD simulation, which gave reasonable U_{eq} values, suggests small distance corrections, so it is clear that the large variance in the C–H bond lengths is unphysical.

The poor quality of the refined structure is most likely a result of the small number of unique reflections, which in turn stems from the temperature of the experiment and the small size of the crystals used. It is possible that the use of a restrained or constrained refinement might improve matters. The SHELX program does not support the use of flexible restraints on positions and displacement parameters. Instead it allows for geometric restraints and restraints that ensure ADPs of bonded or close atoms are similar in a physically reasonable way. While individual coordinates and displacement parameters can not be restrained, they can be constrained. Model I2 in Table 6.5 represents an isotropic model in which the positions are freely refined but the value of U_{eq} for each atom is fixed at the number determined by the DFT+D MD simulation. The R factor is slightly smaller than in the I1 refinement but the wR and S values are slightly larger. However, the C–H bond lengths appear to be much more reasonable and the spread is much smaller. The heavy-atom distances are not really affected.

Despite the poor quality of the data, the use of the DFT+D U_{eq} values does appear to produce a more reasonable model of the structure. The use of the MD-derived ADPs might improve the picture further. Refinement A1 (in Table 6.5) is the free anisotropic refinement at 300 K, while A2 is the refinement with the ADPs constrained to the DFT+D values. The various agreement factors are

Table 6.5: Details of the refinements of benzophenone at 300 K.

	I1	I2	A1	A2
$R[F^2 > 2\sigma(F^2)]$	0.1331	0.1309	0.0974	0.1037
$wR(F^2)$	0.1636	0.1729	0.1382	0.1533
S	3.456	3.638	2.982	3.227
p	99	75	219	75
n	575	575	575	575
$n : p$	5.8	7.7	2.6	7.7
$\max_{\Delta/\sigma}$	<0.0001	<0.0001	<0.0001	<0.0001
$\Delta\rho_{\max}$, $\Delta\rho_{\min}$ / e Å^3	1.02, −1.05	1.06, −0.95	0.56, −0.37	0.53, −0.50
rC(1)–C(2)	1.403(7)	1.392(7)	1.387(8)	1.368(6)
rC(1)–C(6)	1.383(7)	1.379(7)	1.382(8)	1.382(6)
rC(6)–C(7)	1.484(7)	1.490(7)	1.485(9)	1.490(7)
rC(7)–O	1.262(8)	1.254(8)	1.224(8)	1.211(6)
rC(1)–H(1)	1.077(17)	1.118(16)	1.092(19)	1.149(13)
rC(4)–H(4)	1.018(21)	1.077(21)	1.121(24)	1.140(15)
rC(10)–H(7)	1.033(23)	1.068(20)	0.990(26)	1.130(16)

naturally smaller for the A1 refinement compared to I1 and I2 but the model has too many parameters freely refining and features a number of artefacts including some very short C–H bonds [*e.g.* rC(10)–H(7) = 0.990(26) Å]. The constrained model, A2, yields a better fit than I1 and I2 and also produces a more consistent structure than A1, with slightly smaller uncertainties. The C–H bond lengths are longer than would be expected but are within error of the likely values at 300 K.

It would be preferable to use the MD data to restrain the refinements as opposed to constraining them. In gas electron diffraction studies it is common for theoretical/computed data to be used for this purpose, using methods such as SARACEN.[25] In the case of the A2 model the constrained data produce C–H bond lengths that are consistent but too long. If the MD data could be used to restrain/constrain the shape of an ellipsoid but not its size then better agreement should be possible. Alternatively the orientation might be restrained, while the size is constrained. There are many possible ways that the data could be used to supplement the experimental refinement. The CRYSTALS[26] program does support such flexible restraints but the process of inputting them is cumbersome and more suited to geometrical restraints.

6.3 Conclusion

The structure of the stable α phase of benzophenone has been studied using DFT-MD simulations and multi-crystal neutron diffraction at 70 and 300 K. The DFT simulations were performed with and without an empirical correction for van der Waals forces. These forces represent long-range correlations of the electron density, which are poorly modelled by most mainstream functionals. The dispersion correction significantly improves the agreement between the MD-derived displacement parameters and U_{eq} values from an isotropic refinement of the experimental data at 300 K.

There are insufficient data at 300 K to obtain an acceptable anisotropic refinement at 300 K. However, the use of the MD-derived ADPs/U_{eq} in constrained isotropic and anisotropic refinements improves the structural consistency of the refinements and does not adversely affect the various agreement factors that much. The use of MD-derived data as flexible restraints on ADPs would probably improve matters further.

At 70 K an anisotropic refinement is possible and yields a reasonable structure. However, the large agreement factors suggest some issue with the experimental data, possibly as a result of the cooling of the two crystals used in this multi-crystal experiment.

While the poor quality of the experimental data impacts upon the importance of this study, it is clear from this and the previous simulations of nitromethane and ammonia that MD simulations are capable of providing reasonable estimates of ADPs.

Bibliography

[1] L. Merrill and W. A. Bassett, *Rev. Sci. Instrum.*, 1974, **45**, 290.

[2] A. E. Whitten and M. A. Spackman, *Acta Cryst. B*, 2006, **62**, 875.

[3] A. Ø. Madsen, *J. Appl. Cryst.*, 2006, **39**, 757.

[4] M. T. Dove, *Introduction to Lattice Dynamics*, Oxford University Press, 2005.

[5] S. Baroni, S. de Grioncoli and A. Dal Corso, *Rev. Mod. Phys.*, 2001, **73**, 515.

[6] A. Criado, A. Conde and R. Márquez, *Acta Cryst. A*, 1984, **40**, 696.

[7] T. Pilati, F. Demartin and C. M. Gramaccioli, *Phys. Chem. Minerals*, 1998, **26**, 149.

[8] N. M. Glykos, *Acta Cryst. D*, 2007, **63**, 705.

[9] A. Ø. Madsen, B. Civalleri, F. Pascale, R. Dovesi and S. Larsen, *Acta Cryst. A*, 2008, **64**, C148.

[10] E. B. Fleischer, N. Sung and S. Hawkinson, *J. Phys. Chem.*, 1968, **72**, 4311.

[11] J. Moncol and P. Coppens, Private communication to the Cambridge Structural Database, deposition number CCDC 245188.

[12] H. Kutzke, H. Klapper, R. B. Hammond and K. J. Roberts, *Acta Cryst. B*, 2000, **56**, 486.

[13] S. J. Grimme, *J. Comput. Chem.*, 2004, **25**, 1463.

[14] M. Elstner, P. Hobza, T. Frauenheim, S. Suhai and E. Kaxiras, *J. Chem. Phys.*, 2001, **114**, 5149.

[15] D. A. Keen, M. J. Gutmann and C. C. Wilson, *J. Appl. Cryst.*, 2006, **39**, 714.

[16] C. C. Wilson, *J. Appl. Cryst.*, 1997, **30**, 184.

[17] G. M. Sheldrick, *Acta Cryst. A*, 1990, **46**, 467.

[18] G. Lippert, J. Hutter and M. Parrinello, *Mol. Phys.*, 1997, **92**, 477.

[19] J. VandeVondele, M. Krack, F. Mohamed, M. Parrinello, T. Chassaing and J. Hutter, *Comp. Phys. Comm.*, 2005, **167**, 103.

[20] R. W. Williams and D. Malhotra, *Chem. Phys.*, 2006, **327**, 54.

[21] (*a*) S. Nosé, *J. Chem. Phys.*, 1984, **81**, 511; (*b*) W. G. Hoover, *Phys. Rev. A*, 1985, **31**, 1695.

[22] C. Giacovazzo, H. L. Monaco, G. Artioli, D. Viterbo, G. Ferraris, G. Gilli, G. Zanotti and M. Catti, *Fundamentals of Crystallography*, Oxford University Press, 2nd edn., 2002.

[23] (*a*) D. Schwarzenbach, S. C. Abrahams, H. D. Flack, W. Gonschorek, T. Hahn, K. Huml, R. E. Marsh, E. Prince, B. E. Robertson, J. S. Rollett and A. J. C. Wilson, *Acta Cryst. A*, 1989, **45**, 63; (*b*) D. Schwarzenbach, S. C. Abrahams, H. D. Flack, E. Prince and A. J. C. Wilson, *Acta Cryst. A*, 1995, **51**, 565.

[24] M. J. Gutmann, Personal communication, 2009.

[25] (*a*) A. J. Blake, P. T. Brain, H. McNab, J. Miller, C. A. Morrison, S. Parsons, D. W. H. Rankin, H. E. Robertson and B. A. Smart, *J. Phys. Chem.*, 1996, **100**, 12280; (*b*) P. T. Brain, C. A. Morrison, S. Parsons and D. W. H. Rankin, *J. Chem. Soc., Dalton Trans.*, 1995, 4589; (*c*) N. W. Mitzel and D. W. H. Rankin, *Dalton Trans.*, 2003, 3650.

[26] P. W. Betteridge, J. R. Carruthers, R. I. Cooper, K. Prout and D. J. Watkin, *J. Appl. Cryst.*, 2003, **36**, 1487.

Chapter 7

Experimental equilibrium structures in the gas phase: silsesquioxanes

7.1 Introduction

Polyhedral oligomeric silsesquioxanes (POSS) are a class of molecules with the general formula $(\mathrm{SiO}_{1.5})_n$ where $n = 4, 6, 8, 10, 12...$, which have attracted a considerable amount of interest in the literature. They are highly functional, nano-sized molecules, with a number of applications including additives for paints and resins, polymers and chemical-vapour deposition coatings. The chemistry of a wide selection of POSS molecules and details of more applications is provided in a review by Lickiss and Rataboul.[1]

The interest in the properties of silsesquioxanes has naturally lead to a large number of structural studies being performed on these molecules. In particular the eight-membered (in terms of silicon atoms) and ten-membered variants, $\mathrm{Si_8O_{12}R_8}$ and $\mathrm{Si_{10}O_{15}R_{10}}$, have been studied a number of times using computational and experimental methods. $\mathrm{Si_8O_{12}H_8}$ was the first POSS molecule to be studied and was characterised using X-ray diffraction.[2] Since then studies have been performed on a number of different molecules using X-ray[3–5] and neutron diffraction[6] on crystals as well using NMR and infra-red (IR) spectroscopy in solution.[7]

Recent work in the Rankin research group has focused on elucidating the experimental gas-phase structures of a series of POSS molecules. The technique used to perform these gas-phase studies will be outlined in the following section, while a discussion of the gas-phase and solid-state structures of some of these molecules will be give in Sections 7.3 and 7.4. A gas-phase study of these molecules is important because many of the solid-state structures feature deformations from the highest possible molecular symmetry. In the gas phase the molecules can be studied in the absence of packing effects, so independent molecular features of the molecules can be probed. This should in turn help us to understand lattice effects.

7.2 Gas electron diffraction

Structures in the gas phase can be studied by a number of techniques. These include spectroscopic methods such as IR and microwave spectroscopy and also gas-phase electron diffraction (GED). Of these methods, GED is the most versatile and widely used method for total structure determination in the gas phase. Microwave methods rely on molecules having a dipole moment and are only applicable to relatively small molecules.

Electrons are used for diffraction in the gas phase because they give higher diffraction intensities than X-rays or neutrons (*cf.* the electron form factor given by Equation 1.11).[8] This permits shorter experiments and smaller samples. A typical GED experiment involves heating a solid or liquid sample of the compound of interest to produce vapour, which is then passed in front of a beam of electrons resulting in diffraction.[9] The rotational disorder of the gaseous molecules leads to a pattern of concentric rings being generated on the detector, which can be photographic film, image plates or a CCD camera. The circular pattern is averaged to produce a 1-D scattering curve. The diffraction pattern arises due to interactions of the electrons with one, two or more atoms at a time. From a structural point of view, the two-atom scattering is of most use as it tells us about each of the interatomic distances in the molecule. Once the atomic and background scattering have been removed we have a molecular scattering curve, which when Fourier transformed yields a radial distribution curve (RDC), which shows the probability of finding a given distance in the molecule; see Figure 7.1 for an example. As in the case of solid-state diffraction, vibrations play an important role in the GED technique. The root-mean squared amplitude of vibration, u, is the GED equivalent of the anisotropic displacement parameters. In the harmonic approximation, each peak in the RDC corresponds to a Gaussian distribution (with variance u^2) for each type of interatomic distance.

The nature of the 1-D data collected in a GED experiment makes it very difficult to refine structures directly from the experimental data. One of the primary reasons for this is the overlapping of peaks in the RDC. As can be seen in

Figure 7.1: RDC of 1,3,5-trichlorotriazine ($C_3N_3Cl_3$). Each of the vertical "sticks" represents a distance and its relative intensity (but not multiplicity).

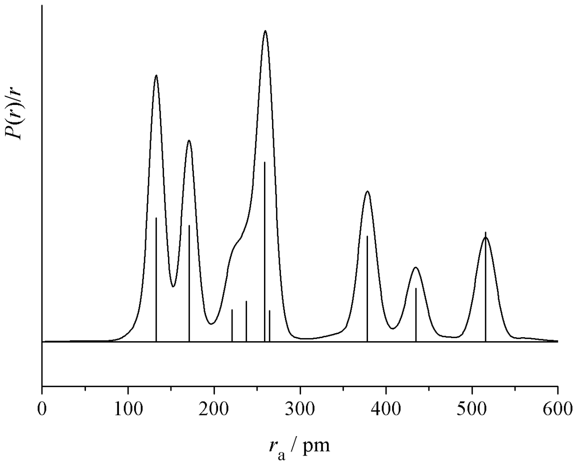

Figure 7.1 the third to sixth smallest interatomic distances are so close that they produce what appears to be only two peaks that overlap each other. The more distances there are under a given peak the harder it is to refine them without serious correlations or artefacts in the refinement. Other issues involve the number of parameters required to model a structure and also the small scattering factor of light atoms such as hydrogen.

A variety of methods have been developed to overcome these issues and it is now possible to determine the structures of molecules with $\sim$ 100 atoms successfully. Data from complimentary techniques such as microwave spectroscopy or liquid-crystal NMR can be used to supplement the GED dataset. However, it is more routine to use theoretical data. The SARACEN method[10] incorporates theoretical data into the refinement by using the computed values as initial guesses and also to decide restraints for various parameters and amplitudes of vibration.

As stated above, GED experiments are subject to vibrational effects just like solid-state diffraction. The distance determined by the GED molecular scattering function is a time-averaged one, referred to as r_a. The traditional scattering equation is formulated in such a way that this distance is not the direct average of the interatomic distance:

$$r_{\mathrm{a}} = \langle r^{-1} \rangle^{-1}. \tag{7.1}$$

To allow for anharmonicity in the thermal motion, the scattering equation also incorporates a term that models the effective interatomic potential as being Morse-like in nature.[11] A more general scattering equation that can model any degree of anharmonicity, using a polynomial expansion, has also been developed.[12]

7.2.1 Equilibrium structures in the gas phase

There has been considerable interest in correcting experimental GED structures to obtain structures more suited for comparison with theory. This is especially important in the gas phase because more accurate computational techniques such as hybrid DFT, MP2 and the various CI methods are less computationally demanding in the gas phase. Initial attempts at correcting for thermal motion effects used either experimental or theoretical "force fields" (*i.e.* dynamical matrix or Hessian) to estimate distance corrections.[11,13] These corrections assumed that the atoms moved in a particular fashion relative to each other. For example the r_{h0} distance/structure is obtained by modelling the atoms as moving harmonically along straight lines. The r_{h1} structure assumes that the motion is harmonic but along parabolic paths. These types of corrections can be calculated from a theoretical force field by the SHRINK program.[14]

More recently it has become common to calculate cubic force fields to allow for the effects of anharmonic motion of the atoms.[15] This approach, which yields $r_{\mathrm{a3,\,1}}$ distances, is well suited to systems for which a cubic potential is an appropriate model for thermal motion. However, for very anharmonic motion, where fourth-order and higher terms may be important, the cubic force field can give spurious results. The EXPRESS method was developed recently by McCaffrey *et al.*[16] as a general method capable of modelling any degree of anharmonicity. It uses a series of *ab initio* or DFT calculations along the normal modes of the molecule to map the potential-energy surface and calculate the r_{a}. The method has been successfully applied to NaCl, which forms a mixture of monomers and diamondlike dimers in the gas phase. However, it is a very labour intensive approach to the problem and also relies on the assumption that only simple coupling of the normal mode motions occur.

7.2.2 Equilibrium structure of 1,3,5-chlorotriazine determined using molecular dynamics simulations

As we have seen in Chapters 3–6, MD simulations provide a useful and generic way to determine the differences between equilibrium and time-averaged structures. Dr. P. McCaffrey first applied this type of approach to the gas-phase structure of octahydridosilsesquioxane, $Si_8O_{12}H_8$.[17] This molecule will be discussed below in Section 7.3 with other silsesquioxanes that have been studied using GED. The method will be outlined here using a more detailed benchmark of the method, the structure of 1,3,5-trichlorotriazine. This compound, shown in Figure 7.2, is small and rigid and should not feature any particularly large-amplitude anharmonic vibrations. Therefore, both the MD and traditional methods should give reasonable and comparable results.

Figure 7.2: Structure of 1,3,5-chlorotriazine.

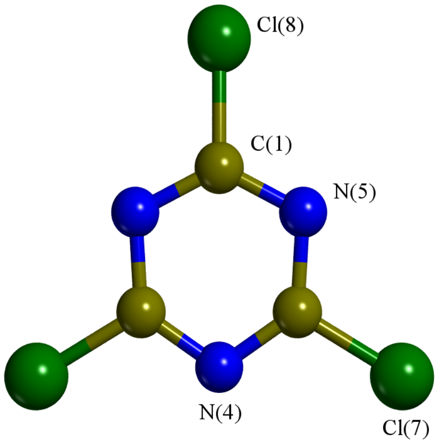

Computational details

Gaussian basis set calculations of $C_3N_3Cl_3$ were performed by Dr. D. A. Wann (University of Edinburgh) using the Gaussian03 program,[18] with the computational resources of the EPRSC National Service for Computational Chemistry (http://www.nsccs.ac.uk). Calculations were performed at a variety of levels of theory up to MP2[19] and B3LYP,[20] with basis sets including 6–31G(d) and 6–311+G(d). A cubic-frequency calculation was performed at the B3LYP/6–311+G(d) level of theory to determine the RMS amplitudes of vibration and distance corrections required for an $r_{\mathrm{a}3,1}$-type refinement.[16]

Plane-wave DFT calculations were performed using the CPMD code.[21] To simulate an isolated molecule in the gas phase using a periodic code such as CPMD, a supercell of 14 Å length was used together with a Tuckerman-Poisson solver,[22] to limit electrostatic interactions between periodic images of the molecule. The PBE functional,[23] Troullier-Martins norm-conserving pseudopotentials[24] and a plane-wave cut-off energy of 1250 eV were used. After a geometry optimisation a classical NVT simulation was performed at 398 K (the average experimental temperature), with the temperature being regulated by a "massive" chain of Nosé-Hoover thermostats for the ions. The system was evolved using the usual Car-Parinello method with a time step of 0.0725 fs for a total of 41 ps. Data were collected every 5 CPMD steps.

A path-integral (PI) MD simulation of $C_3N_3Cl_3$ was also performed using the CPMD program. The basic simulation and system parameters (cut-off, *etc.*) were the same as for the classical DFT simulation. A Trotter dimension (bead number) of 16 was used. The standard normal-mode transformation approach[25] was used to propagate the equations of motions of the PI beads. The simulation was run for a total of 20 ps. The shorter simulation time, compared to the classical simulation, is justified as the PI beads are equivalent to each other so the trajectory is effectively collecting 16 times the data of the classical simulation.

Trajectory analysis

The time-averaged distance between two atoms i and j, $r_{\mathrm{a},ij}$, determined by a GED experiment can be calculated from a trajectory as:

$$r_{\mathrm{a},ij} = \left(\frac{1}{N} \sum_{n=1}^{N} (r_{ij,n})^{-1} \right)^{-1}, \tag{7.2}$$

where N is the total number of steps being averaged over. If symmetry results in different distances being symmetrically equivalent then these can be averaged over as well. The RMS amplitude of vibration is given by:

$$u_{ij} = \sqrt{\frac{1}{N} \sum_{n=1}^{N} (r_{ij,n} - \langle r_{ij,m} \rangle)^2}, \tag{7.3}$$

where $r_{ij,m}$ is the direct mean interatomic separation:

$$r_{ij,m} = \frac{1}{N} \sum_{n=1}^{N} r_{ij,n}. \tag{7.4}$$

The uncertainties in these quantities can be estimated from the Central limit theorem as discussed in Chapter 3.[26] The analysis of the PIMD simulations was performed using the above equations and considering each replica of the system in turn so that for a P bead simulation, P times as many distances were used for the calculations in Equations 7.2 and 7.3.

It is also possible to estimate the Morse constants to allow for asymmetry in the probability density function (PDF) that describes the vibrational distribution of each interatomic distance. The instantaneous interatomic distances adopted by an atom pair can be easily "binned" during the course of the simulation to determine a histogram of atomic distances. Normalisation of this histogram produces a probability density function, $P(r)$ for each pair of atoms. The Boltzmann equation relates this function to the effective interatomic potential $V(r)$ such that:

$$P(r) = \frac{1}{Z} \exp\left(\frac{-V(r)}{k_{\mathrm{b}}T} \right), \tag{7.5}$$

where k_b is the Boltzmann constant and Z is the partition function. The potential can be obtained from

$$V(r) = -k_\mathrm{b}T\left(\ln[P(r)] - \ln[P(r_\mathrm{e})]\right). \tag{7.6}$$

The subtraction of $\ln[P(r_\mathrm{e})]$ gives $V(r_\mathrm{e}) = 0$ and eliminates the partition function, Z, from Equation 7.6. The numerical potential can then be fitted to a Morse potential to extract the desired value.

A program called MDSIM was written by Dr. A. V. Zakharov (Ivanovo State University of Chemistry and Technology), during a visit to the University of Edinburgh, which performs the trajectory analysis outlined in this section. In addition, it provides suitable input files for the ed@ed refinement program.[27]

RMS amplitudes of vibration, distance corrections and Morse constants

The MD-derived distance corrections and amplitudes of vibration are given in Table 7.1, along with the cubic force-field values. A PIMD simulation was performed because it is likely that the inclusion of zero-point energy will be important for some vibrational modes. This is clearly evident in the amplitudes and distance corrections for the classical and PI simulations. In all but one case the amplitude of vibration is found to be larger in the PIMD simulation. The distance corrections are also correspondingly different. The agreement between the PIMD and force-field amplitudes is very good and the distance corrections are nearly identical.

The classical-MD and PIMD Morse parameters disagree substantially. The classical values for the bonded distances agree reasonably with the tabulated values of Kuchitsu *et al.*[28] The non-bonded values are quite small apart from N(4)$\cdots$N(5) and N(4)$\cdots$Cl(4). The latter at least will have some bonding character as the Cl is directly opposite that N in the structure. In contrast, the PIMD non-bonded values are larger, while the bonded values are much smaller than would be expected. This is most likely an artefact of the manner in which

Table 7.1: RMS amplitudes of vibration, u, distance corrections, $r_a - r_e$, and Morse constants, a, determined from the DFT-MD simulations and the cubic frequency calculation of $C_3N_3Cl_3$.[a]

	DFT-MD ($P = 1$)			DFT-PIMD ($P = 16$)			Cubic freq. calc.[b]		
Atom pair	u	$r_a - r_e$	a	u	$r_a - r_e$	a	u_{h1}	$r_a - r_{a3,1}$	a[c]
C(1)–N(5)	3.1(1)	0.4	21.7	4.6(1)	0.6	10.0	4.5	0.6	22.7
C(1)–Cl(8)	4.3(1)	0.8	21.5	5.2(1)	0.9	11.2	4.8	0.8	18.3
C(1)···Cl(8)	4.0(1)	0.2	0.4	5.3(1)	0.7	4.2	5.2	0.6	0.0
N(4)···N(5)	4.5(1)	0.3	10.3	5.6(1)	0.8	5.3	5.3	0.8	0.0
N(4)···Cl(7)	5.9(1)	0.8	9.5	6.6(1)	1.1	6.1	6.2	1.0	0.0
C(1)···N(4)	5.1(1)	0.8	2.1	6.2(1)	0.7	4.4	5.9	0.7	0.0
C(1)···Cl(7)	5.9(1)	0.3	2.9	6.5(1)	0.9	8.2	6.2	0.8	0.0
N(1)···Cl(8)	6.2(1)	−0.1	1.3	6.8(1)	0.7	2.4	6.3	0.7	0.0
Cl(7)···Cl(8)	8.6(1)	0.1	0.0	8.5(1)	0.8	4.7	8.4	0.8	0.0

[a] Distances and amplitudes are in pm, while Morse constants are in nm^{-1}.

[b] B3LYP/6–311+G(d) level of theory.

[c] Tabulated values of Kuchitsu *et al.*[28] The values are for diatomic species and therefore do not include non-bonded distances.

the trajectory is analysed. While treating each replica molecule individually gives acceptable amplitudes and corrections, it appears to produce spurious Morse constants. This is supported by calculations on 1,3,5-trazine ($C_3N_3H_3$).[29] Morse parameters are rarely used for anything other than bonded distances, where a Morse potential is likely to be physically reasonable. If they are necessary, then values from a classical MD simulation should be used until an appropriate way of estimating them properly from a PIMD simulation is found.

Otherwise, the close agreement of the PIMD values with the cubic force-field values shows that MD simulations are capable of reproducing *ab initio* results. This provides a strong validation for their application to more complex systems. It is not feasible to perform PIMD simulations for all molecules but the majority of systems that this method will be applied to will have low-frequency high-amplitude vibrations that are far better approximated by classical dynamics. Distances between bonded atoms or atoms separated by only one or two atoms will still be poorly represented as they will have significant contributions from high-frequency stretches and bends but the force-field approach should give suitable values for those distances. It is for longer interatomic distances, with large amplitudes, that MD simulations will be most important and suitable.

Equilibrium structure

The *ab initio* and DFT calculations confirmed the natural assumption of $D_{3\mathrm{h}}$ symmetry. The GED refinement was carried out by Dr. D. A. Wann using the ed@ed program and a model of the molecule with $D_{3\mathrm{h}}$ symmetry, defined by the parameters, rC–Cl, rC–N and ∠N–C–N. Details of the data extraction and refinement are given elsewhere;[29] the final geometric parameters (r_e), determined using the DFT-PIMD simulation results, were rC–Cl = 1.7024(9) Å, rC–N = 1.3214(6) Å and ∠N–C–N = 127.04(9)°.

7.3 Gas-phase structures of silsesquioxanes

The MD method outlined in the previous section has been successfully applied to the structures of four silsesquioxanes. These are $Si_8O_{12}H_8$, $Si_8O_{12}Me_8$, $Si_{10}O_{15}H_{10}$ and $Si_6O_9(OSiMe_3)_6$ (where Me = methyl). Figure 7.3 shows the molecular structure of each molecule. As the details of the experiments and refinements are either published or due to be published,[30–32] for brevity only the features of the structures that are of interest will be discussed here. The MD simulations of $Si_8O_{12}H_8$ were performed by Dr. P. D. McCaffrey, while some of the simulations of $Si_6O_9(OSiMe_3)_6$ were performed by Mr. C. Jackson, a B.Sc. project student. The remaining simulations were carried out in the course of this work.

7.3.1 $Si_8O_{12}H_8$ and $Si_8O_{12}Me_8$

The first two silsesquioxanes studied were the octahydrido and octamethyl compounds. Both compounds feature a cube-like structure with the Si atoms at the corners joined by O atoms and possess overall O_h symmetry. In the case of $Si_8O_{12}H_8$ the classical DFT-MD simulations gave amplitudes of vibration that were too small. Instead of using all of the MD-derived values, the distance corrections were taken from the MD simulation while the amplitudes of vibration were taken from the *ab initio* frequency calculation. This refinement and an all *ab initio* refinement were essentially the same. In contrast, attempts to use the force

Figure 7.3: Structures of four POSS molecules studied using GED.

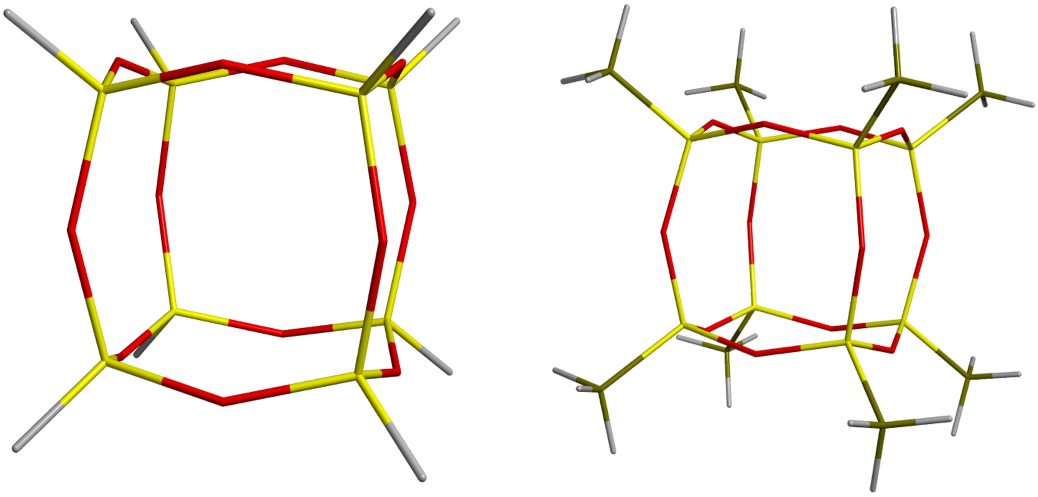

(a) $Si_8O_{12}H_8$

(b) $Si_8O_{12}H_8$

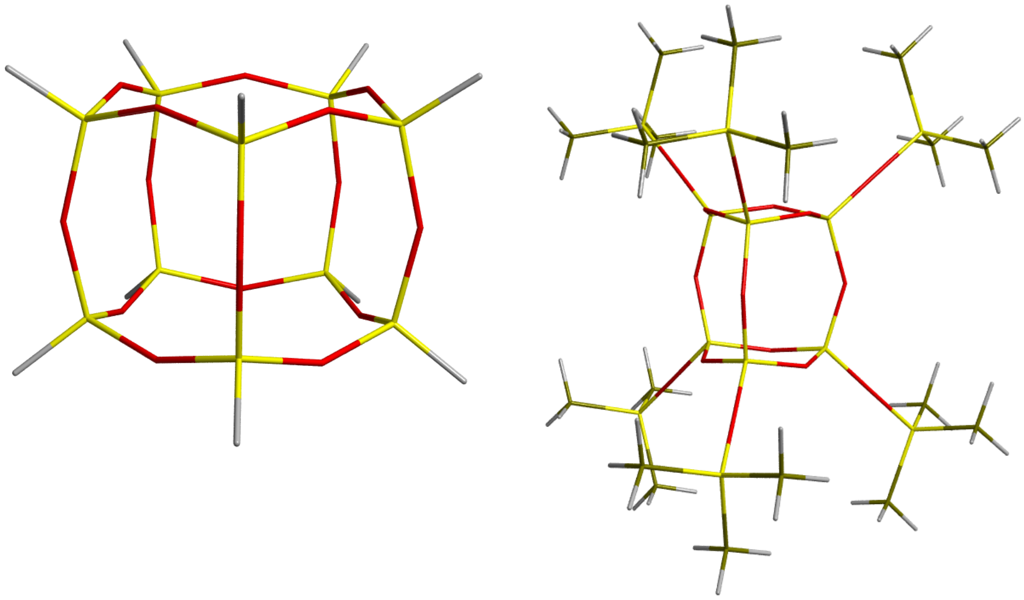

(c) $Si_{10}O_{15}H_{10}$

(d) $Si_6O_9(OSiMe_3)_6$

field amplitudes and distance corrections for $Si_8O_{12}Me_8$ failed. The presence of the methyl groups altered the dynamics of the cage to the extent that harmonic or cubic potentials were no longer suitable. In addition the H atoms of the methyl groups rotate freely. Such motion is also poorly modelled by second- or third-order polynomials. The MD-derived values permitted an acceptable refinement of the equilibrium structure. Quantum effects were not a serious issue because of the slightly higher temperature of the experiment (490 K *versus* 400 K for $Si_8O_{12}H_8$) and the low frequencies of the dominant anharmonic vibrations.

The most interesting structural feature of these two molecules is not contained in the absolute parameters but in the $r_\mathrm{a} - r_\mathrm{e}$ distance corrections. Nearly all of the non-bonded distance corrections are negative, indicating that the effect of thermal motion is to contract the silsesquioxane molecule. However, the effect is relatively small, with the diagonal Si$\cdots$Si distance being 0.015 Å shorter in $\mathrm{Si_8O_{12}H_8}$ and 0.025 Å shorter in $\mathrm{Si_8O_{12}Me_8}$ compared to the equilibrium values. While the Si$\cdots$Si distance corrections are small, distance corrections to O atoms are larger. The across-face O$\cdots$O distance in $\mathrm{Si_8O_{12}H_8}$ is 0.046 Å shorter while the corresponding O$\cdots$O distance in $\mathrm{Si_8O_{12}Me_8}$ is 0.056 Å shorter. The shortening most likely arises from anharmonic motions of the O atoms transverse to the direction of Si linkage. In this case the pairs of O atoms can be thought of as vibrating towards and away from each other. They spend more time moving towards each other from their equilibrium position, pulling the Si atoms and shrinking the cage. Studies of $\mathrm{Si_8O_{12}H_8}$ and other silsesquioxanes in the solid state[3,4] have shown that this motion arises from rigid motions of the $\mathrm{SiHO_3}$ "tetrahedra" relative to each other. This leaves the strong O–Si–O linkages intact, with the result being that the corresponding motions have very low vibrational frequencies. The motions of $\mathrm{SiO_4}$ tetrahedra in zeolites and silicates are also very soft and the cooperative motions of these tetrahedra has been shown to have an important role in the structural and phase behaviour of some materials.[33] Such low-frequency cooperative vibrations are referred to as rigid unit modes.

The analysis of such vibrations is complicated by the obviously large degree of anharmonicity but it is still useful to study the harmonic frequencies and eigenvectors obtained using the *ab initio* calculations. Figure 7.4 shows the eigenvectors of the 29 $\mathrm{cm^{-1}}$ vibration of $\mathrm{Si_8O_{12}Me_8}$, obtained at the B3LYP/6–31G* level of theory. This $T_{2\mathrm{u}}$ symmetry mode is the second-lowest frequency vibration in the structure and it is clear that it and similar vibrations are responsible for the across-face motions of the O atoms. The vectors show that the motions of the O atoms relative to one another preserves the strong O–Si–O linkages. Bieniok and Bürgi[4] performed principal component analysis (PCA) of the deformations of solid-state $\mathrm{Si_8O_{12}}$ fragments, finding that the deformations from ideal symmetry were a result of A_{2g}, E_g and T_{2u} type distortions.[4] These correspond to the three lowest frequency vibrations in the gas-phase harmonic frequency calculation (but in the order A_{2g}, T_{2u} and E_g). In fact, at the B3LYP/6–31G* level of theory the A_{2g} vibration has an imaginary frequency (15i cm^{-1}) that prohibits its inclusion in the SHRINK treatment of vibrations. The frequency and eigenvectors will be very sensitive to the degree of anharmonicity so it is not surprising that the traditional approaches fail to model them adequately.

Figure 7.4: Eigenvectors of the 29 cm^{-1} vibrational mode of $Si_8O_{12}Me_8$ (calculated at the B3LYP/6–31G* level of theory).

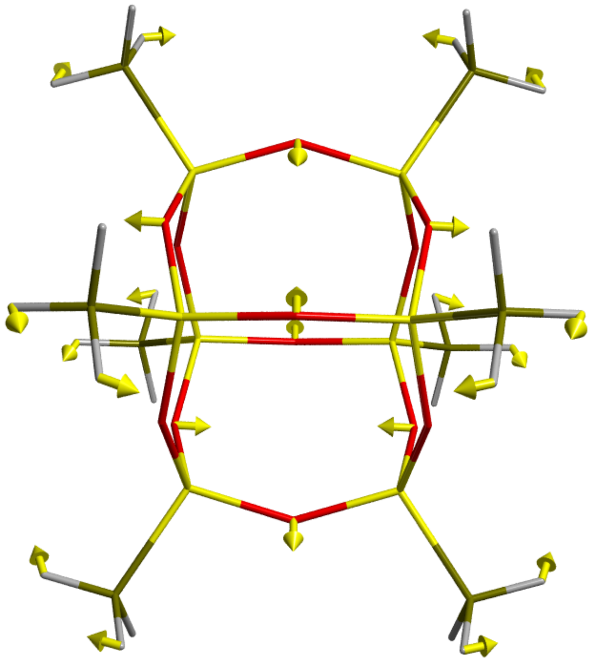

7.3.2 $Si_{10}O_{15}H_{10}$

The $Si_{10}O_{15}$ fragment has also been studied a number of times in the solid state.[7,34] The gas-phase structure of $Si_{10}O_{15}H_{10}$ was determined in a similar fashion to the structures of $Si_8O_{12}H_8$ and $Si_8O_{12}Me_8$. *Ab initio* and DFT calculations showed that the molecule had D_{5h} symmetry with two ten-membered Si_5O_5 rings joined with O atoms at each Si atom resulting in five eight-membered rings on the sides of the molecule. The pentagonal ten-membered rings are more flexible than the eight-membered rings in the Si_8O_{12} molecules and attempts to use traditional force-field methods failed. As in the case of the cube-like structures a number of the distance corrections are negative. Within the ten-membered rings there are two O$\cdots$O distances, a 1,2 distance (in terms of O atoms) and a 1,3 distance. The former is slightly shorter in the equilibrium structure by 0.006 Å but the latter is 0.134 Å longer in the equilibrium structure compared to the time-averaged one. The distances between ten-membered rings are typically shortened by thermal motion; the O$\cdots$O distance straight down from one ten-membered ring to the other is 0.143 Å shorter in the time-averaged structure. However, the distance between the O atoms that bridge the two larger rings are slightly longer in the time-averaged structures, suggesting expansion of the eight-membered rings in one direction, with compression in the other.

It is impossible to have repeating five-fold symmetry in 3-D space. It is therefore natural that the $Si_{10}O_{15}H_{10}$ molecule be distorted from the ideal D_{5h} symmetry seen in the gas phase. The distortions have also been the subject of PCA analysis by Bürgi and co workers.[34] Their results indicated that two pairs of degenerate distortions are responsible for the vast majority (97%) of the deviations from the ideal D_{5h} symmetry. The first pair involves the contraction of one of the ten-membered rings and expansion of the other ten-membered ring, while the second degenerate pair involves in-phase contraction/expansion of the two ten-membered rings. These correspond to the two lowest frequency vibrations in the gas-phase harmonic frequency calculation, which are depicted in Figure 7.5. Examining the plotted eigenvectors we can see the origin of the ten-membered ring distance corrections in the gas phase. The 1,3 O$\cdots$O distances have large vectors pointing towards each other, suggesting that this distance will shorten, while the 1,2 eigenvectors are nearly at 90° to each other, suggesting only a small correction. As in the case of the cube-like structures the lowest frequency modes all preserve the shape of the $HSiO_3$ tetrahedra.

Figure 7.5: The two lowest frequency vibrations of $Si_{10}O_{15}H_{10}$ (calculated at the HF/6–31G* level of theory).

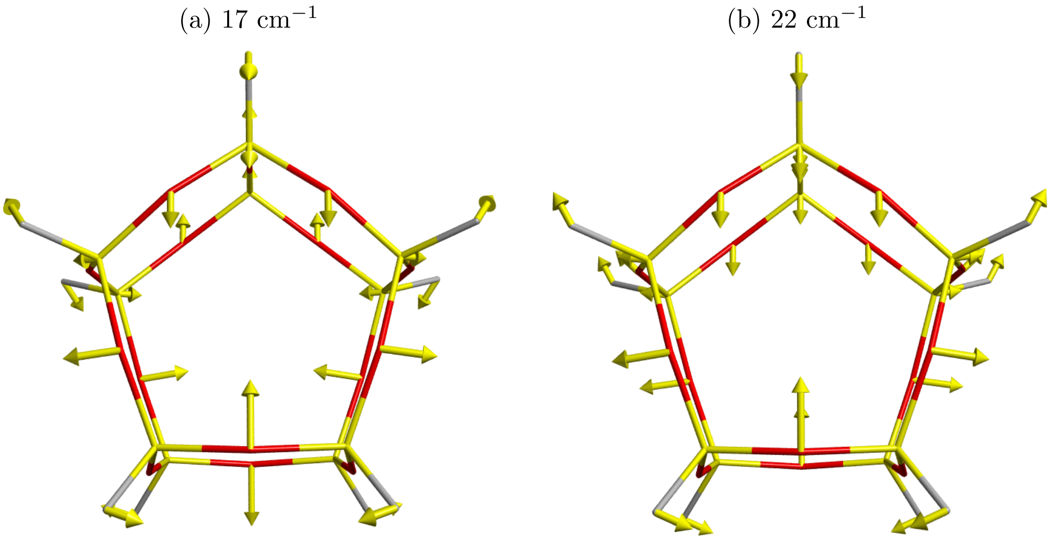
(a) 17 cm^{-1} (b) 22 cm^{-1}

7.3.3 $Si_6O_9(OSiMe_3)_6$

The $Si_6O_9(OSiMe_3)_6$ molecule has D_{3h} symmetry with a trigonal prism of silicon atoms at its core; it is the smallest of the silsesquioxanes (in terms of cage size) to be studied in the gas phase using the GED method. Unlike the previous molecules it features SiO_4 tetrahedra. While this cage does not feature in known zeolites, $Si_6O_9(OSiMe_2Br)_6$ has been used as a precursor to porous polymeric materials based on the Si_6O_9 core,[35] and the $Si_6O_{15}^{6-}$ ion is well known.[36,37]

The spatial extent of the molecule, with its bulky $OSiMe_3$ ligands, rendered plane-wave or Gaussian plane-wave DFT simulations impossible to perform due to the length of time and computational expense they would entail. Instead, semi-empirical (SE) methods (Section 2.2.8) were used to provide the forces for the MD simulation. The general-purpose CP2K code[38] was used to perform a series of simulations using a variety of SE methods including PM3,[39] PM6,[40] MNDO[41] and MNDO/D.[42] It was found that the best results (suitable for use in the GED refinement) were obtained using the MNDO/D and PM6 methods, both of which include *d* orbitals in the basis set used for the Si atoms. The inclusion of *d* orbitals is important for modelling the barriers to rotation of the various parts of the ligands.

The MD-derived distance corrections show that as for the $Si_{10}O_{15}H_{10}$ molecule, the vibrations make the Si_6O_9 cage contract in one direction and expand in another. The Si$\cdots$Si distance bridging the the trigonal faces of the prism shortens by 0.021 Å in the r_a structure, while the across-face Si$\cdots$Si distance is 0.013 Å longer.

7.4 Silsesquioxanes in the solid state

The distance corrections calculated from the MD simulations of the gas-phase silsesquioxane molecules suggest that the internal dynamics of the $Si_nO_{1.5n}$ cages affects the apparent "size" of the molecules. In the gas phase, the effect is small in magnitude and is only an issue for the refinement of the equilibrium structures but in the solid state, with the fixed reference of the lattice, the shrinkage or expansion of the cages could have an interesting affect on the thermal expansion of the materials. Contraction of the silsesquioxane molecules with increasing temperatures might lead to very low, or possibly even negative, coefficients of thermal expansion. The volumetric expansion coefficient is defined as:

$$\alpha_V = \frac{1}{V} \times \frac{\partial V}{\partial T} \simeq \frac{1}{V_0} \times \frac{\Delta V}{\Delta T}, \tag{7.7}$$

where V_0 is the initial volume. Some zeolites show volumetric expansion coefficients in the range of -15.1×10^{-6} K^{-1} to 32.1×10^{-6} K^{-1}.[43] The zeolite ITQ-7[44] has a volumetric expansion coefficient of -5.6×10^{-6} K^{-1} and features the Si_8O_{12} core in its structure. The phenomenon of negative thermal expansion has attracted considerable interest as composite materials made of negatively and positively expanding components could have zero expansion coefficients, making such materials suitable for use over a large temperature range, or have well defined expansion coefficients to match specific applications (*e.g.* tooth fillings).

$Si_8O_{12}R_8$ molecules have been studied extensively in the solid state using both experimental and computational techniques. Only a few of the experimental studies have determined structures at two or more temperatures. The symmetry in the solid state is always lower than the ideal, O_h, symmetry found in the gas phase. In the case of $Si_8O_{12}H_8$, $Si_8O_{12}Me_8$ and $Si_8O_{12}Cl_8$ the crystallographic symmetry is $\mathrm{\bar{R}3}$. This enforces $\bar{3}$ symmetry on the molecular sites but higher non-crystallographic symmetry of T_h occurs in the case of $Si_8O_{12}H_8$ and $Si_8O_{12}Me_8$.[4]

7.4.1 NVT DFT-MD simulation of $Si_8O_{12}Me_8$

A detailed study of the behaviour, in particular thermal expansion, of the molecular crystals of silsesquioxanes is beyond the scope of this present work. Such a study would require NPT DFT-MD simulations to calculate the time-averaged cell vectors at a series of temperatures. However, such calculations would be very difficult to converge without long simulation times or large supercells. However, it is feasible to use NVT DFT-MD simulations of unit cells to assess whether the dynamics in the solid state resemble those in the gas phase and if as a result similar distance/positional corrections occur in the solid state.

A Gaussian plane-wave[45] (GPW) DFT-MD simulation of a unit cell of $Si_8O_{12}Me_8$ was performed using the CP2K code in the NVT ensemble. The calculations made use of the facilities of HECToR, the UK's national high-performance computing service, which is provided by UoE HPCx Ltd. at the University of Edinburgh, Cray Inc. and NAG Ltd., and funded by the Office of Science and Technology through EPSRC's High End Computing Programme. The starting coordinates for the simulation were obtained from a geometry optimisation of the reported 291 K single-crystal X-ray structure.[5] The electronic wavefunction was represented in real space using double-ζ Gaussian basis functions with polarisation functions,[46] while plane-waves were used in reciprocal space to represent the electron density. A density cut-off energy of 5200 eV was used. Valence-core interactions were modelled using the GPW-optimised analytical pseudopotentials of Goedecker *et al.*[47,48] A simulation time step of 0.55 fs was used with data collected for a total of 12 ps. The trajectory was analysed in a similar fashion to the other DFT-MD trajectories discussed previously.

As the experimental structure was determined with a X-ray source, it is not possible to determine the equilibrium structure for $Si_8O_{12}Me_8$. However, it is still useful to compare the experimental and theoretical estimates of the amount of thermal motion. Table 7.2 shows the isotropic temperature factors for the six heavy atoms present in the asymmetric unit. A further four hydrogens make up the asymmetric unit but a combination of the methyl rotation and spherical form factors used in the experimental refinement renders meaningful comparison impossible for these atoms. The theoretical heavy-atom values are smaller in all cases than the experimental values by about 0.01–0.015 Å^2. This may arise from a lack of long-range phonon modes (as in the case of ammonia).

Table 7.2: $Si_8O_{12}Me_8$ experimental[5] and theoretical heavy-atom U_{eq} values (in Å^2).

	Expt.	Theory
Si(1)	0.0357(6)	0.0192(1)
Si(2)	0.0340(5)	0.0165(1)
O(1)	0.047(1)	0.0399(1)
O(2)	0.046(1)	0.0384(1)
C(1)	0.060(3)	0.0483(1)
C(2)	0.050(2)	0.0416(1)

The CP2K code does not have the ability to enforce the crystallographic symmetry (or the higher molecular symmetry). As a result, the geometry optimisation lead to small differences in the structures of the three molecules in the unit cell. Using only one of the optimised molecules the position corrections were of the magnitude of 0.017 Å to 0.032 Å for the heavy atoms. Similar results would be expected if an averaged or full symmetrised equilibrium geometry was used instead. Figure 7.6 shows (unit length) vectors pointing from the time-averaged coordinates to the equilibrium coordinates. For clarity, the hydrogen atoms are omitted and only a single molecule is shown in the cell. The vectors clearly show that the cage contracts. The intra-cage distance corrections are similar to those seen in the gas phase.

Figure 7.6: $Si_8O_{12}Me_8$ molecule with correction vectors (of unit length) pointing from the time-averaged position to the equilibrium position.

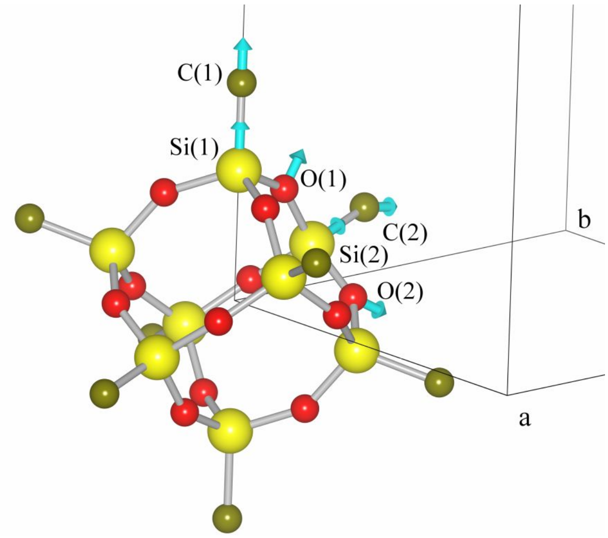

7.4.2 NPT EP-MD simulations

DFT simulations of the thermal expansion of the silsesquioxanes would be prohibitively expensive. However, a number of sets of empirical potentials have been tested for their suitability in modelling the Si_8O_{12} cage in the solid state by Ionescu *et al.*[49] The potentials tested included the condensed-phase optimised molecular potentials for atomistic simulation studies (COMPASS) force field developed by Sun[50] and a hybrid-COMPASS force field with and without electrostatic interactions. All of them were found to give acceptable results.

To assess the thermal expansion of $Si_8O_{12}H_8$ and $Si_8O_{12}Me_8$, simulations of both were performed at 300 and 400 K using the hybrid-COMPASS force field with no electrostatic interactions. The simulations were run in the anisotropic NPT ensemble using DL_POLY[51] version 2.20, running on the EaStCHEM Research Computing Facility (http://www.eastchem.ac.uk/rcf) Hare cluster. The simulation cell was a 2×2×2 supercell and a 7 Å cut-off radius was used for the intermolecular interactions. The simulations were run for a total of 360 ps using a time step of 0.6 fs. Using the average volumes at the two temperatures and the approximate form of Equation 7.7, α_V is estimated to be 152.8×10^{-6} K^{-1} for $Si_8O_{12}H_8$ and 192.2×10^{-6} K^{-1} for $Si_8O_{12}Me_8$, clearly indicating that the molecular crystals have positive thermal expansion. Although DFT would be expected to model the cage contracting modes more accurately, these values are likely to be representative for these materials. At 293 K, α_V for liquid water is 206×10^{-6} K^{-1}, while for ethanol it is 1400×10^{-6} K^{-1}.[52] Hard materials, such as metals, typically have much small coefficients; commercial titanium has a value of 25.5×10^{-6} K^{-1} at 298 K.[52]

The thermal expansion coefficients of $Si_8O_{12}H_8$ and $Si_8O_{12}Me_8$ are not that surprising for molecular crystals. While the cages contract, the vibrations of the molecules relative to each other will lead to overall expansion of the cage. If the silsesquioxanes were joined in one, two or three dimensions then it is possible that the contraction of the cage will dominate. The majority of crystalline systems featuring low or negative thermal expansion are framework or non-molecular materials. Investigating the thermal expansion of the silsesquioxanes cages in industrial applications may prove fruitful. Indeed, some epoxy resins with a $Si_8O_{12}R_8$ core are already known to have quite small thermal expansion coefficients in the range of 22×10^{-6} K^{-1}.[53] Interestingly, this behaviour is often explained in terms of the Si_8O_{12} cores being rigid.

7.5 Conclusion

An MD method for determining experimental equilibrium structures from GED data has been outlined and benchmarked using the structure of 1,3,5-chlorotriazine. This method uses classical or path-integral MD simulations to calculate amplitudes of vibration, distance corrections and Morse anharmonicity constants, all of which can be used in a GED refinement. Path-integral simulations are important for determining accurate amplitudes and distance corrections for interatomic distances involving light atoms or high-frequency vibrations.

This MD method has been used to determine the equilibrium structures of four silsesquioxane molecules. In the case of three of the four molecules the traditional force-field approach to estimating amplitudes of vibration and distance corrections proved inadequate. For $Si_8O_{12}R_8$ (R = H, Me) the theoretical distance corrections show that low-frequency vibrations result in an apparent shrinking of the Si_8O_{12} cage. The lower symmetry of the other two silsesquioxanes, $Si_{10}O_{15}H_{10}$ and $Si_6O_9(OSiMe_3)_6$, leads to shrinkage of some $(SiO)_n$ rings and expansion of others.

Solid-state MD simulations of $Si_8O_{12}H_8$ and $Si_8O_{12}Me_8$ using DFT and empirical potentials suggest that while the Si_8O_{12} cages still contract in the solid state there is overall expansion of the cell. More rigid systems, where the silsesquioxanes are joined, may exhibit much lower coefficients of thermal expansions than the molecular crystals of the monomer species.

Bibliography

[1] P. D. Lickiss and F. Rataboul, *Adv. Organomet. Chem.*, 2008, **57**, 1.

[2] K. Larsson, *Ark. Kemi.*, 1960, **16**, 215.

[3] T. P. E. Auf der Heyde, H. B. Bürgi, H. Bürgy and K. W. Törnroos, *Chimia*, 1991, **45**, 38.

[4] A. M. Bieniok and H. B. Bürgi, *J. Phys. Chem.*, 1994, **98**, 10735.

[5] V. G. Koellner and U. Müller, *Acta Cryst. C*, 1989, **45**, 1106.

[6] K. W. Törnroos, *Acta Cryst. C*, 1994, **50**, 1646.

[7] C. Marcolli, P. Lainé and G. Bühler, R. Calzaferri, *J. Phys. Chem. B*, 1997, **101**, 1171.

[8] C. Giacovazzo, H. L. Monaco, G. Artioli, D. Viterbo, G. Ferraris, G. Gilli, G. Zanotti and M. Catti, *Fundamentals of Crystallography*, Oxford University Press, 2nd edn., 2002.

[9] J. Tremmel and I. Hargittai, in *Stereochemical applications of gas-phase electron diffraction: Part A The electron diffraction technique*, ed. I. Hargittai and M. Hargittai, VCH Publishers, 1988, ch. Gas electron diffraction experiment, p. 191.

[10] (*a*) A. J. Blake, P. T. Brain, H. McNab, J. Miller, C. A. Morrison, S. Parsons, D. W. H. Rankin, H. E. Robertson and B. A. Smart, *J. Phys. Chem.*, 1996, **100**, 12280; (*b*) P. T. Brain, C. A. Morrison, S. Parsons and D. W. H. Rankin, *J. Chem. Soc., Dalton Trans.*, 1995, 4589; (*c*) N. W. Mitzel and D. W. H. Rankin, *Dalton Trans.*, 2003, 3650.

[11] I. Hargittai, in *Stereochemical applications of gas-phase electron diffraction: Part A The electron diffraction technique*, ed. I. Hargittai and M. Hargittai, VCH Publishers, 1988, ch. A survey: the gas-phase electron diffraction technique of molecular structure determination, p. 1.

[12] P. D. McCaffrey, J. K. Dewhurst, D. W. H. Rankin, R. J. Mawhorter and S. Sharma, *J. Chem. Phys.*, 2008, **128**, 204304.

[13] E. B. Wilson, J. C. Decius and P. C. Cross, *Molecular Vibrations*, McGraw-Hill Book Company, 1955.

[14] V. A. Sipachev, *J. Mol. Struct. (THEOCHEM)*, 1985, **121**, 143.

[15] V. A. Sipachev, *Struct. Chem.*, 2000, **11**, 167.

[16] P. D. McCaffrey, R. J. Mawhorter, A. R. Turner, P. T. Brain and D. W. H. Rankin, *J. Phys. Chem. A*, 2007, **111**, 6103.

[17] P. D. McCaffrey, *Ph.D. thesis*, University of Edinburgh, 2007.

[18] M. J. Frisch, G. W. Trucks, H. B. Schlegel, G. E. Scuseria, M. A. Robb, J. R. Cheeseman, J. A. Montgomery, Jr., T. Vreven, K. N. Kudin, J. C. Burant, J. M. Millam, S. S. Iyengar, J. Tomasi, V. Barone, B. Mennucci, M. Cossi, G. Scalmani, N. Rega, G. A. Petersson, H. Nakatsuji, M. Hada, M. Ehara, K. Toyota, R. Fukuda, J. Hasegawa, M. Ishida, T. Nakajima, Y. Honda, O. Kitao, H. Nakai, M. Klene, X. Li, J. E. Knox, H. P. Hratchian, J. B. Cross, V. Bakken, C. Adamo, J. Jaramillo, R. Gomperts, R. E. Stratmann, O. Yazyev, A. J. Austin, R. Cammi, C. Pomelli, J. W. Ochterski, P. Y. Ayala, K. Morokuma, G. A. Voth, P. Salvador, J. J. Dannenberg, V. G. Zakrzewski, S. Dapprich, A. D. Daniels, M. C. Strain, O. Farkas, D. K. Malick, A. D. Rabuck, K. Raghavachari, J. B. Foresman, J. V. Ortiz, Q. Cui, A. G. Baboul, S. Clifford, J. Cioslowski, B. B. Stefanov, G. Liu, A. Liashenko, P. Piskorz, I. Komaromi, R. L. Martin, D. J. Fox, T. Keith, M. A. Al-Laham, C. Y. Peng, A. Nanayakkara, M. Challacombe, P. M. W. Gill, B. Johnson, W. Chen, M. W. Wong, C. Gonzalez and J. A. Pople, *Gaussian 03, Revision E.01*, Gaussian, Inc., Wallingford, CT, 2004.

[19] C. Møller and M. S. Plesset, *Phys. Rev.*, 1934, **46**, 618.

[20] (*a*) A. D. Becke, *J. Chem. Phys.*, 1993, **98**, 5648; (*b*) C. Lee, W. Yang and R. G. Parr, *Phys. Rev. B*, 1992, **37**, 785; (*c*) B. Miehlich, A. Savin, H. Stoll and H. Preuss, *Chem. Phys. Lett.*, 1989, **157**, 200.

[21] *CPMD, Version 3.13.2, IBM Corp. 1990-2008, MPI für Festkörperforschung, Stuttgart, 1997-2001.*, 2008.

[22] G. Martyna and M. E. Tuckerman, *J. Chem. Phys.*, 1999, **110**, 2810.

[23] J. P. Perdew, K. Burke and M. Ernzerhof, *Phys. Rev. Lett.*, 1996, **77**, 3865.

[24] N. Troullier and J. L. Martins, *Phys. Rev. B*, 1991, **43**, 1993.

[25] M. E. Tuckerman, *Path Integration via Molecular Dynamics*, John von Neumann Institute for Computing, Jülich, 2002, vol. 10.

[26] M. P. Allen and D. J. Tildesley, *Computer Simulation of Liquids*, Oxford University Press, 1989.

[27] S. L. Hinchley, H. E. Robertson, K. B. Borisenko, A. R. Turner, B. F. Johnston, D. W. H. Rankin, M. Ahmadian and J. N. Jones, *Dalton Trans.*, 2004, 2469.

[28] K. Kuchitsu, M. Nakata and S. Yamamoto, in *Stereochemical applications of gas-phase electron diffraction*, ed. I. Hargittai and M. Hargittai, VCH Publishers, 1988, ch. Joint use of electron diffraction and high-resolution spectroscopic data for accuate determination of molecular structure, p. 227.

[29] D. A. Wann, A. V. Zakharov, A. M. Reilly, P. D. McCaffrey and D. W. H. Rankin, *J. Phys. Chem. A*, 2009, **113**, 9511.

[30] D. A. Wann, R. J. Less, F. Rataboul, P. D. McCaffrey, A. M. Reilly, H. E. Robertson, P. D. Lickiss and D. W. H. Rankin, *Organometallics*, 2008, **27**, 4183.

[31] D. A. Wann, F. Rataboul, A. M. Reilly, H. E. Robertson, P. D. Lickiss and D. W. H. Rankin, *Dalton Trans.*, 2009, 6843.

[32] D. A. Wann, A. M. Reilly, F. Rataboul, P. D. Lickiss and D. W. H. Rankin, manuscript accepted, *Z. Naturforsch., B*.

[33] F. S. Tautz, V. Heine, M. T. Dove and X. Chen, *Phys. Chem. Minerals*, 1991, **18**, 326.

[34] H. B. Bürgi, K. W. Törnroos, G. Calzaferri and H. Bürgy, *Inorg. Chem.*, 1993, **32**, 4919.

[35] P. G. Harrison and R. Kannengiesser, *Chem. Commun.*, 1996, 415.

[36] D. Hoebbel, G. Engelhardt, A. Samoson, K. Újszászy and Y. I. Smolin, *Anorg. Allg. Chem.*, 1987, **552**, 236.

[37] J. L. You, H. Chen, G. C. Jiang, H. Y. Hou, H. Chen, Y. Q. Wu and K. D. Xu, *Chinese Phys. Lett.*, 2004, **21**, 640.

[38] J. VandeVondele, M. Krack, F. Mohamed, M. Parrinello, T. Chassaing and J. Hutter, *Comp. Phys. Comm.*, 2005, **167**, 103.

[39] (*a*) J. J. P. Stewart, *J. Comput.Chem.*, 1989, **10**, 209; (*b*) J. J. P. Stewart, *J. Comput. Chem.*, 1989, **10**, 221.

[40] J. J. P. Stewart, *J. Mol. Model.*, 2007, **13**, 1173.

[41] M. J. S. Dewar and W. Thiel, *J. Am. Chem. Soc.*, 1977, **99**, 4899.

[42] W. Thiel and A. A. Voityuk, *J. Phys. Chem.*, 1996, **100**, 616.

[43] P. Lightfoot, D. A. Woodcock, M. J. Maple, L. A. Villaescusa and P. A. Wright, *J. Mater. Chem.*, 2001, **11**, 212.

[44] L. A. Villaescusa, P. A. Barrett and M. A. Camblor, *Angew. Chem. Int. Ed.*, 1999, **38**, 1997.

[45] G. Lippert, J. Hutter and M. Parrinello, *Mol. Phys.*, 1997, **92**, 477.

[46] I. N. Levine, *Quantum Chemistry*, Prentice Hall, 5th edn., 2000.

[47] (*a*) S. Goedecker, M. Teter and J. Hutter, *Phys. Rev. B*, 1996, **54**, 1703; (*b*) C. Hartwigsen, S. Goedecker and J. Hutter, *Phys. Rev. B*, 1998, **58**, 3641.

[48] M. Krack, *Theor. Chem. Acc.*, 2005, **114**, 145.

[49] T. C. Ionescu, F. Qi, C. McCabe, A. Striolo, J. Kieffer and P. T. Cummings, *J. Phys. Chem. B*, 2006, **110**, 2502.

[50] H. Sun, *Macromolecules*, 1995, **28**, 701.

[51] W. Smith and T. R. Forrester, *J. Mol. Graphics*, 1996, **14**, 136.

[52] *CRC Handbook of Chemistry and Physics*, ed. D. R. Lide, CRC Press, 89th edn., 2009.

[53] S. Sulaiman, C. M. Brick, C. M. De Sana, J. M. Katzenstein, R. M. Laine and R. A. Basheer, *Macromolecules*, 2006, **39**, 5167.

Chapter 8

Conclusions, recommendations and future work

8.1 Experimental equilibrium crystal structures

8.1.1 Molecular dynamics-derived equilibrium structures

Equilibrium structures are of particular use to structural chemists because they represent the system at rest without the potentially distorting effects of thermal averaging. To compare different experimental structures quantitatively with each other or with theory the use of equilibrium structures is essential. However, in the solid state there has been no generic way to correct structures for the effects of thermal motion up until now. Molecular dynamics (MD) simulations have been used to overcome this problem. MD simulations allow us to simulate the theoretical time-averaged structure of a crystal. This can be used together with a theoretical equilibrium structure to estimate corrections to experimental time-averaged structure. The resulting experimental equilibrium structure combines the best of theory and the best of experiment.

This MD method has been successfully applied to a series of molecules including ammonia, nitromethane and 1:1 urea-phosphoric acid (UPA). The results show large and significant corrections to atomic positions and interatomic distances. To study systems at low temperatures path-integral methods have been used to include the effects of zero-point energy and tunnelling. The results from nitromethane show that even systems with only zero-point energy can have statistically significant corrections to structural parameters.

The simulations carried out to date represent only an initial benchmarking and validation of this method. Further simulations are required to have a broader picture of what systems and chemical motifs are likely to be affected appreciably by thermal motion. In addition, all of the simulations performed in the course of this work have used either the relatively high-level DFT methodology or empirical potentials specifically optimised for the molecule of interest. A study of the suitability of more generic semi-empirical methods (such as PM6[1]) or optimised sets of empirical potentials (such as Amber[2] *etc.*) would be useful.

8.1.2 Equilibrium structures from experiment alone

Performing DFT-MD simulations is not feasible for all crystal structures and even with the use of empirical potentials or SE methods it is by no means a trivial procedure. It would be preferable if thermal motion could be accounted for using only experimental data. The experimental information on thermal motion takes the form of the 3-D probability density functions (PDFs) that describe the thermal motion of each atom in the mean field of the other $N-1$ atoms in the unit cell. The N 3-D PDFs are marginals of the full $(3N-3)$-D PDF that describes the complete thermal motion of the crystal lattice. These PDFs have corresponding free-energy surfaces associated with them. It was hoped that the minimum of the 3-D potentials would correspond to the minimum of the global potential, thus providing an estimate of the equilibrium structure. However, analysis of the results from a number of systems suggests that the minimum of an atom's 3-D potential can not be taken as a reliable estimate of its equilibrium position.

A possible way to overcome this problem would be to combine the individual 3-D PDFs to obtain the full $(3N-3)$-D PDF. However, this would require knowledge of the correlations between different atoms. In the harmonic limit the correlations between two atoms, k and k', can be described by:

$$U_{ij,kk'} = \langle \Delta u_{i,k} \Delta u_{j,k'} \rangle. \tag{8.1}$$

where u is a displacement from the mean atomic position and $i, j = 1, 2, 3$. For $k = k'$ we obtain the standard anisotropic displacement parameters. Information on the $k \neq k'$ terms is lost in a single experiment but is obtainable from a multi-temperature study.[3–5] Combining the PDFs and analysing the result would be challenging computationally but for some systems the majority of the effect could be captured by combining PDFs of atoms that will be strongly correlated. For example, in UPA the behaviour of the migratory proton will be strongly influenced by the two O atoms that it migrates between. The correlations between the three atoms could be extracted from the MD simulation that has already been performed and could be used to produce a 9-D PDF. If the minimum of this compares more favourably to the equilibrium position then this would confirm the origin of the differences in the probable and equilibrium positions.

Although multi-temperature studies could be used to determine the correlations, they may not always be feasible and for neutron studies they would be particularly expensive to perform. Another way to estimate the correlations would be to use a lattice dynamics calculation. Such a calculation would give only harmonic information but this should be sufficient for estimating correlation terms. Correlations might also exist in the higher-order terms but these should be small in comparison to the harmonic quantities.

8.2 Anharmonic probability density functions and Debye-Waller factors

The need to "correct" experiment structures for thermal motion effects arises because of anharmonicity in the potential-energy surface. In the diffraction experiment this anharmonicity manifests itself in deviations of the 3-D atomic PDFs from normal or Gaussian distributions. The vast majority of crystal structures only model thermal motion as Gaussian or harmonic in nature. While anharmonic PDFs may not provide a reliable estimate of equilibrium positions it is still important to model thermal motion properly. This can be seen by the considerable interest that anharmonic thermal motion has garnered in the crystallographic literature. The use of anharmonic PDFs should lower R factors and also provide structures that make more physical sense. In the case of nitromethane the C–D bond obtained by using anharmonic PDFs is far closer to the equilibrium value than the average distance.

The primary deficiency (and in a sense strength) of the previously developed anharmonic PDFs and Debye-Waller factors is their general form. A variety of different methods have been implemented that can fit nearly any degree of anharmonicity but at a significant cost in the number of parameters. The generic form was partly a result of the fact that little independent evidence or data could be collected about the nature of the anharmonicity and its effect on the shape of the PDF. In this present work MD simulations have been used to fill this gap. Numerical PDFs can be readily obtained from the MD simulations. As a test case, numerical PDFs showing a significant degree of curvature and/or asymmetry have been modelled using the traditional Gram-Charlier (GC) series approach as well as a parabolic and skew-normal PDF. The latter two PDFs, introduced to crystallographic use in the present work, model curvature and asymmetry, respectively. The results suggest that the numerical PDFs will prove useful in assessing the merit of different models of anharmonicity. In particular the parabolic PDF consistently produced better agreement with the numerical data but with far fewer parameters than the GC series.

The MD simulations used to collect the numerical PDFs need not be of the highest possible level of theory. Good agreement with experiment is of course preferable but all that is required is that the PDFs represent physically-reasonable distributions. A semi-empirical study of a large range of systems could be used to obtain a broad test set for new analytical PDFs.

8.2.1 Implementing new anharmonic Debye-Waller factors

For anharmonic treatment of thermal motion to become more widespread in crystallography it is important that new PDFs are intuitive, contain as few parameters as possible and are available in free and widely used software.

Functions that model anharmonic motion intuitively, such as the parabolic PDF, will be most easily defined in real space. In some cases it will not be possible to obtain analytical forms for the corresponding Debye-Waller factors. Even “true” PDFs, which must have an analytical Debye-Waller factor, may not have a succinct expression suitable for use in refinement programs. Refining structures using numerical Debye-Waller factors could overcome this problem and indeed the process of testing different functions on experimental data would be simplified if such a method could be easily implemented.

There is quite a variety of crystallographic software available for performing crystal structure refinement. Of these, the computational crystallography toolbox[6] (cctbx) (http://cctbx.sourceforge.net) is probably the most suited for implementing new Debye-Waller factors. The cctbx consists of a series of modules, written in C++ and python, that contain flexible code for handling crystallographic data and performing refinements. Its modular design allows new features to be implemented without the need for changes to every part of the code. Although developed for macromolecular crystal structures, where conventional programs perform poorly, the cctbx routines can be used for any type of system. The cctbx itself is command-prompt based but the graphic-user-interface based OLEX2 program[7] can use some cctbx features.

8.2.2 Visualisation of PDFs

Information on the harmonic approximation to thermal motion is easily visualised using surfaces of constant probability. For a 3-D Gaussian PDF such surfaces take the form of ellipsoids.[8,9] The depicted thermal ellipsoids can be used to assess how much different atoms move in the system and to assess the quality of the refinement.[10]

For anharmonic PDFs there has been practically no work on visualising analytical surfaces of constant probability. Older programs such as PROMETHEUS[11] were capable of plotting 2-D density and difference-density maps. The more recent XD2006[12] program renders GC-series PDFs numerically using volumetric datasets. Such an approach is probably the most efficient and effective one, especially with the wide variety of programs capable of rendering volumetric data.

One of the more widely used formats for volumetric data is the cube file format originally introduced by the Gaussian program as an output format for electron densities and molecular orbitals.[13] A number of chemical visualisers can use this format including VMD,[14] molekel[15] and Jmol.[16] Fortran90 programs have been written that take the output of an MD simulation and convert it into a cube file for visualisation of the numerical PDFs. Figure 8.1(a) shows the PDFs of d_3-nitromethane at 228 K rendered using Jmol and POV-ray.[17] A particular advantage of Jmol is its ability to take arbitrary "slices" through the volumetric data; Figure 8.1(b) shows the plane through the three D atoms. Jmol also supports a compact file format for isosurfaces and planes called jvxl, which could be used for interactive inspection of 3-D structures just as crystallographic information files (cifs) can be used to visualise thermal ellipsoids in programs such as Mercury.[18]

Figure 8.1: Jmol and POV-ray renderings of the numerical PDFs of d_3-nitromethane at 228 K. [Probability increases from red to blue in (b).]

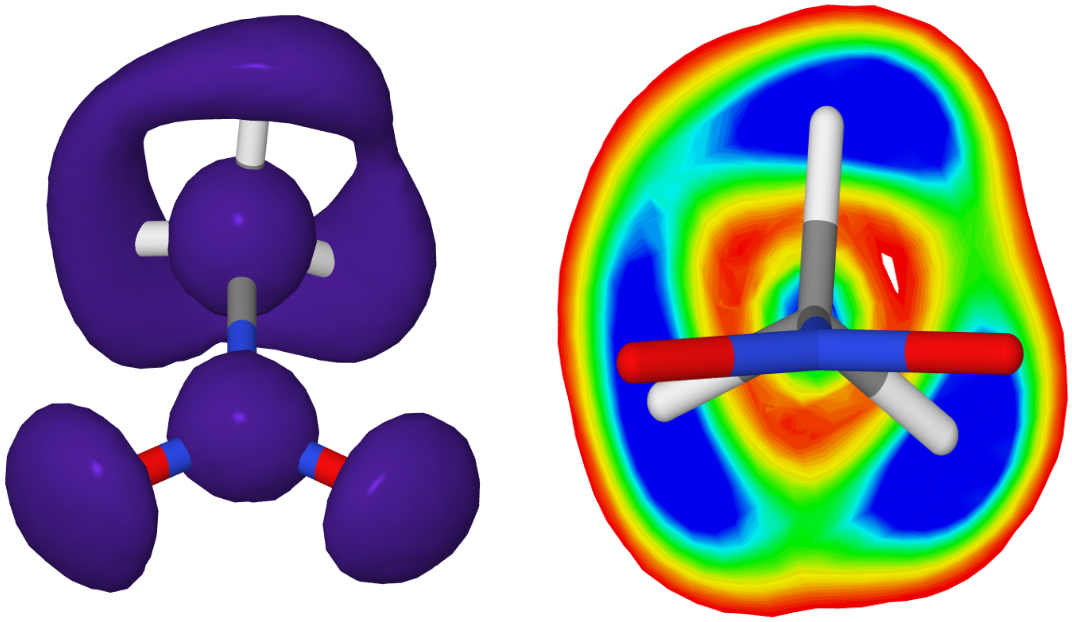

(a) 3D isosurface

(b) 2D plane through D atoms

8.3 Predicting anisotropic displacement parameters

The primary focus of this thesis has been extracting information on anharmonicity from MD simulations. It is also possible to extract harmonic information from the simulations. The theoretical prediction of ADPs would be of use for H atoms in X-ray studies or for studies at high pressure *etc.*, where experimental data are limited by the nature of the experimental apparatus. The results from the compounds studied in this work suggest that MD simulations could give reliable estimates of ADPs. Lattice dynamics (LD) calculations represent an alternative method and are more suitable for routine application. This is because they require far less computational effort and therefore permit higher levels of theory, such as hybrid DFT, to be used. LD calculations may have difficulties with highly anharmonic systems and MD simulations may prove useful for those systems in testing the LD approach.

8.4 Gas-phase equilibrium structures

The MD method can also be used in the gas phase, building on previous work by Dr. P. D. McCaffrey. The equilibrium structures of four silsesquioxane molecules have been determined using this method. Three of these molecules could not be studied with traditional gas electron diffraction (GED) approaches that use the gas-phase equivalent of lattice dynamics to estimate vibrational parameters. MD simulations are likely to be particularly suited to large molecules that feature low-frequency high-amplitude vibrations. Studying systems whose thermal motion is dominated by high-frequency vibrations may require the use of expensive path-integral MD simulations.

The application of MD simulations to GED structure determination is still in its infancy and further studies, particularly of compounds outside the silsesquioxane class of molecules, are required to fully assess the range of compounds it will be best suited to. It would be beneficial to implement the more generic scattering equation of McCaffrey *et al.*[19] into the ed@ed[20] refinement program. The standard Morse-potential based scattering equation is only effective at modelling anharmonicity between bonded atoms where the approximation of a Morse potential is valid. Using a more generic equation would allow all of the MD-derived data to be used in the refinement process.

Bibliography

[1] J. J. P. Stewart, *J. Mol. Model.*, 2007, **13**, 1173.

[2] W. D. Cornell, P. Cieplak, C. I. Bayly, I. R. Gould, K. M. J. Merz, D. M. Ferguson, D. C. Spellmeyer, T. Fox, J. W. Caldwell and P. A. Kollman, *J. Am. Chem. Soc.*, 1995, **117**, 5179.

[3] H. B. Bürgi and S. C. Capelli, *Acta Cryst. A*, 2000, **56**, 403.

[4] H. B. Bürgi, *Annu. Rev. Phys. Chem.*, 2000, **51**, 275.

[5] H. B. Bürgi, S. C. Capelli and H. Birkedal, *Acta Cryst. A*, 2000, **56**, 425.

[6] R. W. Grosse-Kunstleve, N. K. Sauter, N. W. Moriarty and P. D. Adams, *J. Appl. Cryst.*, 2002, **35**, 126.

[7] O. V. Dolomanov, L. J. Bourhis, R. J. Gildea, J. A. K. Howard and H. Puschmann, *J. Appl. Cryst.*, 2009, **42**, 339.

[8] *International Tables for Crystallography*, ed. A. J. C. Wilson, Kluwer Academic Publishers, 1995, vol. C, p. 505.

[9] C. K. Johnson, *ORTEP: a FORTRAN thermal-ellipsoid plot program for crystal structure illustrations*, ORNL report no. 3794. Oak Ridge National Laboratory, Oak Ridge, Tennessee.

[10] C. C. Wilson, *Cryst. Rev.*, 2009, **15**, 3.

[11] U. H. Zucker, E. Perenthaler, W. F. Kuhs, R. Bachmann and H. Schulz, *J. Appl. Cryst.*, 1983, **13**, 358.

[12] A. Volkov, P. Macchi, L. J. Farrugia, C. Gatti, P. Mallinson, T. Richter and T. Koritsanszky, *XD2006*, 2006.

[13] M. J. Frisch, G. W. Trucks, H. B. Schlegel, G. E. Scuseria, M. A. Robb, J. R. Cheeseman, J. A. Montgomery, Jr., T. Vreven, K. N. Kudin, J. C. Burant, J. M. Millam, S. S. Iyengar, J. Tomasi, V. Barone, B. Mennucci, M. Cossi, G. Scalmani, N. Rega, G. A. Petersson, H. Nakatsuji, M. Hada, M. Ehara, K. Toyota, R. Fukuda, J. Hasegawa, M. Ishida, T. Nakajima, Y. Honda, O. Kitao, H. Nakai, M. Klene, X. Li, J. E. Knox, H. P. Hratchian, J. B. Cross, V. Bakken, C. Adamo, J. Jaramillo, R. Gomperts, R. E. Stratmann, O. Yazyev, A. J. Austin, R. Cammi, C. Pomelli, J. W. Ochterski, P. Y. Ayala, K. Morokuma, G. A. Voth, P. Salvador, J. J. Dannenberg, V. G. Zakrzewski, S. Dapprich, A. D. Daniels, M. C. Strain, O. Farkas, D. K. Malick, A. D. Rabuck, K. Raghavachari, J. B. Foresman, J. V. Ortiz, Q. Cui, A. G. Baboul, S. Clifford, J. Cioslowski, B. B. Stefanov, G. Liu, A. Liashenko, P. Piskorz, I. Komaromi, R. L. Martin, D. J. Fox, T. Keith, M. A. Al-Laham, C. Y. Peng, A. Nanayakkara, M. Challacombe, P. M. W. Gill, B. Johnson, W. Chen, M. W. Wong, C. Gonzalez and J. A. Pople, *Gaussian 03, Revision E.01*, Gaussian, Inc., Wallingford, CT, 2004.

[14] W. Humphrey, A. Dalke and K. Schulten, *J. Mol. Graphics*, 1996, **14**, 33.

[15] *Molekel 5.3, Swiss National Supercomputing Centre, Manno, Switzerland.*

[16] *Jmol: an open-source Java viewer for chemical structures in 3D. http://www.jmol.org/.*

[17] *Persistence of Vision Raytracer (Version 3.6), Persistence of Vision Pty. Ltd., Williamstown, Victoria, Australia.*

[18] C. F. Macrae, I. J. Bruno, J. A. Chisholm, P. R. Edgington, P. McCabe, E. Pidcock, L. Rodrigeuz-Monge, R. Taylor, J. van de Streek and P. A. Wood, *J. Appl. Cryst.*, 2008, **41**, 466.

[19] P. D. McCaffrey, J. K. Dewhurst, D. W. H. Rankin, R. J. Mawhorter and S. Sharma, *J. Chem. Phys.*, 2008, **128**, 204304.

[20] S. L. Hinchley, H. E. Robertson, K. B. Borisenko, A. R. Turner, B. F. Johnston, D. W. H. Rankin, M. Ahmadian and J. N. Jones, *Dalton Trans.*, 2004, 2469.

Appendices

Appendix A

List of publications

1. Experimental equilibrium crystal structures: molecular dynamics as a probe for atomic probability density functions.
   A. M. Reilly, D. A. Wann, C. A. Morrison and D. W. H. Rankin, *Chem. Phys. Lett.*, 2007, **448**, 61.

2. The phonon spectrum of phase-I ammonia: reassignment of lattice mode symmetries from combined molecular and lattice dynamics calculations.
   A. M. Reilly, D. S. Middlemiss, D. A. Wann, M. M. Siddick, G. J. Ackland, C. C. Wilson, D. W. H. Rankin and C. A. Morrison, *J. Phys. Chem. A*, 2008, **112**, 1322.

3. Accurate Gas-Phase Experimental Structures of Octasilsesquioxanes ($Si_8O_{12}X_8$; X = H, Me).
   D. A. Wann, R. J. Less, F. Rataboul, P. D. McCaffrey, A. M. Reilly, H. E. Robertson, P. D. Lickiss and D. W. H. Rankin, *Organometallics*, 2008, **27**, 4183.

4. What makes the ^{31}P–^{31}P coupling constants in $S(PF_2)_2$ and $Se(PF_2)_2$ vary so much with temperature?
   A. M. Reilly, D. A. Wann and D. W. H. Rankin, *J. Phys. Chem. A*, 2009, **113**, 938.

5. The Application of Molecular Dynamics Simulations to Vibrational Corrections for Gas Electron Diffraction Equilibrium Structures.
   D. A. Wann, A. Zakharov, A. M. Reilly, P. D. McCaffrey and D. W. H. Rankin, *J. Phys. Chem. A*, 2009, **113**, 9511.

6. The gas-phase structure of the decasilsesquioxane $Si_{10}O_{15}H_{10}$.
   D. A. Wann, F. Rataboul, A. M. Reilly, H. E. Robertson, P. D. Lickiss and D. W. H. Rankin, *Dalton Trans.*, 2009, 6843.

7. The gas-phase structure of the hexasilsesquioxane $Si_6O_9(OSiMe_3)_6$.
   D. A. Wann, A. M. Reilly, F. Rataboul, P. D. Lickiss and D. W. H. Rankin, manuscript accepted, *Z. Naturforsch., B.*

8. Anharmonic thermal motion in d_3-nitromethane.
   A. M. Reilly, S. Habershon, R. Ibberson, D. E. Manolopoulos, C. A. Morrison and D. W. H. Rankin, manuscript in preparation.

9. MD-estimated anisotropic displacement parameters: DFT+D modelling of dynamics in benzophenone.
   A. M. Reilly, D. A. Wann, A. Daoud-Aladine, M. J. Gutmann, C. A. Morrison and D. W. H. Rankin, manuscript in preparation.

Publications 1-6 are included in the electronic appendix.

Appendix B

Conferences and courses attended

Conferences

- ScotCHEM Computational Chemistry Symposium
  University of St Andrews, April 2007
  Poster presentation “The equilibrium structure of crystalline ammonia”
- BCA Annual Spring Meeting
  University of Kent, Canterbury, April 2007
  Poster presentation “Towards equilibrium crystal structures”
- 12th European Symposium on Gas Electron Diffraction
  Blaubeuren, Germany, June 2007
  Poster presentation “The equilibrium structure of crystalline ammonia”
- 22nd Austin Symposium on Molecular Structure
  Austin, TX, USA, March 2008
  Poster presentation “A molecular dynamics approach to equilibrium structures in crystals: nitromethane”
- BCA Annual Spring Meeting
  University of York, April 2008
  Oral presentation “A molecular dynamics approach to equilibrium structures in crystals”
- ScotCHEM Computational Chemistry Symposium
  University of Glasgow, April 2008
  Poster and flash presentation “A molecular dynamics approach to equilibrium structures in crystals: nitromethane”
- 20th IUCr Congress
  Osaka, Japan, August 2008
  Poster presentation “A molecular dynamics approach to equilibrium structures in crystals: nitromethane”

- ISIS Crystallography User Group Meeting and PCG/SCMP Autumn Meeting
  Abingdon, Oxfordshire, November 2008
  Poster presentation “Understanding the effects of anharmonic thermal motion”
- ScotCHEM Computational Chemistry Symposium
  Heriot-Watt University, Edinburgh, April 2009
  Poster presentation “Applications of molecular dynamics simulations to crystallography”
- 13th European Symposium on Gas Electron Diffraction
  Blaubeuren, Germany, June 2009
  Poster presentation “Applications of molecular dynamics simulations to crystallography”

Courses and seminar series

- NSCCS CASTEP Workshop, 2006
- Intermediate Unix, 2006
- Unix shell programming, 2006
- ISIS neutron training course, 2006
- SUPA course in density functional theory (SUPADFT), 2006
- CCP5 summer school in molecular simulation, 2007
- Programming in Perl, 2007
- Creating web pages with HTML, 2008
- Formatting web pages with cascading style sheets, 2008
- Departmental colloquia, 2006-2009
- Inorganic, structural, materials and chemical physics section talks, 2006–2009

Appendix C

Contents of electronic appendix

The electronic appendix consists of a number of folders:

- **Benzophenone**: The intensity files (.hkl), SHELX input files (.ins) and resulting crystallographic information files (cifs) are provided here for the 70 K refinement and the four 300 K refinements. The cifs have not been fully validated.
- **Code**: This contains source code for the programs used to analyse some of the MD simulations performed as part of the work presented in this thesis. Some sample Mathematica notebooks for fitting anharmonic probability density functions to MD datasets are also provided. The vast majority of the empirical-potential MD code used for nitromethane and ammonia was written by other authors and is not included here.
- **Publications**: Copies of the first six publications listed in Appendix A are provided here as .pdf files. The remainder are in press or in preparation.
- **Thesis**: The cross-referenced electronic copy of this thesis is included in this folder.